LAPPEENRANTA UNIVERSITY OF TECHNOLOGY
School of Technology
LUT Mechanical Engineering
Mechanical Engineering

Ville Matilainen

CHARACTERIZATION OF PROCESS EFFICIENCY IMPROVEMENT IN LASER ADDITIVE MANUFACTURING

Examiners: Professor Antti Salminen
M. Sc. (Physics) Olli Nyrhilä

Supervisors: D. Sc. Heidi Piili
M. Sc. Tuomas Purtonen

ABSTRACT

Lappeenranta University of Technology
School of Technology
LUT Mechanical Engineering
Mechanical Engineering
Ville Matilainen

CHARACTERIZATION OF PROCESS EFFICIENCY IMPROVEMENT IN LASER ADDITIVE MANUFACTURING

Master's thesis

78 pages, 67 figures, 5 tables and 4 appendices

Examiners: Professor Antti Salminen
M. Sc. (Physics) Olli Nyrhilä

Keywords: Laser, additive manufacturing, 3D printing, stainless steel, process efficiency

Laser additive manufacturing (LAM), known also as 3D printing, has gained a lot of interest in past recent years within various industries, such as medical and aerospace industries. LAM enables fabrication of complex 3D geometries by melting metal powder layer by layer with laser beam.

Research in laser additive manufacturing has been focused in development of new materials and new applications in past 10 years. Since this technology is on cutting edge, efficiency of manufacturing process is in center role of research of this industry.

Aim of this thesis is to characterize methods for process efficiency improvements in laser additive manufacturing. The aim is also to clarify the effect of process parameters to the stability of the process and in microstructure of manufactured pieces. Experimental tests of this thesis were made with various process parameters and their effect on build pieces has been studied, when additive manufacturing was performed with a modified research machine representing EOSINT M-series and with EOS EOSINT M280. Material used was stainless steel 17-4 PH. Also, some of the methods for process efficiency improvements were tested.

Literature review of this thesis presents basics of laser additive manufacturing, methods for improve the process efficiency and laser beam – material- interaction. It was observed that there are only few public studies about process efficiency of laser additive manufacturing of stainless steel. According to literature, it is possible to improve process efficiency with higher power lasers and thicker layer thicknesses. The process efficiency improvement is possible if the effect of process parameter changes in manufactured pieces is known.

According to experiments carried out in this thesis, it was concluded that process parameters have major role in single track formation in laser additive manufacturing. Rough estimation equations were created to describe the effect of input parameters to output parameters. The experimental results showed that the *WDA* (width-depth-area of cross-sections of single track) is correlating exponentially with energy density input. The energy density input is combination of the input parameters of laser power, laser beam spot diameter and scan speed.

The use of skin-core technique enables improvement of process efficiency as the core of the part is manufactured with higher laser power and thicker layer thickness and the skin with lower laser power and thinner layer thickness in order to maintain high resolution. In this technique the interface between skin and core must have overlapping in order to achieve full dense parts.

It was also noticed in this thesis that keyhole can be formed in LAM process. It was noticed that the threshold intensity value of 10^6 W/cm^2 was exceeded during the tests. This means that in these tests the keyhole formation was possible.

TIIVISTELMÄ

Lappeenrannan teknillinen yliopisto
Teknillinen tiedekunta
LUT Kone
Konetekniikka

Ville Matilainen

LISÄÄVÄN VALMISTUKSEN PROSESSITEHOKKUUDEN PARANTAMISEN KARAKTERISOINTI

Diplomityö

78 sivua, 67 kuvaa, 5 taulukkoa ja 4 liitettä

Tarkastajat: Professori Antti Salminen
Filosofian maisteri Olli Nyrhilä

Hakusanat: laser, lisäävä valmistus, 3D-tulostus, ruostumaton teräs, prosessitehokkuus

Laseravusteinen lisäävä valmistustekniikka, joka tunnetaan yleisemmin myös 3D-tulostuksena, on yleistynyt viimeisien vuosien aikana huomattavasti muun muassa ilmailu- ja lääketeollisuudessa. Laseravusteisella lisäävällä valmistustekniikalla voidaan valmistaa monimutkaisia kolmiulotteisia kappaleita sulattamalla metallijauhetta kerros kerrokselta lasersäteen avulla. Lisäävän valmistuksen tutkimuksessa on viime vuosina keskitytty voimakkaasti uusien materiaalien kehittämiseen sekä uusien käyttökohteiden selvittämiseen. Koska tämä teknologia on nyt tekemässä läpimurtoa, on valmistusprosessia yritetty kehittää myös nopeammaksi ja tehokkaammaksi.

Tämän työn tarkoituksena oli selvittää, miten laseravusteista lisäävää valmistusta voitaisiin tehostaa. Tavoitteena oli myös selvittää, millainen vaikutus prosessiparametrien muutoksilla on valmistusprosessin vakauteen ja valmistetun kappaleen mikrorakenteeseen. Kokeissa varioitiin valmistusparametreja ja niiden vaikutusta syntyneisiin kappaleisiin tutkittiin. Koelaitteistoina käytettiin EOS EOSINT M-sarjan prototyyppi laitetta, sekä EOS EOSINT M280 laitetta. Materiaalina käytettiin 17-4 PH jauhetta, joka on ruostumaton teräsjauhe.

Kirjallinen osa esittelee laseravusteisen lisäävän valmistuksen perusteita, käsittelee keinoja tehostaa valmistusprosessia sekä paneutuu lasersäteen ja metallimateriaalin

vuorovaikutukseen. Kirjallisuudessa prosessitehokkuutta käsittelevää aineistoa oli niukasti julkaistuna, mutta löydetyissä artikkeleissa prosessitehokkuutta oli yritetty parantaa suurempitehoisilla lasereilla ja paksummalla kerrospaksuudella. Prosessitehokkuuden kasvattaminen edellyttää perustietoja prosessiparametrien vaikutuksesta valmistettavaan kappaleeseen.

Kokeellisessa osassa koekappaleita valmistettiin eri prosessiparametreilla ja tutkittiin niiden vaikutusta syntyneiden kappaleiden mikrorakenteisiin. Kokeellisessa osassa selvitettiin käytännön kokeiden avulla kirjallisuudessa esitettyjen prosessitehokkuuden parantamisen keinojen luotettavuutta.

Koetulosten perusteella todettiin, että prosessiparametrien muutoksilla on suuri merkitys yksittäisen palon muodostumiseen. Tulosten perusteella määriteltiin yhtälöitä, joiden avulla voidaan karkeasti arvioida sisäänmenoparametrien vaikutusta ulostuloparametreihin. Tulokset osoittivat, että *WDA* (tunkeuman poikkipinnan pinta-ala) korreloi eksponentiaalisesti prosessiin tuodun energiatiheyden kanssa. Energiatiheys on laskennallinen arvo, joka muodostuu prosessin sisäänmenoparametreista kuten laserteho, kerrospaksuus, skannausnopeus ja skannaustiheys.

Kokeet osoittivat, että skin-core tekniikkaa voidaan käyttää prosessin nopeuden kasvattamiseksi. Tällä tekniikalla kappaleen sisäosa valmistetaan suuremmalla laserteholla, sekä paksummalla kerrospaksuudella, kun taas kappaleen pinta ohuemmalla kerrospaksuudella ja pienemmällä laserteholla. Tällä tekniikalla valmistettaessa tulee varmistaa sisäosan ja ulkopinnan välisen rajapinnan yhteenliittyminen, jotta huokosia ei synny kappaleeseen.

Tulokset osoittivat, että LAM prosessin aikana on mahdollista muodostua samanlainen avaimenreikä kuin laserhitsauksessa. Lasersäteen intensiteetin raja-arvo avaimenreiän syntymistä varten on 10^6 W/cm^2, joka ylitettiin kokeiden aikana.

ACKNOWLEDGEMENTS

This thesis was carried out as a part of the Finnish Metals and Engineering Competence Cluster (FIMECC)'s program MANU - Future digital manufacturing technologies and systems.

I would like to thank examiners of my thesis, Professor Antti Salminen and Mr. Olli Nyrhilä, for giving valuable suggestions, ideas and guidance for this thesis. I want to express my gratefulness to the supervisor D.Sc. Heidi Piili, whose comments and guidance during the thesis had big influence in pushing this thesis forward and adjusting it into right direction.

I want to thank Mr. Tatu Syvänen and Mr. Hannu Heikkinen from EOS Finland for helping me to execute the experiments in Turku. I want to thank also the staff of EOS Finland for their warm hospitality during my visit there.

I thank the staff of LUT Laser for all the help and constructive discussions during the thesis. Special thanks goes to Mr. Antti Heikkinen who helped preparing the specimen to metallurgical analyses.

Huge thanks goes to my family and friends. I thank my parents who have supported me during my studies. Last but definitely not least I thank Kaisa for all the support.

Thank You All!

Ville Matilainen

Lappeenranta 16th of April 2014

TABLE OF CONTENTS

LIST OF SYMBOLS AND ABBREVIATIONS

A	absorption coefficient
A_{Laser}	area of laser beam spot
d	diameter of the laser beam spot
E	thermalized energy amount on single powder grain
I	intensity distribution
I_0	maximum intensity
$I(r,z)$	rotationally symmetric Gaussian intensity distribution
J	joule
P	laser power
r	radius of laser beam
t	laser interaction time
v	laser scanning velocity
$V_{process}$	process velocity
W	watt
w	full laser beam radius
z	distance along propagation direction
φ	plane angle
λ	wavelength
μm	micrometer
$3D$	3 dimensional
$AISI$	American Iron and Steel Institute
BW	bead width
$DMLS$	direct metal laser sintering
ED	energy density
kW	kilowatt
LAM	Laser Additive Manufacturing
LT	layer thickness
mm	millimeter
mm^3	cubic millimeter
mm/s	millimeters/second

ms	millisecond
PBF	powder bed fusion
PD	penetration depth
R&D	research and development
SLI	slice layer interface
SLM	selective laser melting
SLS	selective laser sintering
STL	CAD file format, which is widely used in additive manufacturing
WDA	width*depth area
WDR	width-depth ratio

1 INTRODUCTION

Laser additive manufacturing was developed in 1990's but not until past few years it has been considered as part of industrial revolution. Since the technology has developed with fast speed, the manufactured parts can be used in various demanding industries such as medical, automotive and aerospace industries. Nowadays, the 3D printing hype has brought additive manufacturing closer to consumer products and it is noticed that the manufacturing process efficiency could be improved. The need of customized large scale production also pushes this technology into developing the manufacturing process.

Laser additive manufacturing is a powder based process that allows designer to create parts that are hard or impossible to manufacture with conventional methods. Also the possibility to optimize part weight and strength is an advantage of this technology. Parts are built layer by layer as the laser beam melts the next layer on top of the previous one.

In this thesis, methods for process efficiency improvements are studied. Also the laser-material interaction is studied. It is important to understand the effects of the process parameters in the manufacturing process in order to achieve building process without interruptions and high quality parts.

LITERATURE REVIEW

2 PRINCIPLE OF LASER ADDITIVE MANUFACTURING

Laser additive manufacturing (LAM) process is layer-wise material addition technique where complex 3D parts are manufactured by selective melting and solidification of consecutive layers of powder material on top of each other. This process is also known in different names and abbreviations for example *DMLS* (EOS GmbH), SLM (SLM Solutions, Realizer) and Laser Cusing (Concept Laser). All of these techniques are powder bed fusion processes (PBF) which is official and standardized abbreviation of this manufacturing method. In all of previously mentioned cases the part building process is basically the same. Powder material melting is done with focused and computer guided laser beam. (Kruth et al., 2010, p. 1, ASTM Standard, 2012, F2792 - 12a, p. 1)

The advantages of laser additive manufacturing are geometrical freedom, mass customization and shortened design to production time. The laser additive manufacturing can be used for e.g. building visual prototypes, customized medical parts, tooling molds, tooling inserts and also consumer products such as jewelry. (Kruth et al., 2005, p.1, Wohlers and Caffrey, 2012 p.12-13)

This technology has also challenges what comes to the manufacturing process. First of all, the designer should know the limitations and capabilities of this manufacturing process. For example, it is difficult or even impossible to create flat overhanging features without support structures. It is also preferable to create designs and geometries which do not need support structures or they are minimized. (Gibson et al. 2010 p. 705) Avoiding and minimizing the support structures also decrease the amount of post processing needed. One disadvantage is also the relatively slow speed of the manufacturing process due to very small layer thickness. (Ilyas et al., 2010, p. 430)

Increasing the manufacturing speed of this process has been done with mounting more powerful, even kW- range, lasers to the LAM machines. It is possible to melt thicker layers of metal powder with higher laser power and with this way achieve higher building speeds. However, when increasing the layer thickness, the z-direction resolution decreases. It is recommended to use for higher power a skin-core technique, where the skin or the contours of the part are scanned with lower power lasers with thinner layer thickness. The core of the part is then scanned with high power laser with thicker layer thicknesses i.e. multiple thin layers. (Kelbassa et al., 2012, p.2-3)

2.1 Basics of CAD processing

In additive manufacturing, the desired parts are built into physical objects from 3D model. The 3D model is converted into .STL-file format. This .STL-file describes the external closed surfaces of the original 3D model and forms the basis for calculation of the slicing. When the 3D object is on .STL-format, it can still be modified lightly such as scaled or oriented optimally. The part also need support structures, which attach the part onto the build platform, conduct heat away and serve as support if the building angle is too low. The support structures also protect the part itself when detached from the building platform. After all modification and support generation, the supports and the part itself are sliced into the slice format used in LAM machine. The layer thickness is equal to the slice thickness of the slice file which is typically with current machines 20-50 µm with metallic materials. (Gibson, et al. 2010, p. 1-6) Figure 1 shows file manipulation from 3D model to slice file and finally finished part.

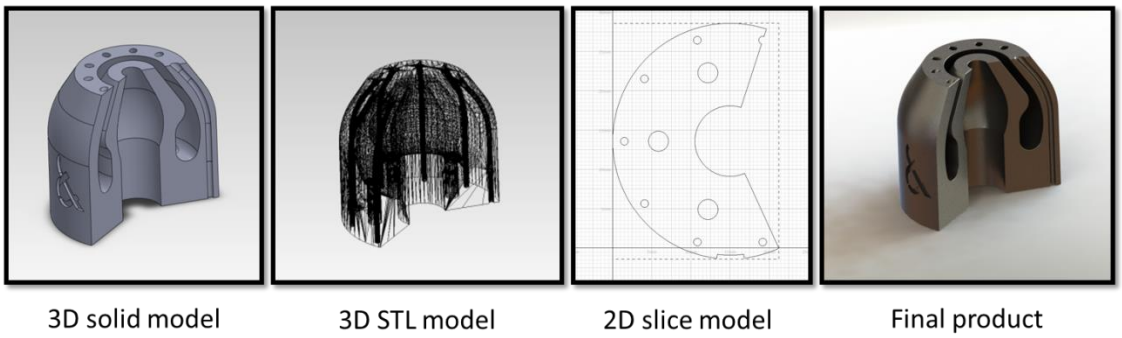

Figure 1. File manipulation from 3D model to final product (LUT Laser 2013).

2.2 Basics of powder bed fusion process

Objects are built layer by layer from powder material in PBF process as it can be seen from figure 2.

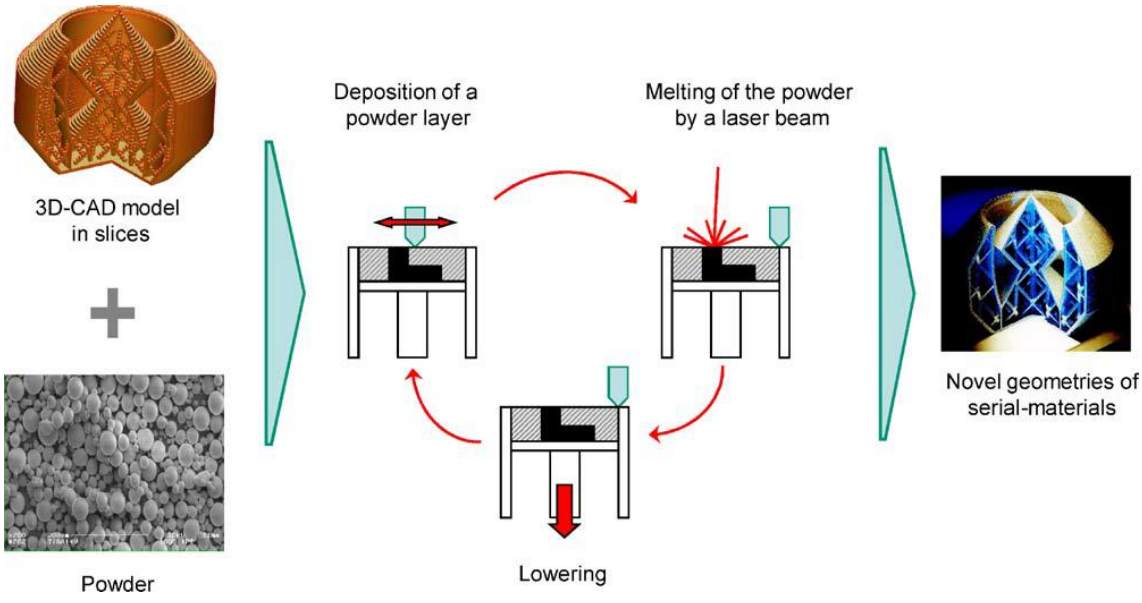

Figure 2. Principles of the laser sintering process (Schleifenbaumet al., 2010, p.162).

Cross-section of desired geometry is melted locally by laser beam to form a solid layer. Once the cross-section is melted a new layer of powder material is spread. This cycle is continued until the desired object is finished. Powders can be preheated close to melting temperature and beam is only used to add small differential energy to melt powder layers together. Preheating powder reduces required laser energy and at the same time decreases temperature difference between layers. Internal stress and deformation can be reduced by low temperature difference. The building process is usually taken place in inert atmosphere to avoid oxidation. Typically building chamber is filled with nitrogen or argon. (Gibson et al. 2010, p. 112-113)

Once the building process is finished the part is surrounded by infusible loose powder. This loose powder is removed and it can be reused after sieving. Finished parts are detached from the building platform and post processed if needed. Post processing can include annealing, machining or different surface treatments such as sandblasting and polishing. (Löber et al., 2013, p.173-174)

3 PROCESS EFFICIENCY

Research on additive manufacturing has been focused into new material qualification and implicating them into different industrial applications. This means that there are only few studies about process efficiency and build rate of LAM process and most of these are rather old or made by machine manufacturers R&D departments for their own purposes.

For example Meiners (1999) and Wagner (2003) have studied build rates in their doctoral theses. The process cycle time can be divided into primary and auxiliary process time in order to understand LAM process efficiency better. The primary process time consists the time that is needed in melting each layer of desired geometry. The auxiliary process time consists of operations, such as building plate lowering and powder spreading. (Schleifenbaum et al. 2010, p. 162, Kelbassa et al. 2012 p.2)

Studies found from literature are focused to investigate the primary process time and increase of build rate through that. This is because of processing time of large volume parts consists more than 80% of the primary process time. Also several low volume parts can be counted into one large volume part which is placed on single building platform and manufactured simultaneously. (Schleifenbaum et al. 2010, p. 162)

Variables that influence the process time are layer thickness (LT), laser scanning velocity (v) and hatch distance (h). The build rate is calculated according equation 1.

$$V_{process} = LT \cdot v \cdot h \quad (1)$$

where $V_{process}$ process velocity
LT layer thickness
v laser scanning velocity
h hatch distance

The scanning velocity and layer thickness are limited by the available laser power. The hatch distance is limited by the diameter of focused laser beam. (Buchbinder et al., 2011, p.272-273)

3.1 Laser power

In order to make breakthrough into series production, the LAM process build rate should be increased significantly. One way to increase build rate is to couple LAM machines with higher power lasers in order to be able to increase layer thickness. It is also possible to increase the scanning velocity with increased laser power which leads to speeding up the building process. However, there is only limited potential to increase the build rate with only increasing laser power and scanning velocity, while keeping the beam diameter constant. When maintaining the beam diameter constant and increasing the laser power, the intensity increases also at the point of processing. This leads to higher evaporation rate and results in higher amount of spattering which has negative effect on the process. In order to avoid higher evaporation and excessive spattering, the beam diameter should

be enlarged with increase in laser power. While enlarging beam diameter, the accuracy and detail resolution of the process is decreasing. It is considered to use skin-core strategy in part building to avoid resolution and accuracy decrease. This skin-core scanning strategy means that the build part must be divided into inner core and outer skin which forms the contours of the part. The skin-core scanning strategy is shown in figure 3. (Schleifenbaum et al. 2010, p. 162-163, Kelbassa et al. 2012, p.2, Buchbinder et al. 2011, p.272)

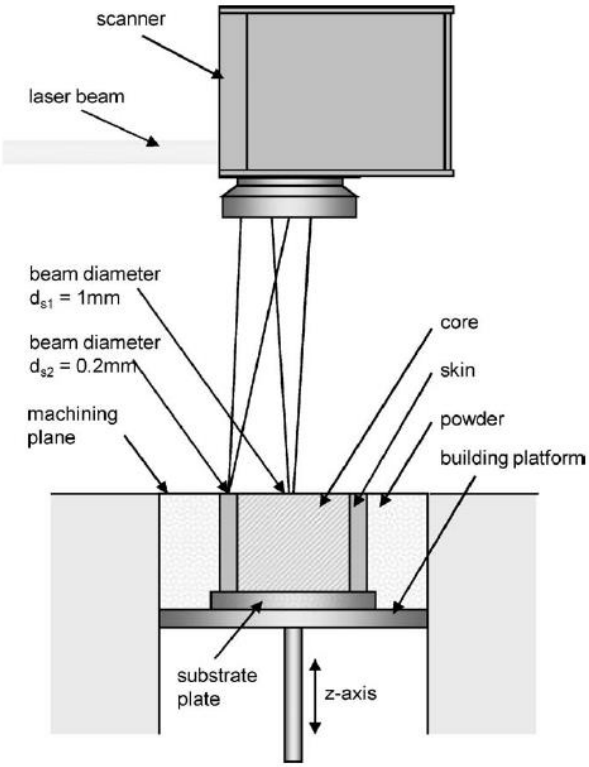

Figure 3. Skin-core scanning strategy (Schleifenbaum et al., 2009, p. 388).

Even though parameters differ in skin and core of the component, they both must have density approximately 100% to make sure that the mechanical properties are same as with conventionally manufactured components. Also the interface of skin and core should be 100% dense in order to achieve proper mechanical properties. (Schleifenbaum et al. 2010, p.163)

3.2 Power density distribution

As mentioned earlier, there is limited possibility to increase the build rate by means of single mode high power lasers. These single mode lasers have Gaussian beam profile,

which means that intensity is extremely high in the centre of the beam. Figure 4 presents the schematic illustration of Gaussian beam profile. (Schleifenbaum, et al., 2011, p. 362)

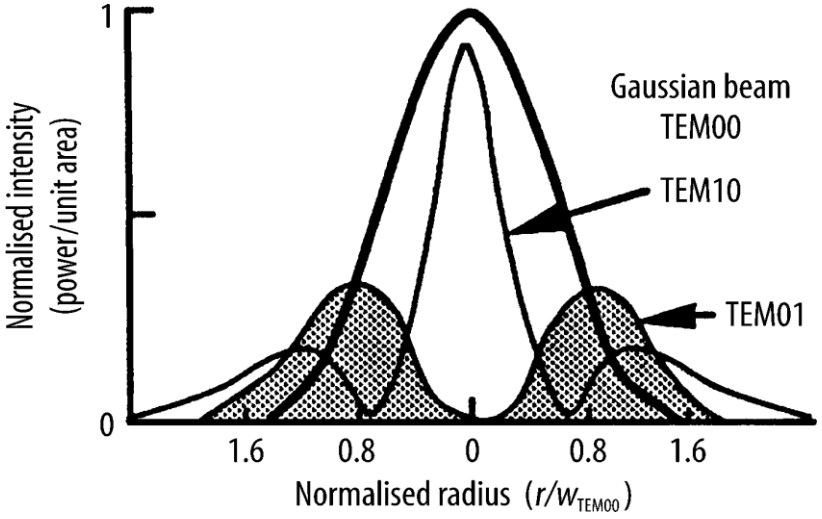

Figure 4. Gaussian beam profile (Steen, Mazumder, 2010, p. 100).

This leads into increased evaporation of the material and also causes spattering which disturbs the process stability. The scan line spacing should be more frequent since the beam diameter is smaller with use of Gaussian beam profile. This is why Schleifenbaum et al. (2010) and Kelbassa et al. (2012) are decided to use multi-mode laser beam with top hat shaped beam. The top hat shaped beam diameter is usually larger than with Gaussian beam profile and the intensity of the beam is more equal throughout the whole beam diameter. Top hat beam profile is shown in figure 5. (Kelbassa et al. 2012, p.3, Schleifenbaum et al. 2010 p. 360-361)

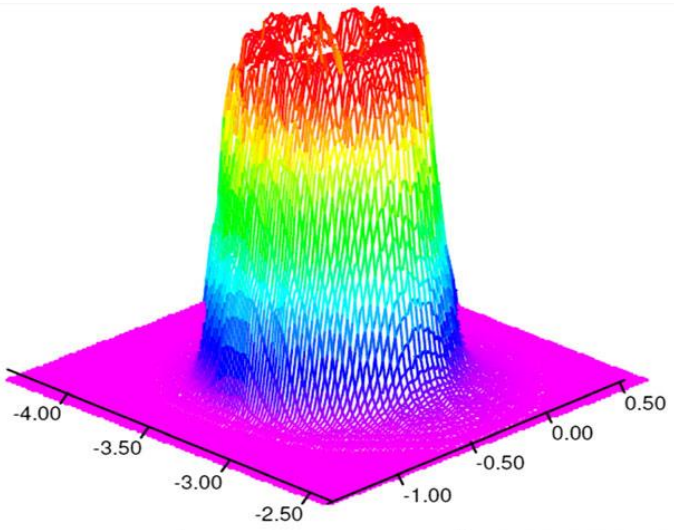

Figure 5. Intensity distribution of top hat shaped laser beam (Schleifenbaum et al. 2011, p. 367).

As mentioned before, the Gaussian beam profile can limit the maximum possible scan line spacing since each powder grain needs a certain amount of thermal energy to completely melt. The amount of thermalized energy in single powder grain is determined by equation 2. (Schleifenbaum et al. 2011, p. 362)

$$E = A \cdot \iiint I(r, \varphi) \cdot r dr d\varphi dt, \quad (2)$$

where
- E thermalized energy amount on single powder grain,
- A absorption coefficient,
- I intensity distribution,
- r radius of laser beam,
- φ plane angle.

When considering rotationally symmetric Gaussian intensity distribution in any distance z along the propagation direction, the intensity distribution can be written as equation 3 illustrates. (Schleifenbaum et al. 2011, p. 363)

$$I(r, z) = I_0(z) \cdot e^{\frac{2r^2}{w(z)^2}} \quad (3)$$

where
- $I(r,z)$ rotationally symmetric Gaussian intensity distribution
- r radius of laser beam,
- z distance along propagation direction,
- I_0 maximum intensity,
- w full beam radius.

Equation 3 shows that if powder grains are too far from center of the laser beam and far from maximum intensity I_0, the grains are exposed to lower amount of energy than the ones which are located in the beam center. If the lower amount of energy is less than the thermal energy needed to melt the powder grain, the grain is not completely molten. This can lead into imperfections between scan lines and instability of building process. (Schleifenbaum et al. 2011, p. 363)

For comparison, intensity distribution of ideally uniform laser beam is described in equation 4.

$$I(r, z) \approx I_0(z) \quad (4)$$

As it can be seen from equation 4, the intensity distribution in ideally uniform laser beam is no longer dependent on beam radius r. This means that this kind of beam profile can melt the powder grains almost over the complete beam diameter. Because of this, the scan line spacing can be enlarged in comparison of Gaussian beam profile and this way speed up the process and increase the build rate as shown in equation 1. It is also possible to use

higher laser power because there is no similar intensity peak in the middle of the beam as with Gaussian beam profile. Due to this the top hat profile can be used and it seems suitable when laser power is increased. Also the usage of multi-mode lasers can be considered because the top hat profile is boosted by the superposition of many transversal electromagnetic modes during the propagation through an optical multimode fiber. (Schleifenbaum et al. 2011, p. 363, Schleifenbaum et al. 2010, p. 164)

LAM machines should be equipped with two laser sources when using high power multimode lasers to be able to maintain high resolution on manufactured parts. As described earlier, the high power multimode lasers focused spot size is relatively large and it is suitable for melting large areas of the part cross-sections. The skin resolution of the part suffers, if the laser beam spot size is large and this is why the other, lower power laser with smaller spot size should be applied. If the used laser is single-mode laser, it can be used alone to expose the core and the skin of the part because the beam can be focused into smaller spot size and that way maintain high detail resolution in part manufacturing. (Shcleifenbaum et al. 2010, p. 163-166)

When applying two lasers into LAM system, the optical system should be redesigned in order to be able to switch laser sources from different fibers to the scanner. Schleifenbaum et al. from Fraunhofer ILT have designed and patented a system where laser source switching is possible. In this system movable tilted mirror is moved into the course of the laser beam with linear axis. The optical system is shown in figure 6. (Schleifenbaum et al. 2011, p. 364)

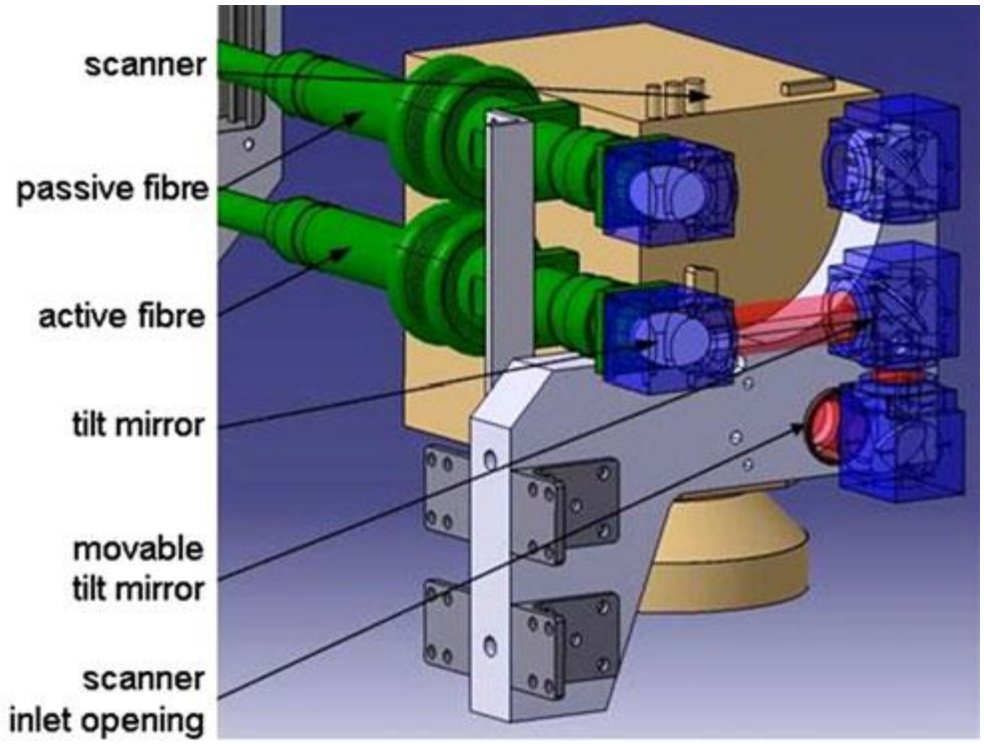

Figure 6. 3D- model of optical system for high power LAM machine (Schleifenbaum et al. 2011, p. 364).

With the assist of movable tilted mirror, the laser beam is guided into the scanner system and focused to the building plane with f-theta-lens. This system is able to focus the laser beam into spot sizes between 193 µm and 1050 µm with 50 µm and 200 µm fibers respectively. It is also possible to vary the focus diameter between 100 µm and several millimeters by varying the collimating focal length, fiber core diameters and by changing the focal length of the f-theta-lens. (Schleifenbaum et al. 2011, p. 364)

3.3 Single track formation in LAM process

The part properties of LAM manufactured parts depend highly on the properties of each single laser melted track and each layer formed by these tracks. When the tracks or lines are melted with laser beam, molten pool is formed. Cross-section of laser melted track is presented in figure 7. (Yadroitsev, et al., 2013, p. 606)

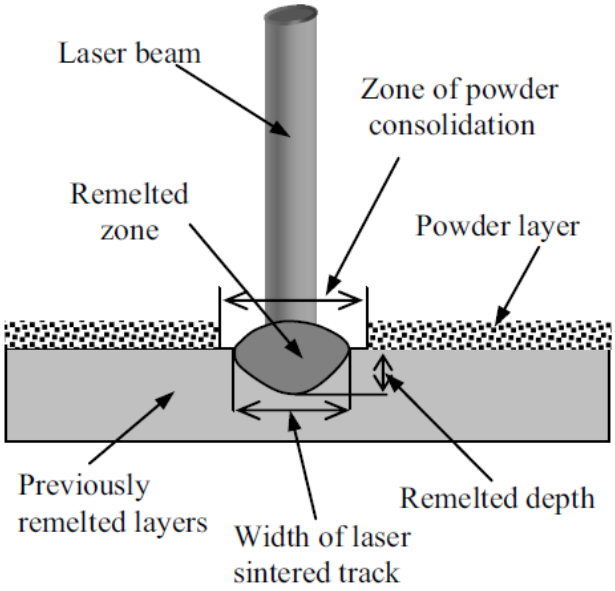

Figure 7. Cross-section of laser melted track from metal powder on substrate (Yadroitsev, Smurov, 2010a, p. 553).

Effect of surface tension gives the molten pool to a form of circular or segmental cylinder. It is vital to be able to control the process such that the melted tracks do not fragment. The fragmentation is well known drawback of the PBF process referred as balling effect. The features of the track instability depend on laser power, scanning speed, powder layer thickness, preheating temperature, substrate material, physical properties and granulomorphometry of the used powder material. (Yadroitsev, Smurov, 2010a, p. 552)

One way to study the single track formation is to define energy density which is needed to melt the single tracks. Energy density which is used in building process can be determined with equation 5.

$$ED = \frac{P}{v \cdot LT \cdot h} \tag{5}$$

where *ED* energy density,

P laser power,

v laser scan velocity,

LT layer thickness,

h hatch distance.

When scanning single tracks, hatch distance is equal to the used lasers spot size. (Ciurana et al. 2013, p. 1107)

Understanding of the mechanisms of single track formation in PBF process gives basis for usage of wider range of commercially available powders and also basic knowledge to improve process efficiency by modifying the parameters of the building process. (Yadroitsev, Smurov, 2010a, p.552-553)

3.3.1 Influence of laser scan speed in single track formation

If the laser power is too low, it is sufficient to melt the powder but not enough to melt the substrate and to create a metallic joint via molten pool. In other words, the build layer is not attached to the previous one. Too low laser power combined to mismatching scanning speed causes irregularities in track formation in the process. In studies by Yadroitsev et al. (Yadroitsev et al., 2010a, 2010b, 2013) the single track formation is closely studied. In these studies 50 W laser has been used to test track formations with different laser powers, scanning speeds and layer thicknesses. (Yadroitsev et al., 2010a, 2010b, 2013, Li et al. 2012, p.1030)

When trying to control the process parameters, it is known that formation of single tracks from metal powder by LAM has a threshold character. There exist a set of process parameters for each powder material, which produce stable and unstable tracks. The formation of spatters which are in contact to the track or very close to it could eventually form pores in 3D parts and increase surface roughness. Figure 8 shows instability of single track formation. (Yadroitsev et al. 2013, p. 607)

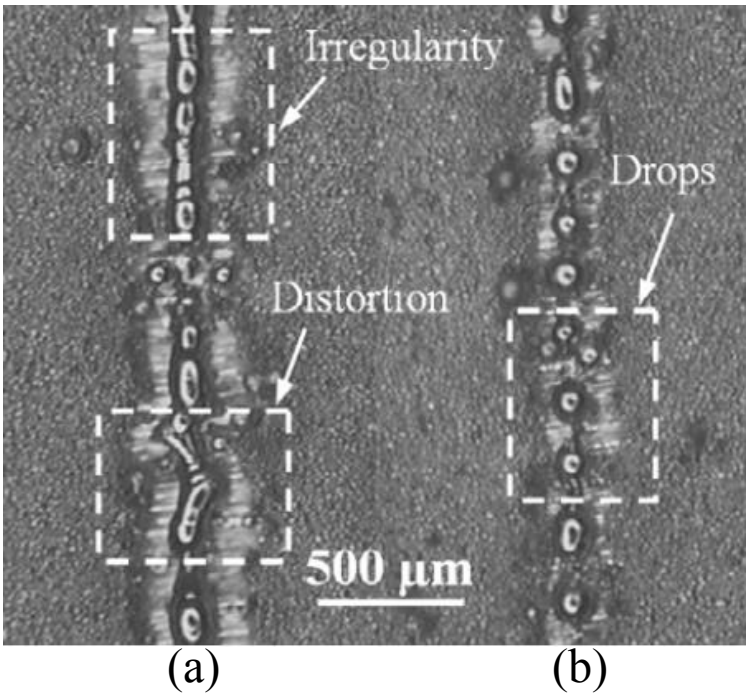

Figure 8. Instability of single tracks from SS 316L powder on steel substrate. Layer thickness is 50 µm, scan speed 0.02 m/s, laser beam spot size 70 µm, (a) P = 25 W, (b) P = 12.5 W (Yadroitsev et al., 2010b, p. 1629).

Yadroitsev and Smurov (Yadroitsev, Smurov, 2010a, p. 554) noticed that increasing the energy input per unit length at relatively high laser power and slow scanning speed, the LAM process is accompanied by an increase of the melt volume and a decrease of the melt viscosity. This leads to the irregularities of the melted tracks. Energy becomes insufficient to melt the substrate with small laser power and small scanning speed and the penetration into the substrate disappears. If the laser energy is enough to maintain the boiling and evaporation of the molten powder, the vapor recoil pressure causes distortion and irregularities of the tracks. When decreasing the laser power further the tracks become a sequence of drops as seen in figure 8 (b). (Yadroitsev et al. 2010b, p. 1629)

The drop formation can cause also balling effect in PBF process. The balling phenomena can cause increase in surface roughness, poor mechanical properties of manufactured part and if the balling is severe enough it can cause jamming in the powder spreading process. The jamming of the powder spreading process can in turn cause part fracturing when the recoater hits the layer where the balling effect has been occurred. The building process can also stop if the recoater jams to the surface of previous layer or it bends or fractures part. Figure 9 shows defect caused by balling phenomena. (Li et al., 2012, p. 1026-1027)

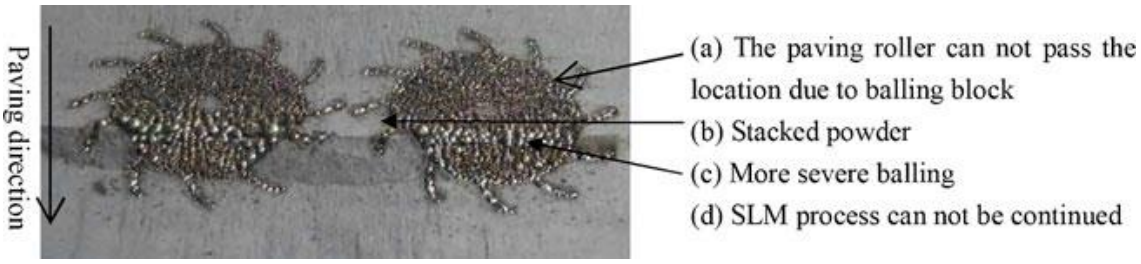

Figure 9. Balling defect on cross-section of parts being built with PBF (Li et al. 2012, p.1028).

The balling defect is formed in PBF process, when combination of process parameters is not compatible with each other. The parameters are for example laser power, scan speed, scan interval, layer thickness and oxygen content in building chamber. (Li et al. 2012, p. 1028-1029)

3.3.2 Influence of the powder layer thickness on the single track formation

Because the PBF process is layer by layer process, the layer thickness is one determinant factor in this process. Layer thickness has significant influence on the melt pool stability and furthermore to the formation of balling effect. The layer thickness should be based on thorough consideration of the particle size and the shrinkage extent during synthesis to achieve continuous tracks. The thickness of deposited layer determines how much powder is melted with single scan. The layer thickness with other important parameters such as laser power, scan speed and scan spacing effects also in part density. Since there is no mechanical pressure involved in PBF processes, it is difficult to achieve 100 % dense parts. The part densification is formed by temperature effects, gravity and capillary forces. If the layer is too thick, it is possible that during the part building laser energy is too low to melt the layer completely and cause pores and balling of the powder. Also if the part surface is rough and powder is not spread homogenously, it is possible that gas is entrapped in thicker sections, and when the layer is scanned, the entrapped gas is superheated and it expands rapidly removing the molten metal above it thus creating a pore. Figure 10 shows effect of scan speed and layer thickness on the relative density of AISI 316L stainless steel manufactured sample. (Li et al. 2012, p. 1032, Kruth et al. 2010, p. 2)

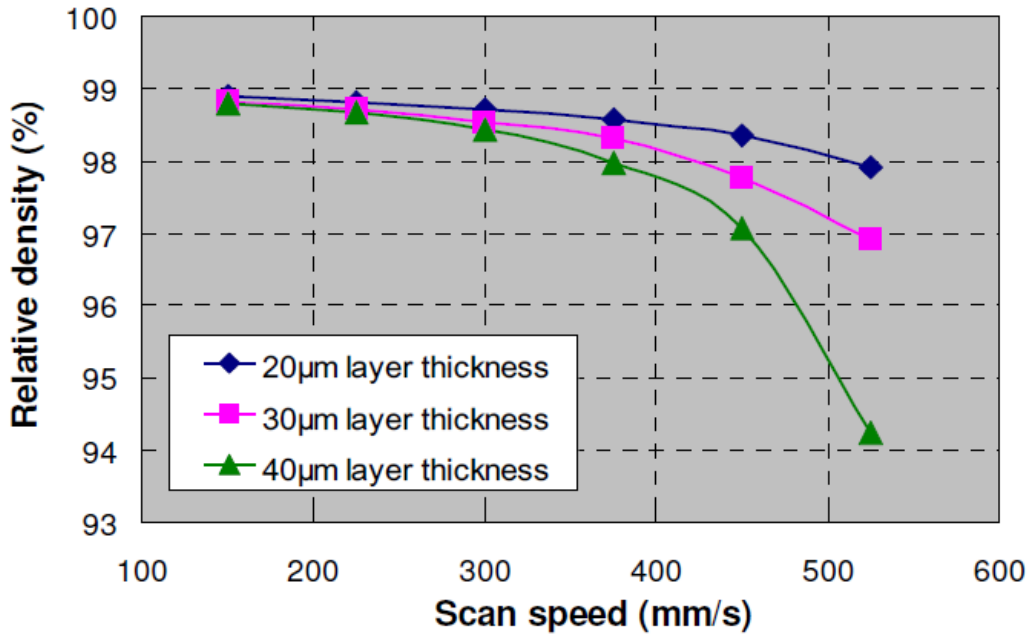

Figure 10. Effect of scan speed and layer thickness on relative density of SS 316L (Kruth et al. 2010, p. 2).

As it can be seen from figure 10, at sufficiently low scan speeds the relative density is almost independent with the selected range of layer thicknesses. At higher scan speeds the thicker layer thickness results in lower density with constant laser power. (Kruth et al. 2010, p. 3)

The effect of layer thickness on single track formation and balling effect is studied by Li et al., Yadroitsev et al. and Ciurana et al. (Li et al. 2012, p.1032, Yadroitsev et al. 2010a, p. 555, Ciurana et al., 2013, p.1103-1110). In these studies the effect of layer thickness is studied with sloped steel substrate where the single tracks are scanned. In figure 11 is presented the schematic diagram of substrate plate used in Ciurana et al. researches.

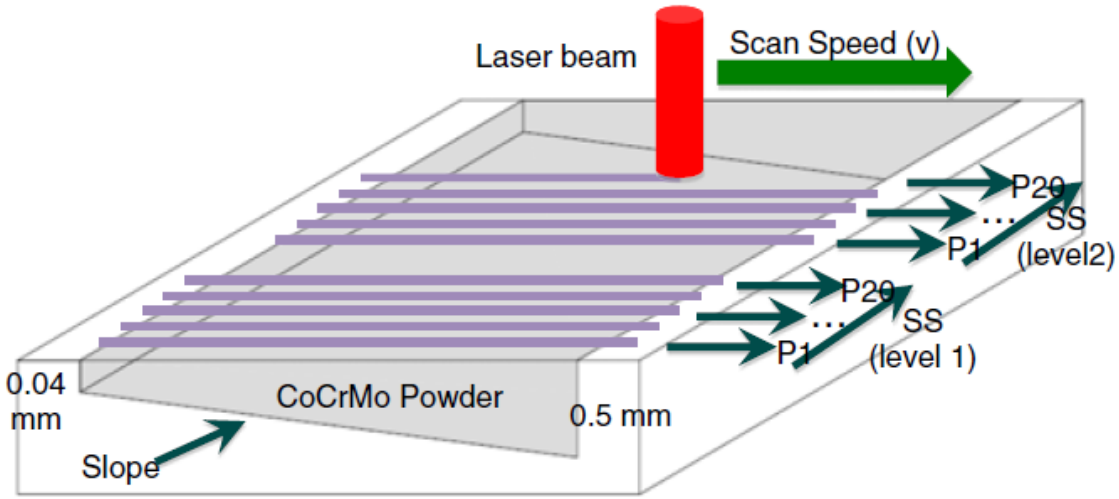

Figure 11. Schematic diagram of the sloped substrate plate (Ciurana et al. 2013, p. 1105).

The sloped substrate plate produces gradient layer thickness as shown in figure 11. In the experiments single scan lines are made on the substrate to verify the effect of layer thickness on the balling. (Ciurana et al. 2013, p.1105) In experiments of Li et al. (Li et al. 2012, p. 1032-1033) the used laser power was set to constant 190 W and scan speed into 50 mm/s. In these experiments it was noticed that layer thickness has big effect on single track formation and balling effect. Scan tracks of study by Li et al. are shown in figure 12. (Li et al. 2012, p. 1033)

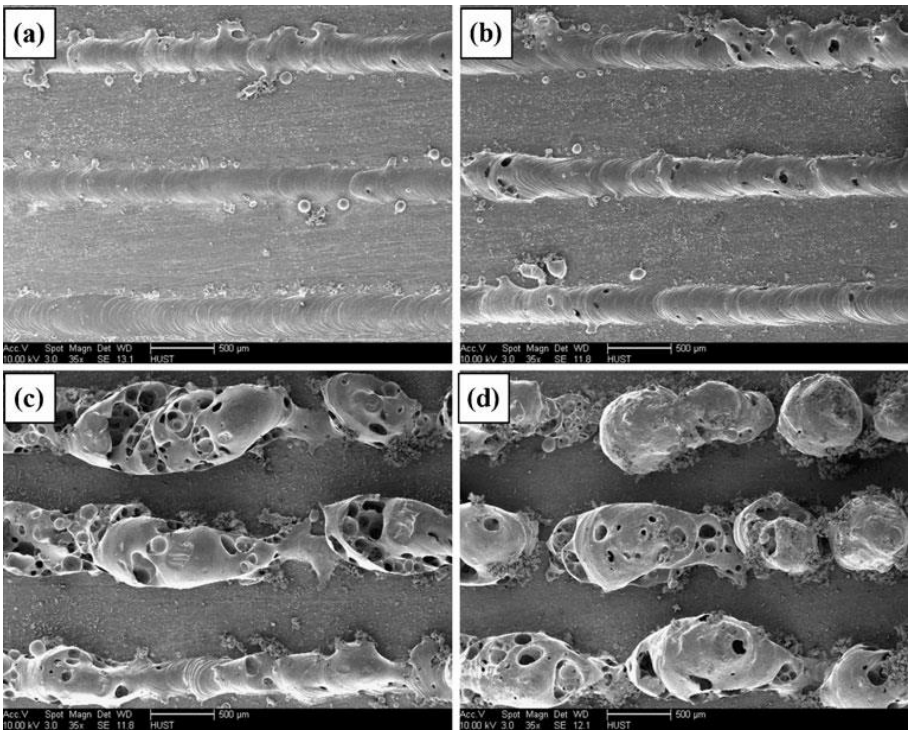

Figure 12. SEM images of layer thickness effects on single track formation of nickel powder. The layer thickness is increased gradually from a) to d) (Li et al. 2012, p. 1034).

As it can be seen from figure 12, it is possible to achieve smooth continuous tracks with thinner layer thickness. Several agglomerates and pores can be seen on thicker layer thicknesses. This indicated worsened wetting ability. This means that there is not enough laser energy to melt the whole thickness of the powder layer. This leads to weak flow ability and balling phenomena. Even though thicker layer thickness could enable big melt pool, the melt pool is relatively far away from the previous layer or substrate. In this condition the small wetting area cannot support a large melt pool and therefore the scan track tends to break into balls. Figure 13 illustrates schematic diagram about effect on layer thickness on the wetting condition. (Li et al. 2012, p. 1033)

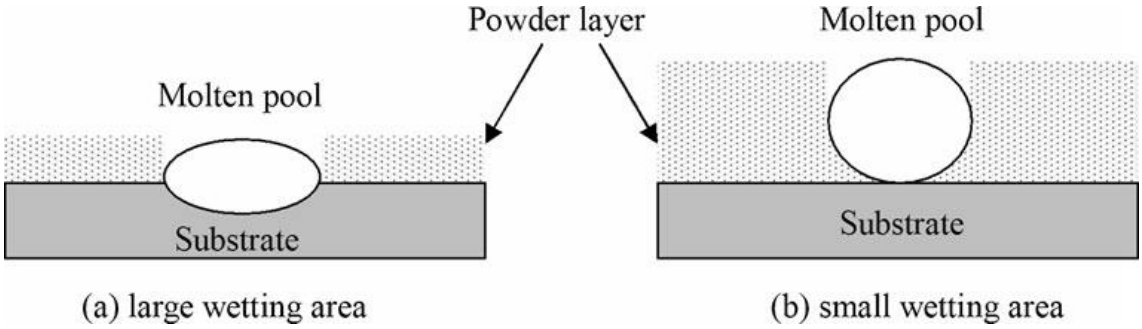

Figure 13. Effect of layer thickness on the wetting condition (Li et al. 2012, p. 1033).

In studies by Yadroitsev et al. (Yadroitsev et al. 2010a, 2010b), similar results are achieved when laser power is set to constant. In these studies scan speed and layer thickness are varied in single track tests. Figure 14 represents scan tracks with varied scanning speeds and layer thicknesses.

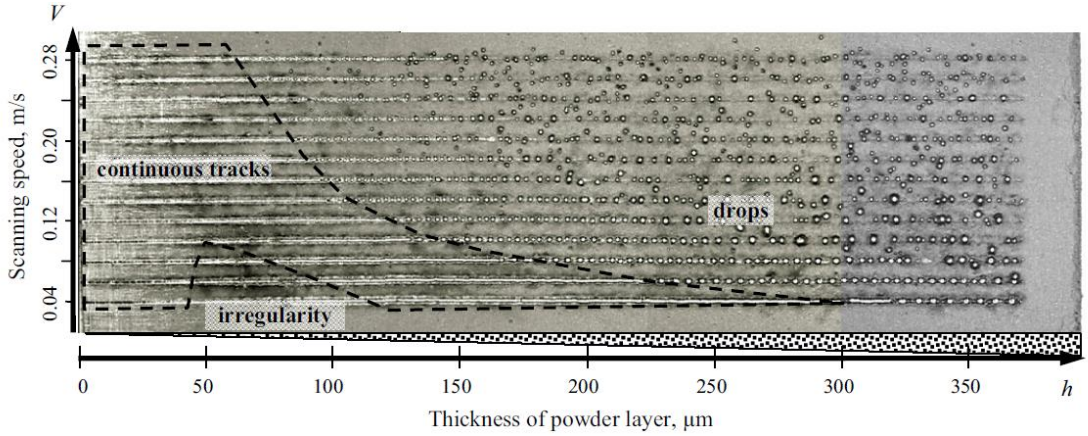

Figure 14. Top view of single tracks from SS 316L on sloped steel substrate (Yadroitsev, Smurov, 2010a, p. 555).

It can be observed from figure 14 that both scanning speed and layer thickness has remarkable effect on single track formation with constant laser power. The used laser power in these tests was 50 W and the powder layer thickness varied from 0 µm to 400 µm, also the scan speed was varied from 0.04 to 0.28 m/s. At the layer thickness less than 50 µm practically all of the powder grain particles interact with laser radiation within the laser beam spot. If the optimum energy balance is achieved, it is possible to achieve continuous tracks. If there is excessive energy, the scanned tracks may be distorted and irregular. As it can be seen from figure 14, with laser power 50 W, irregularities are formed at low scanning speed 0.04 m/s and 0.06 m/s in layer thicknesses 40-120 µm and 40-90 µm, respectively. In study by Yadroitsev and Smurov (Yadroitsev, Smurov, 2010a) the critical minimal and maximal layer thicknesses that produced continuous single tracks at scan speed of 0.04 m/s are 0-40 µm and 120-300 µm respectively. Higher power laser is more preferable in order to vary the scanning speed and layer thickness. (Yadroitsev, Smurov, 2010a, p. 554-555)

3.3.2 Scan vector length and skin-core scanning strategy

As mentioned earlier, the main driver to increase build rate in PBF process is to increase the layer thickness. Therefore it is crucial to solve the problem of the amount of energy required to high quality process. According to Schleifenbaum et al. (Schleifenbaum et al.

2011), the scan vector length has big influence on process stability and manufactured part density. A short scan vector length causes the laser beam to alter its direction more often and this means that the number of reversal points is increasing with decrease of the scan vector length. An increase of temperature is observed in that area of the reversal point, since the laser beam interaction time is longer than in regular scan area. This superheating causes more powder particles to evaporate which results in process instabilities such as spattering and pore formation. This is why increasing the scan vector length and therefore decreasing the reversal point amount is preferable. Figure 15 illustrates part density as a function of the layer thickness and different scan vector lengths. (Schleifenbaum et al. 2011, p.366, Kelbassa et al. 2012, p.3)

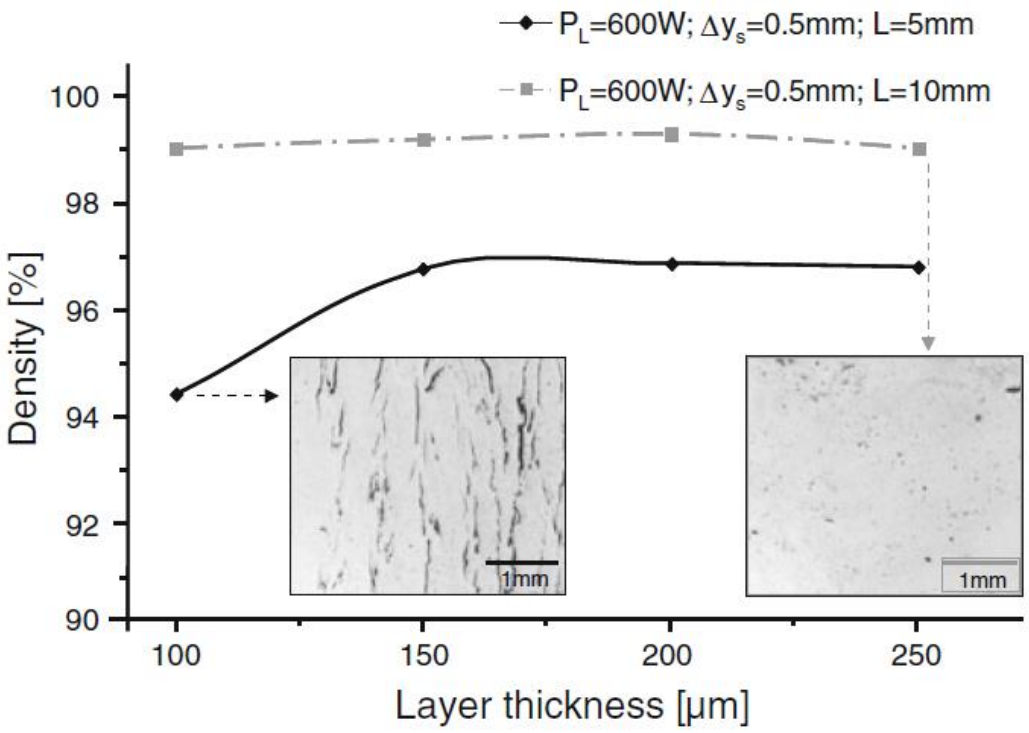

Figure 15. Part density as function of layer thickness and different scan vector lengths (Schleifenbaum et al. 2011, p. 367).

As it can be seen from figure 15, the black graph shows that layer thickness and scan vector length have influence on part density when laser power is constant 600 W and scanning speed is fixed. It can be seen that density of manufactured part increases from approximately 94% to 97 % when layer thickness is increased from 100 µm to 150 µm due to higher energy that is required to melt the powder mass per scan line. At the same time the superheating, evaporation and spattering decreases and the process becomes also more stable. (Schleifenbaum et al. 2011, p. 367)

When using the same process parameters, only varying the scan vector length from 5 mm to 10 mm, a major improvement can be noticed. As it can be seen from figure 15, the grey dotted line shows that the density remains almost uniform from layer thickness 100 µm to 250 µm when scan vector length is 10 mm. At layer thickness 100 µm the difference between 5 mm and 10 mm scan vector length in part density is approximately 5 %. This is because the process becomes more stable and such superheating and evaporation does not happen as in with 5 mm scan vector lengths. With this change it is possible to manufacture parts with approvable density. (Schleifenbaum et al. 2011, p. 367)

The build rate of PBF process can be increased by means of higher power lasers and larger beam diameter. Longer scan vectors should also be applied especially if the layer thickness is less than 150 µm. Again, when using thicker layers the accuracy and detail resolution suffers and it is not possible to manufacture parts with complex geometry with approvable accuracy. This is where the skin-core scanning strategy should be applied. In this technique the core of the part is manufactured with larger beam diameter e.g. 1 mm. The outer section, skin, is manufactured with smaller beam diameter and thinner layer thickness. The layer thickness of the core can only be multiplies of the layer thickness of skin area. For example if the skin layer thickness is 50 µm the core layer thickness can be 100 µm, 150 µm, 200 µm, etc. In figure 16 is presented schematic illustration of skin-core scanning principle. (Schleifenbaum et al. 2010, p.168)

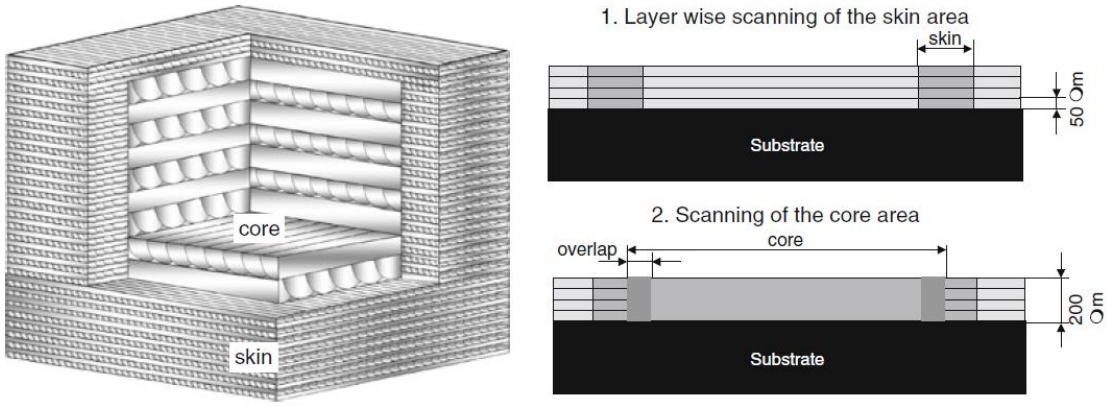

Figure 16. Schematic illustration of skin core principle (left) and procedure of scan strategy (right) (Schleifenbaum et al. 2011, p.368).

Also very crucial factor in this kind of scanning strategy is to create metallurgical bonding between the skin and core sections of manufactured object. This is solved with overlapping the interface of the skin and core. This means that the interface area is scanned twice as seen in figure 16 on the right. The overlap has to be > 0 mm, in order to achieve acceptable metallurgical bonding. The amount of overlap is dependent on layer

thickness ratio of skin and core. In studies by Schleifenbaum et al. (2011) and Kelbassa et al. (2013) the studied skin-core layer thickness ratios are 1:2 and 1:4. In both cases the number and size of defects and porosity is decreasing with increase of overlap. In figure 17 is presented density of skin-core interface on different layer thickness ratios. (Kelbassa et al. 2012, p. 3, Schleifenbaum et al. 2011, p. 368)

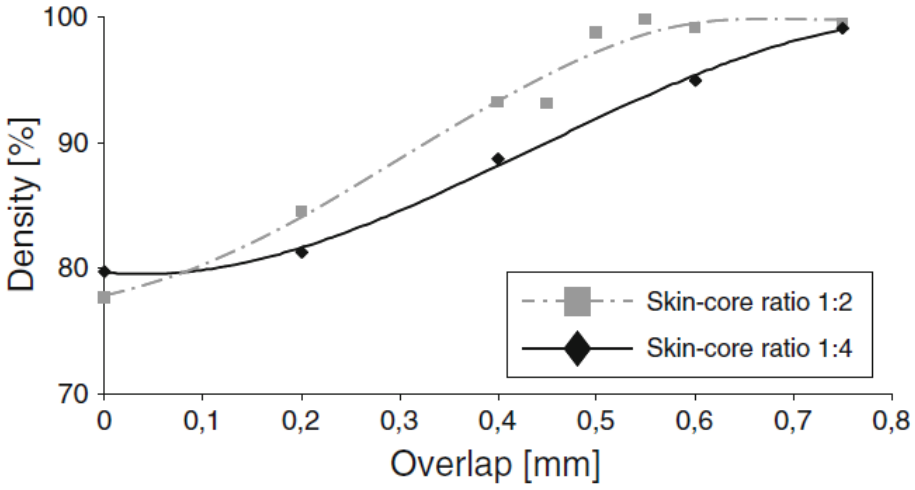

Figure 17. Density of skin-core interface area with layer thickness ratios 1:2 and 1:4 (Schleifenbaum et al. 2011, p. 368).

As it can be seen from figure 17, it is possible to achieve dense metallurgical bonding between skin and core with overlap > 0.5 mm on layer thickness ratio 1:2, which are in this case 50 µm and 100 µm. When skin-core layer thickness ratio is increased to 1:4, which is in this case 50 µm and 200 µm, it is possible to assure 99 % density with overlap > 0.75 mm. In figure 18 is presented cross-sections of skin-core specimen with a layer thickness proportion of 1:2 (left) and 1:4 (right). (Schleifenbaum et al. 2011, p.369)

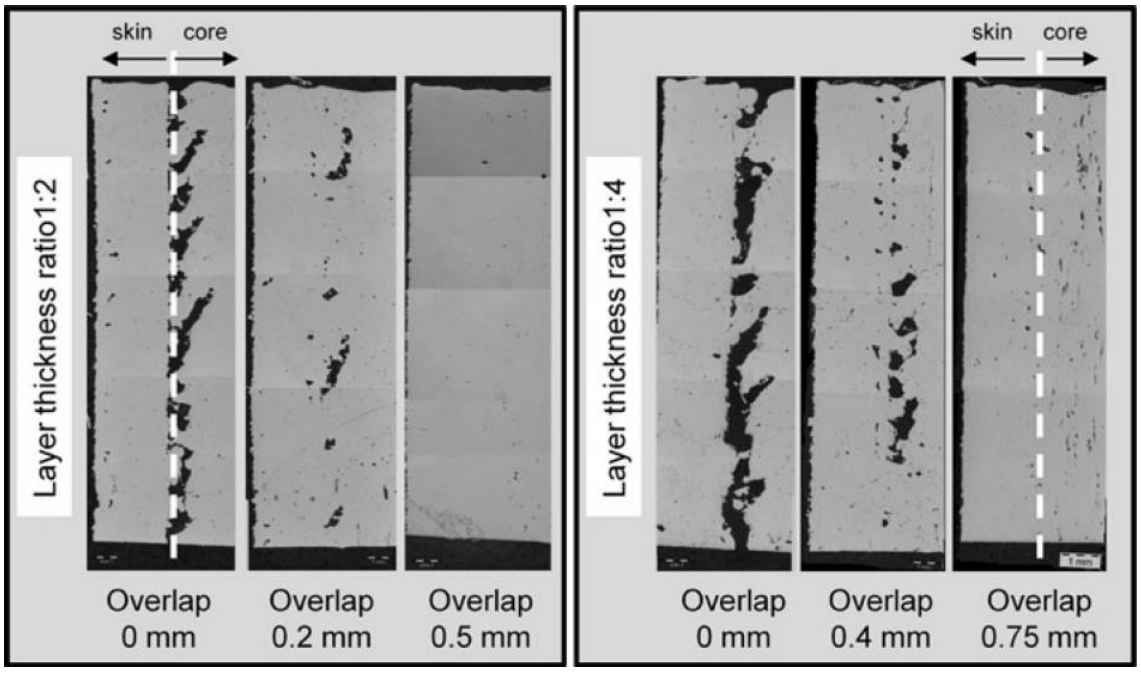

Figure 18. Cross-section of skin-core specimen (Schleifenbaum et al. 2011, p.369).

As it can be seen from figure 18, it is possible to manufacture nearly dense parts with skin-core scan strategy and with layer thickness ratio 1:4 when overlap of the skin-core interface is > 0.75 mm. Besides this skin-core specimen, Schleifenbaum et al. (2011) and Kelbassa et al. (2013) have manufactured injection mold insert, where the capabilities of skin-core scanning are applied. In figure 19 is presented the injection molding tool model. (Schleifenbaum et al. 2011, p. 369, Kelbassa et al. 2012, p. 3-4)

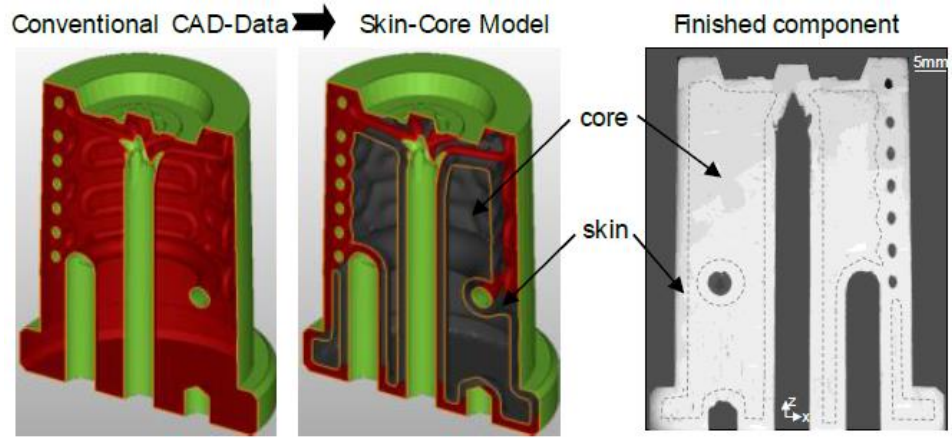

Figure 19. Injection molding tool with internal cooling channels (left: conventional CAD model, middle: skin-core model, right: cross-section of manufactured component) (Kelbassa et al. 2013, p. 4).

As it can be observed from figure 19, the conventional CAD model is transferred into skin-core model and then manufactured with layer thickness ratio 1:4 where layer thicknesses are 50 µm and 200 µm. The overlap of the skin-core interface is set to 0.75

mm. As it can be seen from figure 19 right, the manufactured piece is full dense, even the bonding of skin-core interface is succeed. Build ratio was also measured in this study. Core of the part was built 16. 8 mm^3/s and skin of the part was build 3 mm^3/s. The overall build ratio of the tooling insert sums to 10. 2 mm^3/s, which is multiple times faster than with SLM machines, using less than 400 W laser power. (Kelbassa et al. 2012, p. 4-5, Schleifenbaum et al. 2011, p. 369-370)

EXPERIMENTAL PART

4 AIM AND PURPOSE OF THIS STUDY

Aim of this study was to determine the methods for LAM process efficiency improvements. This aim has been approached by studying laser beam-material-interaction. It was decided to manufacture test pieces where input parameters such as laser power and scanning speed were varied and the formation and penetration of formed single tracks were studied. Also the manufacturability of skin-core test pieces was studied. Test pieces were manufactured with prototype LAM machine, similar to EOS EOSINT M-series machines, and with EOS EOSINT M 280 machine. All of the test pieces were manufactured from EOS 17-4 PH stainless steel powder.

5 EXPERIMENTAL PROCEDURE

5.1 Laser beam- material-interaction model

One of the goals of in this study was to determine the formation of the single exposed track. Also investigating of the depth of penetration and the width of the single exposed track was set as a target. Aim was also to gain basic understanding of the effect of different laser parameters in the laser additive manufacturing process. Piili (Piili, 2013) created a model for laser-material-interaction in her thesis and a modified model from that was created for this study. Figure 20 presents laser beam-material-interaction model, which was used as base, when studying effect of different parameters in LAM process.

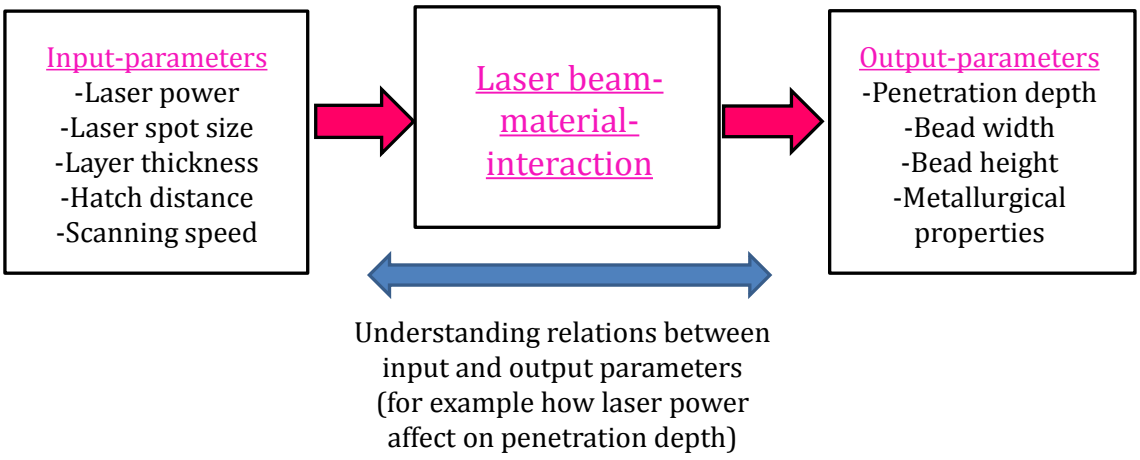

Figure 20. Laser beam-material-interaction parameters.

Understanding the relation of input and output parameters described in figure 20 is important, when analyzing the process. It is possible to model and analyze the phenomena with help of this understanding in interaction of laser beam and metal powder material and later on optimize the process efficiency.

5.2 Material

Material used in this study was EOS StainlessSteel 17-4 PH stainless steel powder. Composition of this powder is similar to US classification 17-4 PH and European 1.4542 stainless steel materials. The chemical composition of the material is shown in table 1.

Table 1. Material composition of EOS 17-4 PH (EOS Finland).

Material	Fe	Ni	Mo	Cu	Cr	Mn	Si	C	P	S	O	N	Nb
Composition [%]	73.7	4.2	0.4	3.9	15.8	0.7	0.7	0.01	0.02	0.01	0.04	0.14	0.29

This powder is a pre-alloyed stainless steel and this type of material is widely used in engineering applications where high toughness, ductility and corrosion resistance is required. Suitable applications can be found for example from medical or mold making industry. This material can also be used for building functional prototypes, small series products and individually designed products and spare parts. It is possible to use layer thickness of 20 µm with standard processing parameters but it is also possible to use skin-core building strategy to increase build speed. Mechanical properties of built parts are fairly uniform in all directions, when using standard process parameters. Parts manufactured from this powder can be welded, machined, shot peened, polished and coated if necessary. (EOS Material data sheet)

5.3 LAM equipment

Laser additive manufacturing systems used in this thesis consists of laser unit, process chamber and process control computer. Two different LAM systems were used in this study. These LAM systems were equipped with 200 W and 400 W fiber laser sources.

5.3.1 Basic principle of LAM equipment

Building process takes place in the process chamber with both systems and the process is controlled by computer. The building chamber is divided into three platforms, where the middle one is the platform where the parts are built. The building chamber of LAM equipment at LUT Laser is presented in figure 21.

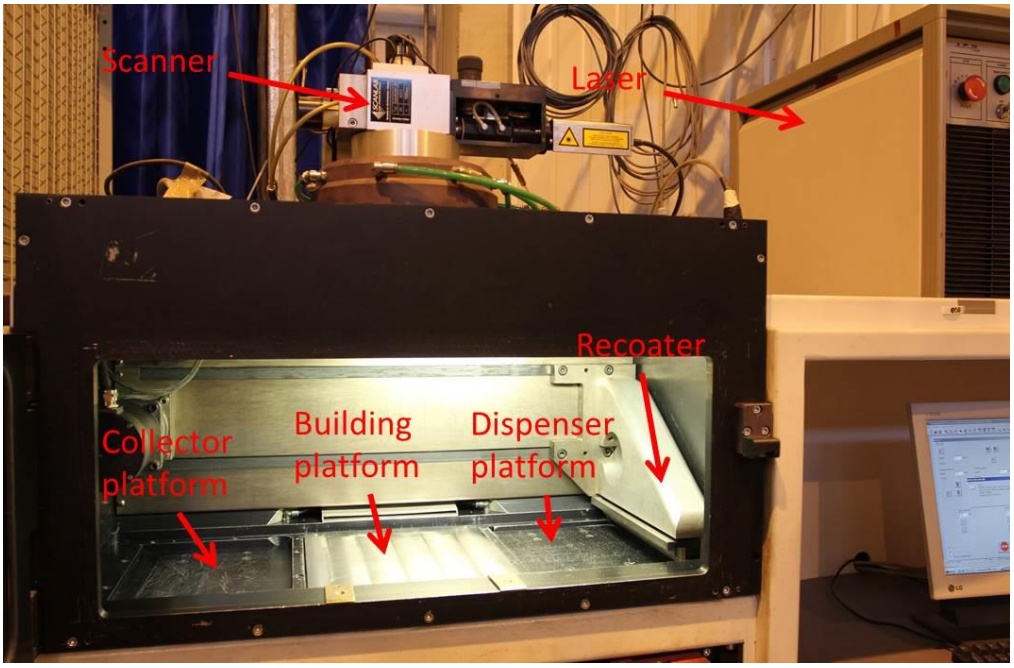

Figure 21. Process chamber of LUT Laser LAM system.

The other two platforms serve as powder dispenser platform and as collector platform where the extra powder is collected. The powder spreading is done with recoater, which spreads the powder evenly to the building platform. The building platform is heated with thermo elements. The chamber is filled with nitrogen gas to decrease the oxygen level of the chamber atmosphere. The nitrogen is provided by nitrogen generator of LAM equipment. The level of nitrogen is 99.8 % during the building process. Nitrogen works as a protective gas and it helps to avoid oxidation of the stainless steel parts.

5.3.2 LAM equipment of LUT

LAM equipment with 200 W fiber laser source is situated in LUT Laser laboratory in Lappeenranta University of Technology and it is experimental prototype system by EOS GmbH. This prototype equipment is similar to EOS EOSINT M-series device and it is equipped with IPG YLS-200-SM-CW fiber laser and Scanlab hurrySCAN 20 scanner. This laser unit produces 200 W power at a wavelength of 1070 nm and the focal length is 400 mm. The LAM equipment situated in LUT Laser is presented in figure 22.

Figure 22. Prototype LAM equipment, similar to EOSINT M-series equipment.

5.3.2 LAM equipment of EOS Finland

The LAM system with 400 W fiber laser source is located in EOS Finland in Turku, Finland. This equipment is commercially available EOS EOSINT M280 system. The LAM equipment situated in EOS Finland is presented in figure 23.

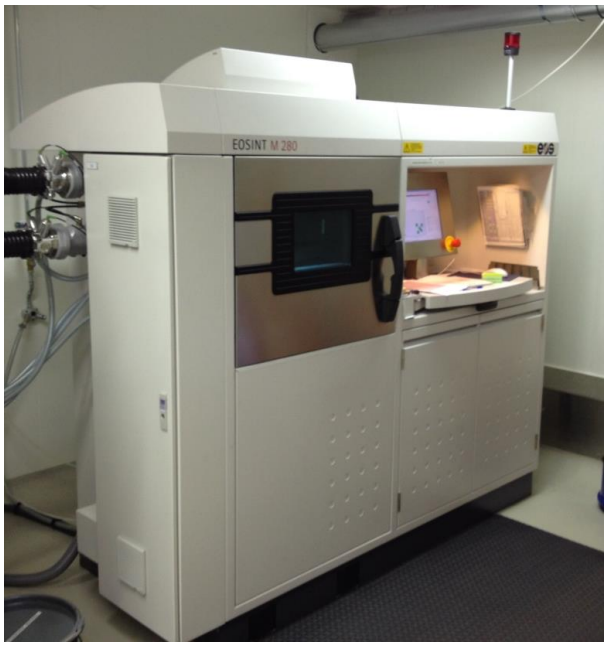

Figure 23. LAM equipment EOS EOSINT M280 located in EOS Finland.

5.4 Geometry of used test-pieces

It was decided to manufacture single track test pieces by altering heat input to be able to determine the effect of heat input on the single track formation and penetration depth. These single tracks were made on top of 20 x 40 x 15 mm bulk piece. The 3D model of single track test piece is shown in figure 24.

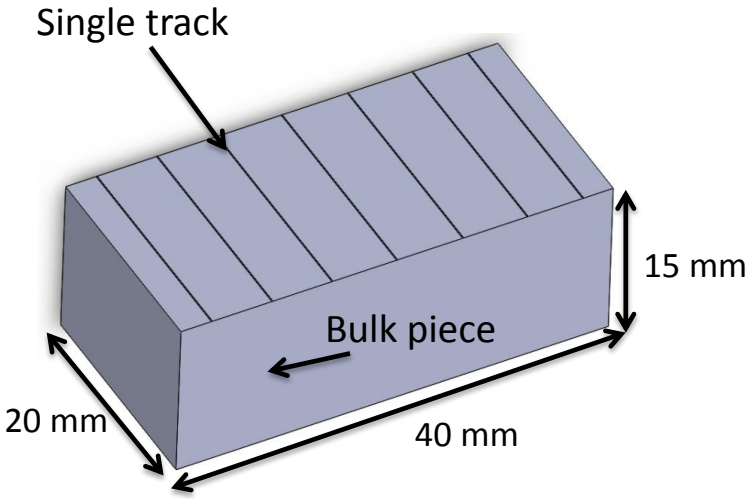

Figure 24. 3D model of the single track test piece.

Skin-core test pieces were also manufactured for this thesis. Skin-core building strategy is building strategy where part was divided into skin and core. The skin of the part was

manufactured with thinner layer thickness to be able to maintain the high quality and accuracy of the part. The core of the part is manufactured with thicker layer thickness which gives possibility to speed up the process. The skin-core test piece was made so that the skin of the part was 20 x 20 x 20 mm with 17 x 17 x 20 mm hole in the middle. The core of the part was 17 x 17 x 20 mm and it was placed to the hole of the skin part. The skin-core test piece is shown in figure 25.

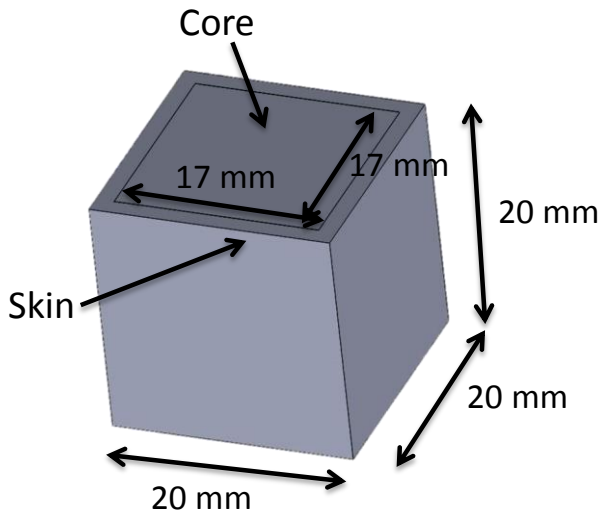

Figure 25. 3D model of skin-core test piece.

The skin was manufactured in skin-core test piece with standard parameters and layer thickness of 20 µm. Core of the part was manufactured by varying heat input and with layer thickness of 40 µm.

5.5 Heat treatment

It was decided to perform heat treatment to one of the single track test pieces. The heat treated test piece was heat treated in furnace. The building platform was sawed into pieces such that only the heat treated test piece was set into the furnace. Figure 26 shows the sawed building platform with heat treated test piece and test pieces without heat treatment.

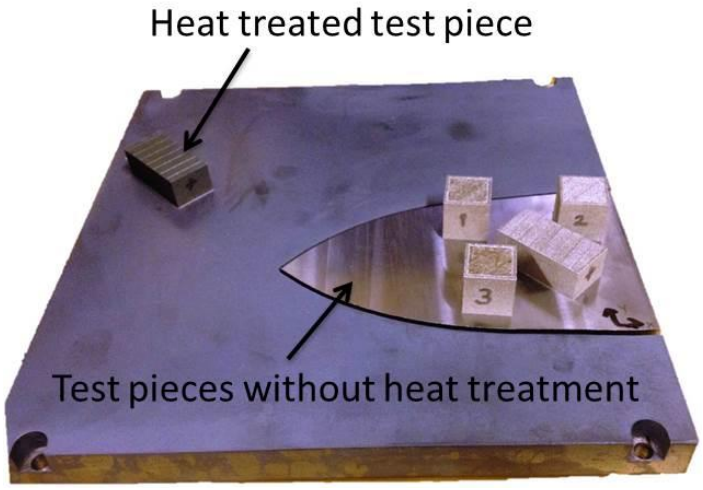

Figure 26. Sawed building platform with test pieces with and without heat treatment.

The purpose of the heat treatment was to smooth the microstructure of the bulk piece so that the single-tracks could be easier to find and analyze with microscope.

The heat treatment was made in furnace where the sawed building platform was placed in box with argon atmosphere to avoid oxidation during the heat treatment. The furnace and the argon filled box are shown in figure 27.

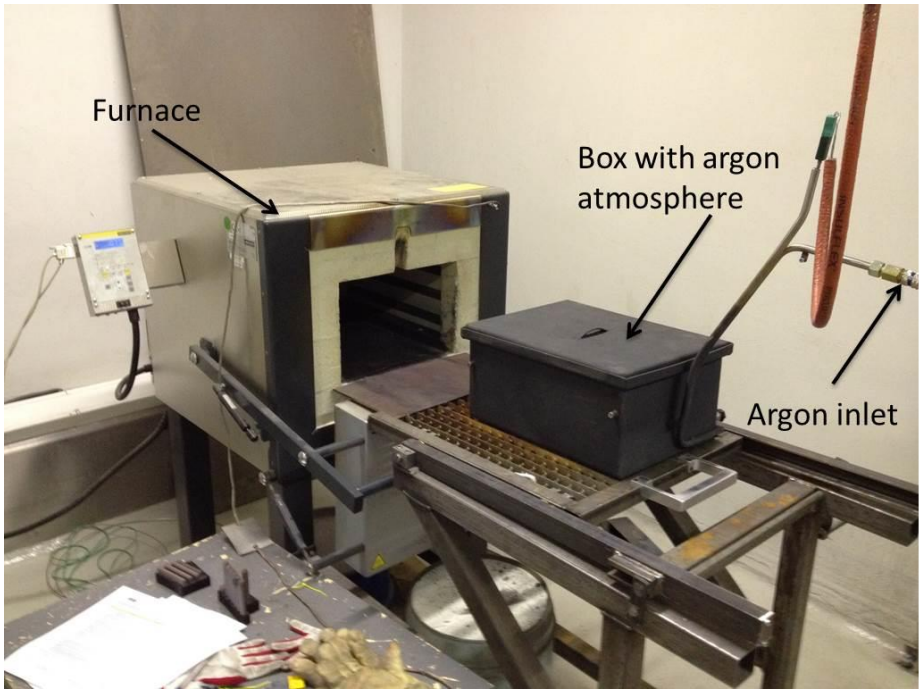

Figure 27. Furnace used in heat treatment.

The heat treatment was performed so that the heat treated test piece was heated into solution annealing temperature to fade the border lines of the scan tracks which have formed during the part building. The solution annealing was made so that the test piece

and the building platform were put in the furnace and the temperature was set to rise into 1038 °C. The test piece was kept in that temperature for one hour and after that it was taken out of the furnace and cooled approximately to 370 °C with argon flow of 30 liters per minute. Cooling to the room temperature was done with compressed air flow. The temperature graph of the heat treatment procedure is shown in appendix IV.

5.6 Analysis equipment

Polished sections were made from the manufactured test pieces so that the pieces were first cut half in longitudinal direction and then polished. All micrographs taken from the polished sections are presented in appendix I. All the measurement results are presented in appendix II. The sections were polished with Struers TegraPol 31 grinding/polishing machine. The polishing machine can be seen in figure 28.

Figure 28. Polishing machine Struers TegraPol 31.

Etching of the test pieces was first made with Kalling's 2 reagent. The single track beads were not visible enough after the first etching to analyze them so it was decided to etch the test pieces again with Fry's reagent. However, even after etching with Fry's reagent, the outlines of the beads were not clear and visible, so it was decided to etch the single track test pieces once more with electro etching using again Kalling's 2 reagent as etchant. Table 2 shows the compositions of the etchants and the etching times. The heat treated

specimen was more difficult to etch than the not heat treated ones. This means that it was more difficult to see the clear edges of the penetration of the single tracks with microscope.

Table 2. Composition and etching times of the etchants.

	Kalling's 2 reagent	Kalling's 2 reagent (electro etching)	Fry's reagent
Cupric chloride $CuCl_2$	5 g	5 g	5 g
Hydrochloric acid HCl	100 ml	100 ml	40 ml
Ethyl alcohol C_2H_5OH	100 ml	100 ml	25 ml
Water	-	-	30 ml
Etching time	10 s	10 s	5 s
Current	-	0.6 A	-
Voltage	-	10 V	-

The polished sections were photographed with Infinity camera coupled with Olympus optical microscope. The imaging software was i-Solution Lite. Optical microscope and imaging system is presented in figure 29.

Figure 29. Optical microscope and imaging system.

The penetration depth, width and height of the bead of the single tracks were measured with AxioVision LE64 microscopy software.

5.7 Parameters of experiments

5.7.1 Single track tests

Basic parameters of this process are marked as St_0 in table 3. The parameters were then varied by keeping the laser power as constant of 200 W in tests made in LUT Laser and 325 W tests made in EOS Finland. The scanning speed was then altered such that energy density also varies. Table 3 shows building parameters in single track tests made in LUT Laser.

Table 3. Building parameters in single track tests made in LUT Laser, with laser power of 200 W.

Parameter	St_{-3}	St_{-2}	St_{-1}	St_0	St_1	St_2	St_3
Laser power [W]	200	200	200	200	200	200	200
Scan speed [mm/s]	1600	1400	1200	1000	800	600	400
Layer thickness [mm]	0.02	0.02	0.02	0.02	0.02	0.02	0.02
Laser beam spot size [mm]	0.1	0.1	0.1	0.1	0.1	0.1	0.1
Energy density [J/mm^3]	63	71	83	100	125	167	250
Laser interaction time [s]	$6.3*10^{-5}$	$7.1*10^{-5}$	$8.3*10^{-5}$	$1*10^{-4}$	$1.3*10^{-4}$	$1.7*10^{-4}$	$2.5*10^{-4}$

Similarly, the single track tests were made in EOS Finland in Turku. Table 4 shows parameters in single track tests made in EOS Finland. Laser interaction time is calculated according to equation 8, and it describes the time that the material is exposed under the laser beam spot while the single track is scanned.

Table 4. Building parameters in single track tests made in EOS Finland, made with laser power of 325 W.

Parameter	St_{-3}	St_{-2}	St_{-1}	St_0	St_1	St_2	St_3
Laser power [W]	325	325	325	325	325	325	325
Scan speed [mm/s]	2600	2275	1950	1625	1300	975	650
Layer thickness [mm]	0.02	0.02	0.02	0.02	0.02	0.02	0.02
Laser beam spot size [mm]	0.1	0.1	0.1	0.1	0.1	0.1	0.1
Energy density [J/mm^3]	63	71	83	100	125	167	250
Laser interaction time [s]	$3.9*10^{-5}$	$4.4*10^{-5}$	$5.1*10^{-5}$	$6.2*10^{-5}$	$7.7*10^{-5}$	$1*10^{-4}$	$1.5*10^{-4}$

The energy densities were maintained the same between tests in LUT Laser and in EOS Finland.

5.7.2 Skin-core tests

The skin-core test pieces were manufactured in EOS Finland and the building parameters are shown in table 5.

Table 5. Building parameters in skin-core tests made in EOS Finland.

Parameter	Skin	Core 1	Core 2	Core 3
Laser power [W]	200	325	325	325
Scan speed [mm/s]	1000	1168	1368	968
Layer thickness [mm]	0.02	0.04	0.04	0.04
Hatch distance [mm]	0.1	0.1	0.1	0.1
Offset [mm]	-	-0.015	-0.015	-0.015
Energy density [J/mm^3]	100	70	59	84

The skin-core building parameters were chosen such that the Core 1 in table 5 includes the nominal parameters for the core building. In Core 2 and Core 3 the energy densities were varied so that they were lower in Core 2 and higher in Core 3. The beam-offset parameter in table 5 is parameter that defines how much the center of the laser beam spot is moved inwards or outwards from the edge of the geometry. In figure 30 is presented illustration of the beam offset parameter.

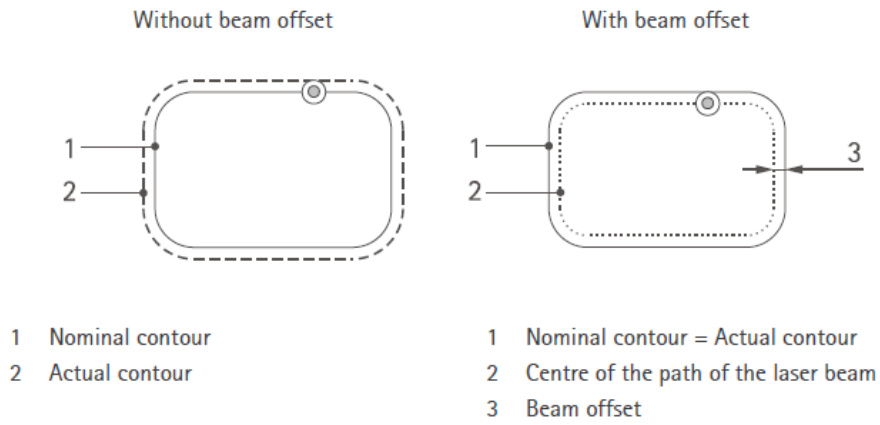

Figure 30. Effect of beam offset parameter (EOS M270/PSW 3.2 Operation manual).

In this case the beam offset is negative which means that the center of the laser beam is moved outwards so that the interface of the skin and core would overlap.

5.8 Equations used in analysis

The energy density input in this thesis was determined according to equation 6. Appendix II shows calculation of energy density.

$$ED = \frac{P}{v \cdot LT \cdot h} \quad (6)$$

In case of single tracks, the hatch distance is set equal as laser beam spot size.

The intensity of the laser beam was defined according to equation 7. Appendix II shows calculation of intensity.

$$I = \frac{P}{A_{Laser}} \quad (7)$$

where I intensity of laser beam,
P laser power,
A_{Laser} area of focused laser beam spot.

The laser interaction time was defined as equation 8 shows. Appendix II shows calculation of laser interaction time.

$$t = \frac{d}{v} \quad (8)$$

where t laser interaction time,
d diameter of laser beam spot,
v laser scanning velocity.

The important feature of the single track tests was to define the penetration depth and single track bead width. Due to this a value of width-depth ratio (*WDR*) was created in this thesis to describe the ratio between bead width and penetration depth. With *WDR* it is easy to conclude when width if the bead is large and penetration is low and vice versa. Figure 31 illustrates the measurements of bead width and penetration depth from where *WDR* is calculated.

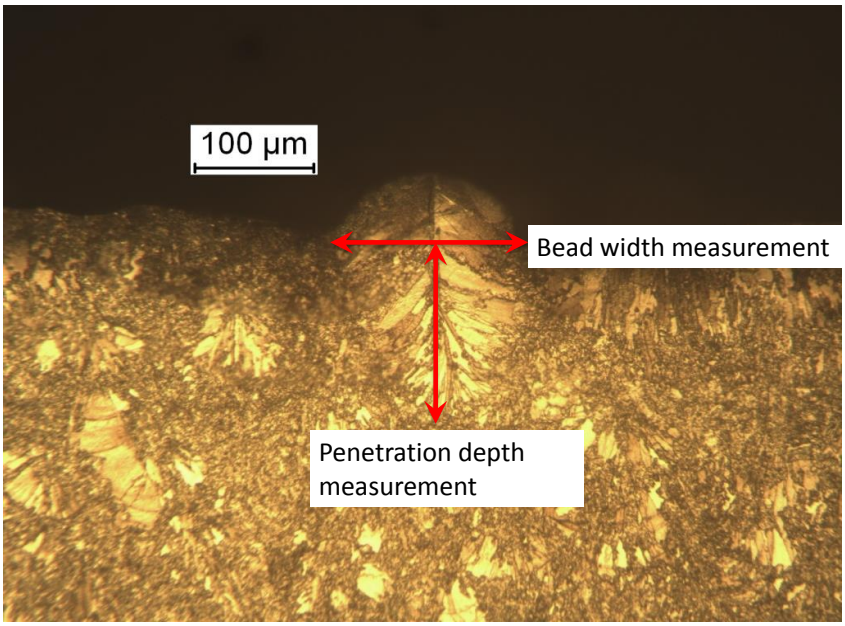

Figure 31. Bead width and penetration depth measurements.

Single track *WDR*s are calculated in order to find out if there is consistency between different specimens. It is calculated as equation 9 illustrates. Appendix II shows calculation of *WDR*.

$$WDR = \frac{BW}{PD} \tag{9}$$

where *WDR* width-depth ratio,
BW bead width,
PD penetration depth.

Figure 32 presents diagram of width-depth ratio, *WDR*.

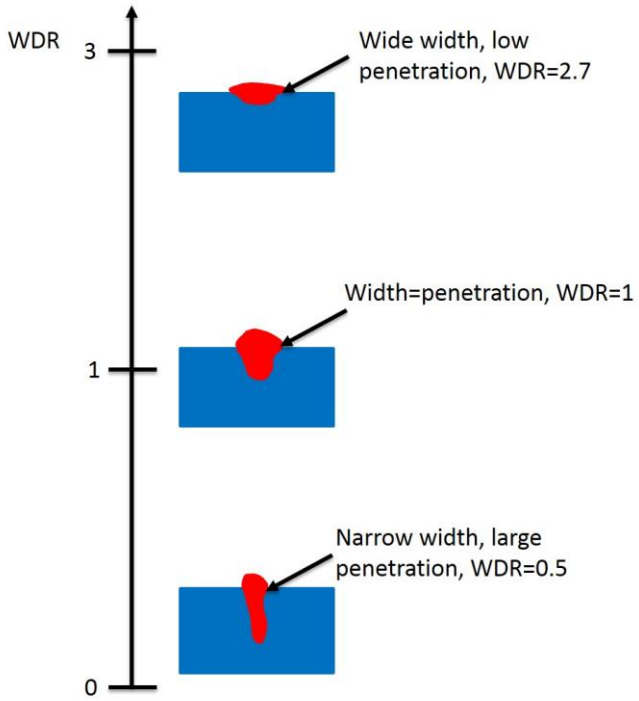

Figure 32. Diagram of small and large *WDR* values.

It was also decided in this thesis to create another value to define the rough area of penetrated bead. Width-depth-area (*WDA*) defines area of the penetration. Bead width and penetration depth is measured as figure 31 shows. *WDA* is calculated as equation 10 illustrates. Appendix II shows calculation of *WDA*.

$$WDA = BW \cdot PD \tag{10}$$

where *WDA* area of penetrated bead,

Figure 33 presents diagram of area of penetration, *WDA*.

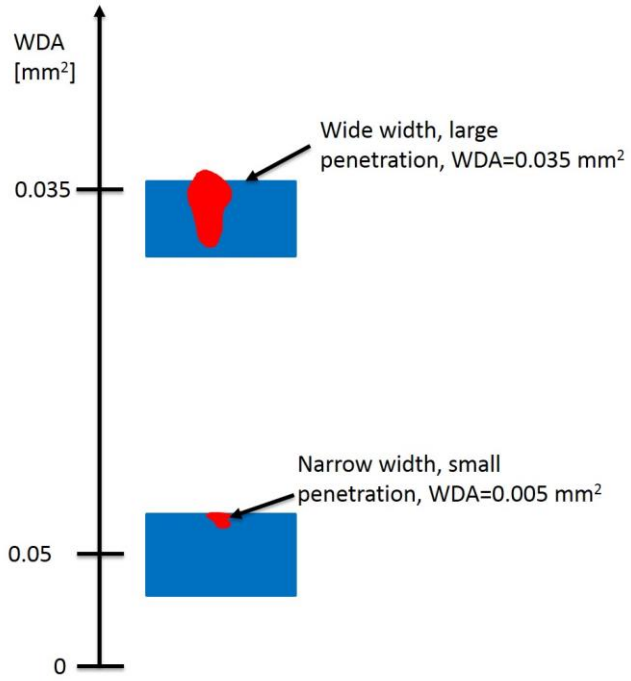

Figure 33. Diagram of small and large *WDA* values.

6 RESULTS AND DISCUSSION

6.1 Single track tests

6.1.1 Energy density vs. penetration depth

The single track specimen made with laser power of 200 W and 325 W were compared against each other, since these test pieces have same energy density inputs and these were not heat treated. Figure 34 illustrates energy density input vs. penetration depth when laser power of 200 W and 325 W were used.

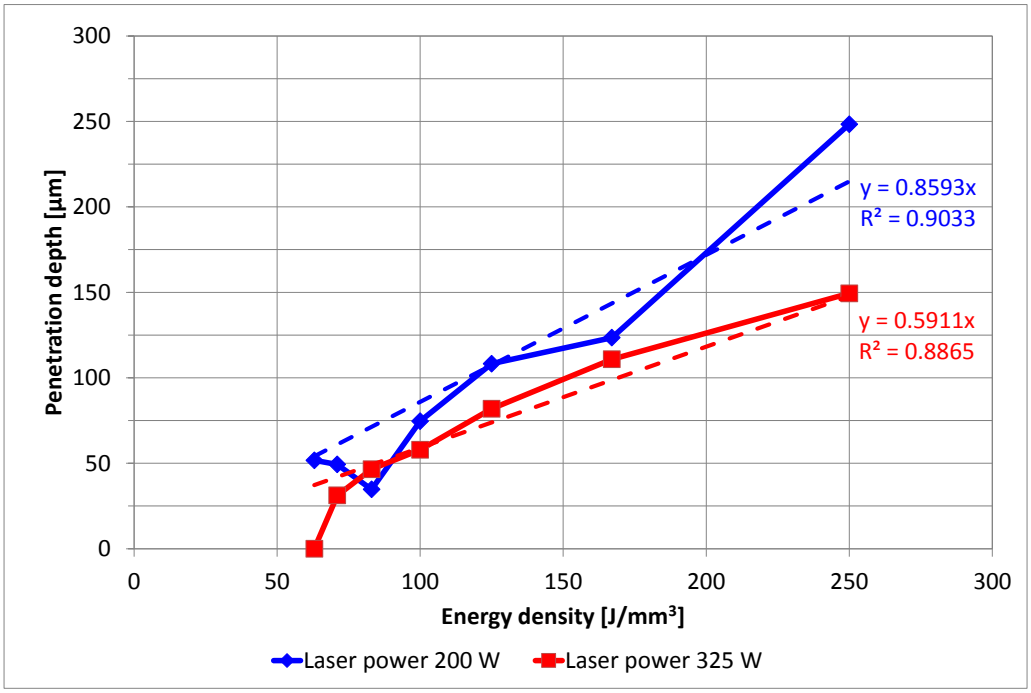

Figure 34. Energy density vs. penetration depth.

As it can be seen from figure 34, the penetration depths of the test piece of 200 W single tracks were almost in every case larger than in test piece of 325 W. This is due to fact that test piece of 200 W single tracks were exposed longer time to laser radiation. Penetration depth increases accordingly, when laser energy density increases. In test piece of 200 W, test of single track made with highest energy density input has penetration depth almost three times larger than test of single track made with the nominal energy density input of 100 J/mm^3.

Penetration depth (325 W) is linearly dependent on energy density. Single track made with smallest energy density input could not be measured in this test piece, since the track penetrated only so little to the bulk piece that it could not be seen with used microscope. The penetration depths between test piece 200 W and 325 W have differences between 10-20 µm, when the energy density input is 167 J/mm^3 or less. When the energy density input increases from 167 J/mm^3, the penetration depth increases in test piece 200 W.

Figure 35 shows energy density input vs. penetration depth when laser power of 200 W and 325 W were used.

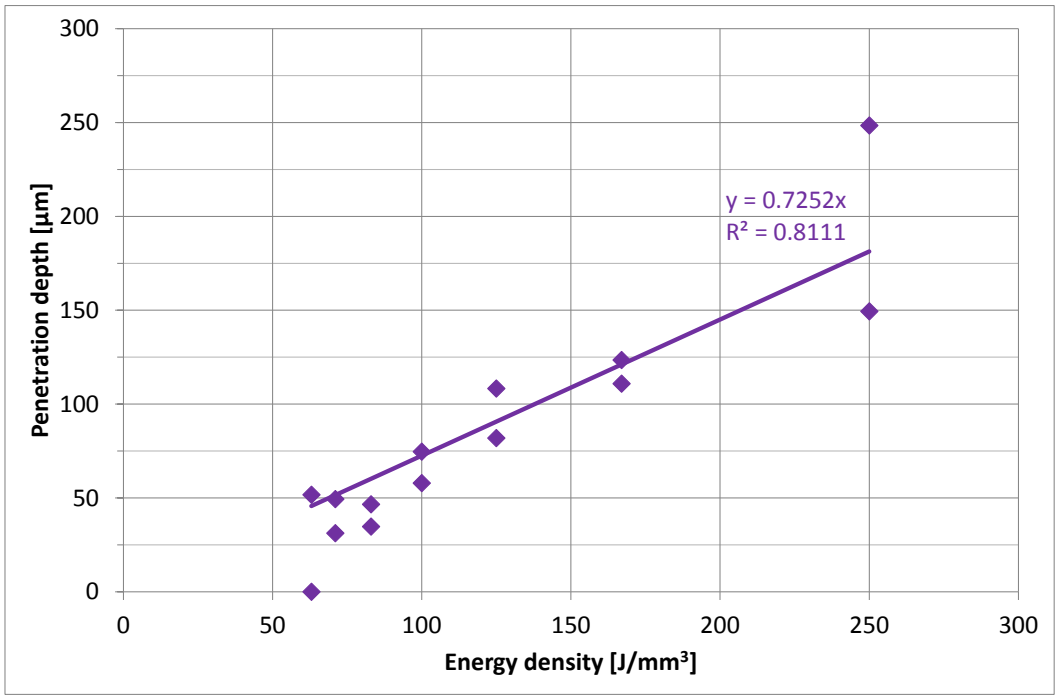

Figure 35. Energy density input vs. penetration depth.

As it can be observed from figure 35, the penetration depth increases as energy density input increases. The increase of penetration depth is linear, when energy density increases. It can also be seen from the figure 35 that when the energy density input is 250 J/mm^3 the penetration depth is almost three times deeper than when the energy density input is the nominal value of 100 J/mm^3.

6.1.2 Laser interaction time vs. penetration depth

Figure 36 shows laser interaction time vs. penetration depth when laser power of 200 W and 325 W were used.

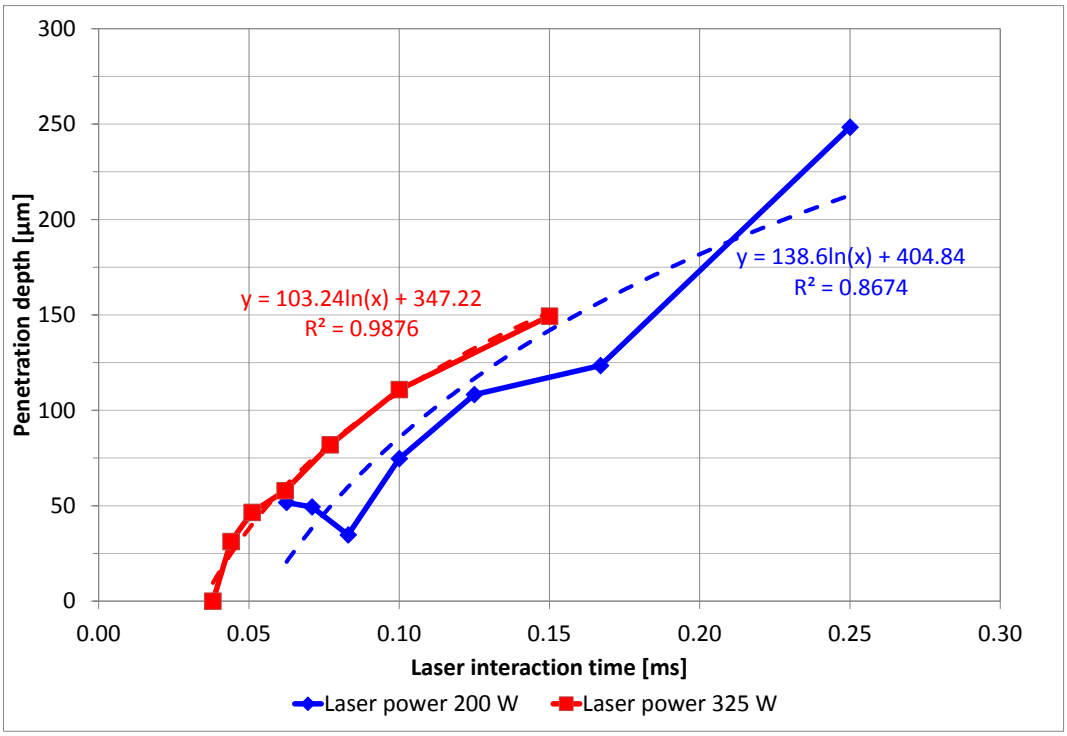

Figure 36. Laser interaction time vs. penetration depth.

As it can be seen from figure 36, the laser interaction time has an effect on the penetration depth of the single tracks. As interaction time increases, penetration depth also increases since laser beam and material interact longer time.

Figure 37 shows laser interaction time vs. penetration depth when laser power of 200 W and 325 W were used.

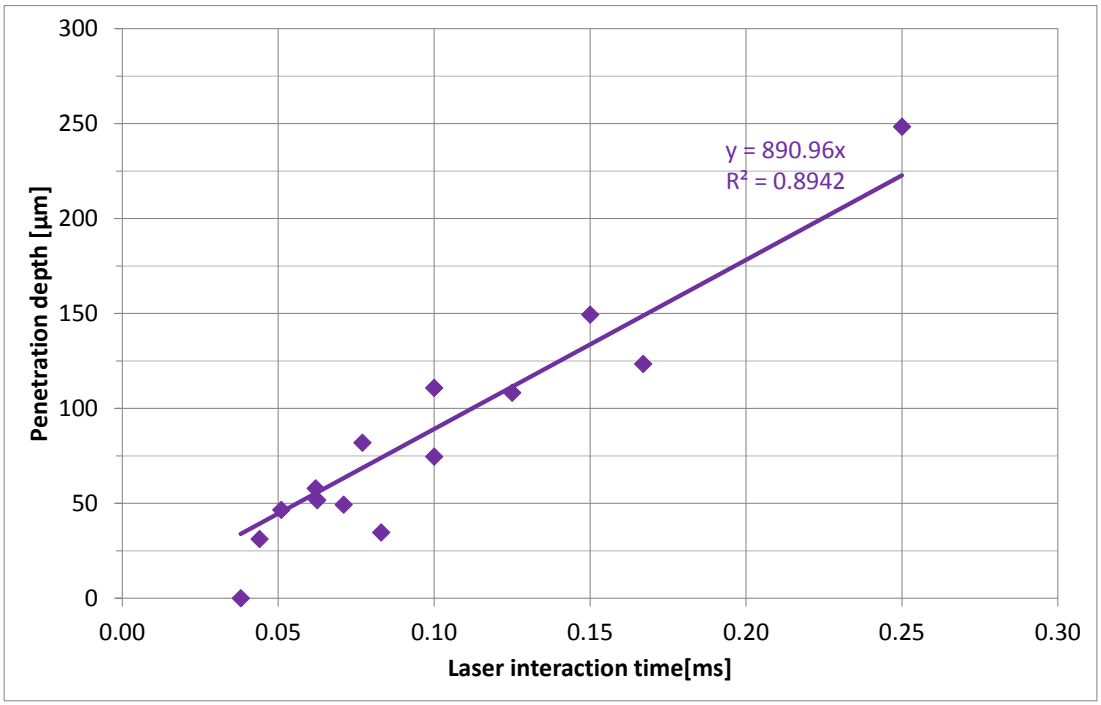

Figure 37. Laser interaction time vs. penetration depth.

Figure 37 shows that the laser interaction time is linearly dependent on penetration depth. It can be observed from the figure 37 that the penetration depth increases when the interaction time increases. It can be also seen from the figure 37, that the penetration depth has only minor variation with short laser beam – material interaction time. With longer interaction times it is possible to achieve multiple times deeper penetration than with short interaction times.

6.1.3 Energy density vs. bead width

Similarly as the penetration depth, the single track bead width is compared to each other. Figure 38 presents energy density vs. bead width when laser power of 200 W and 325 W were used.

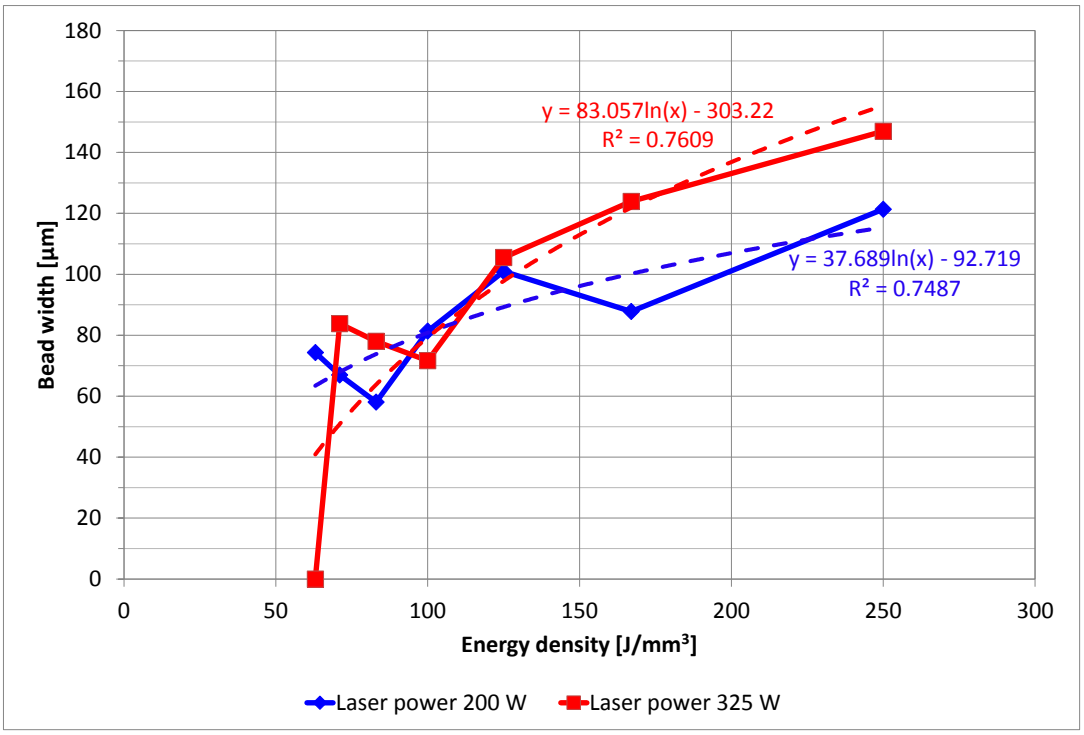

Figure 38. Energy density vs. bead width.

Figure 38 shows that the bead width has larger variation than the penetration depth (Fig. 36). However, there is dependency between energy density input and bead width, as it can be seen from the figure 38. The test piece of 325 W single tracks was wider than the test piece of 200 W, when the test piece of 200 W had deeper penetrated single tracks. This might be because the test piece of 325 W single tracks was made with higher scanning speeds, such that the laser interaction time was shorter. This issue needs further study. It is noticeable that the bead width almost doubles when comparing the highest energy density input into the lowest energy density input.

6.1.4 Laser interaction time vs. bead width

Figure 39 shows laser interaction time vs. bead width when laser power of 200 W and 325 W were used.

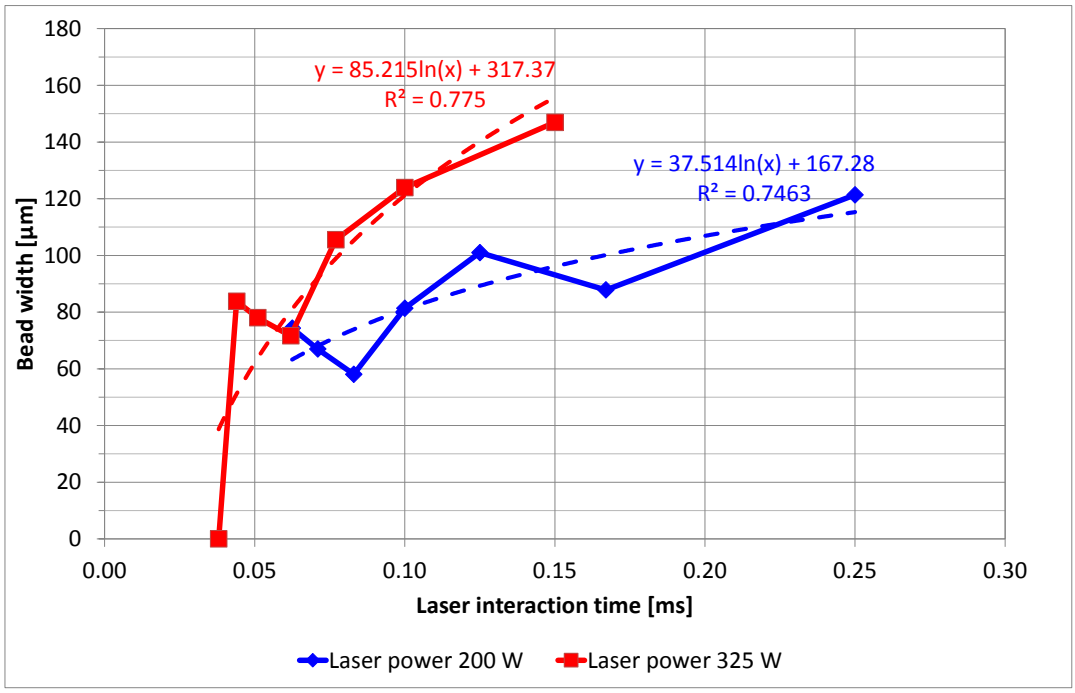

Figure 39. Laser interaction time vs. bead width.

Figure 39 shows that the bead width in test of single track is dependent on the laser interaction time. As it can be seen from the figure 39, the bead width is wider when the interaction time is shorter and vice versa. It can be seen that the scanning speed has effect on the bead width. It seems that when laser interaction time increases over 0.1 ms, the bead width growth stabilizes.

6.1.5 Effect of heat treatment on energy density vs. penetration depth

Test pieces of 325 W with and without heat treatment were compared to each other. Otherwise the parameters are same between these specimens. Figure 40 illustrates effect of heat treatment to energy density vs. penetration depth.

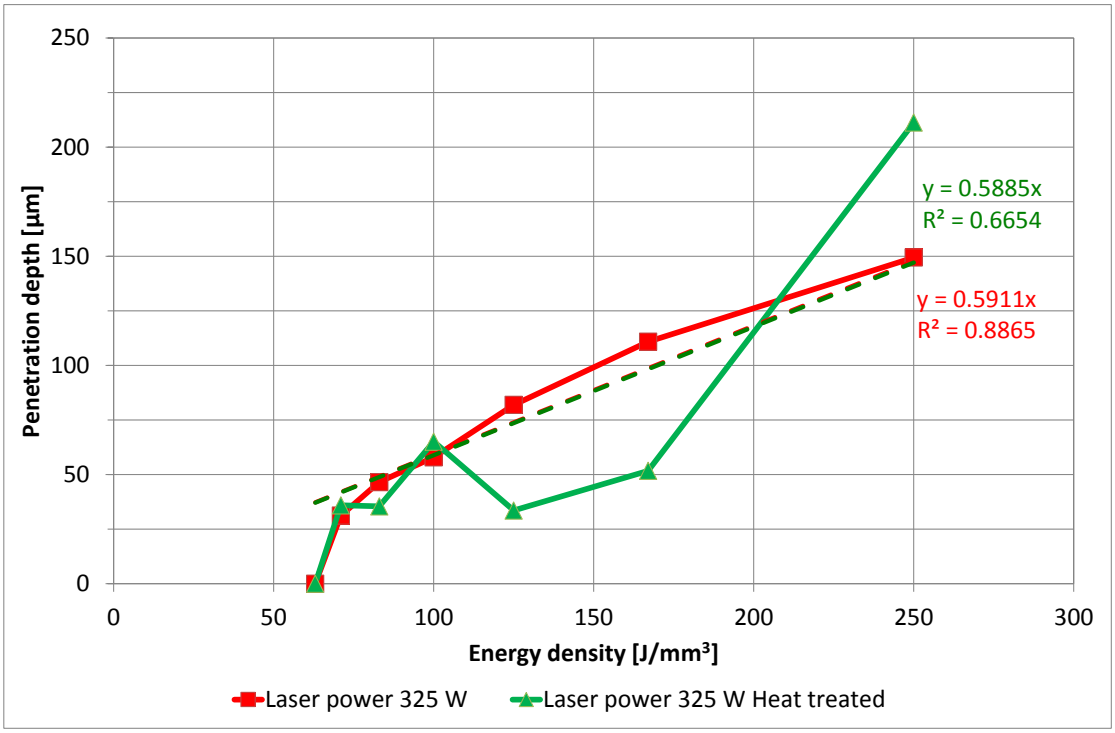

Figure 40. Effect of heat treatment to energy density vs. penetration depth.

Figure 40 shows that heat treatment affects penetration depth so that it varies more than when no heat treatment was used. A single bead was close to the edge of the base material and it was impossible to see it with microscope in heat treated single track made with lowest energy density input. Figure 40 shows that the penetration depth has very little variation between non-heat treated and heat treated sample, when the energy density input is the nominal value of 100 J/mm^3 or less. When the energy density increases, the penetration decreases in heat treated sample, while the penetration depth increases linearly in non-heat treated sample. But when energy density input is more than 167 J/mm^3 the penetration depth increases dramatically in heat treated sample. When compared to non-heat treated sample, the heat treated sample has deeper penetration when energy density input is 250 J/mm^3.

6.1.6 Effect of heat treatment on laser interaction time vs. penetration depth

Figure 41 shows effect of heat treatment to laser interaction time vs. penetration depth.

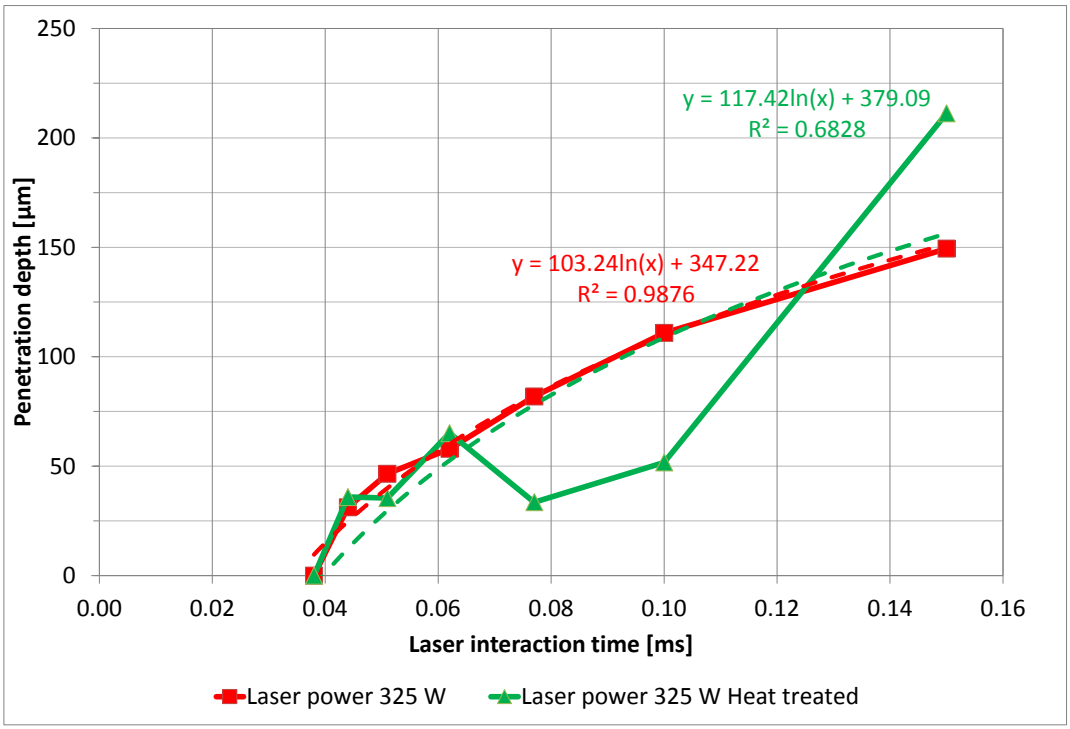

Figure 41. Effect of heat treatment to laser interaction time vs. penetration depth.

As interaction times are the same, it can be seen from the figure 41 that the first four tracks penetration depths are very close to each other, when comparing heat treated and non-heat treated specimen. When laser interaction time is longer, the penetration depth varies between heat treated and non-heat treated samples. As it can be seen from figures 40 and 41, the heat treated sample has deeper penetration depth with highest energy density input than non-heat treated one.

6.1.7 Effect of heat treatment on energy density vs. bead width

The bead width measurements were also compared between heat treated and non-heat treated specimen. Figure 42 illustrates effect of heat treatment to energy density vs. bead width.

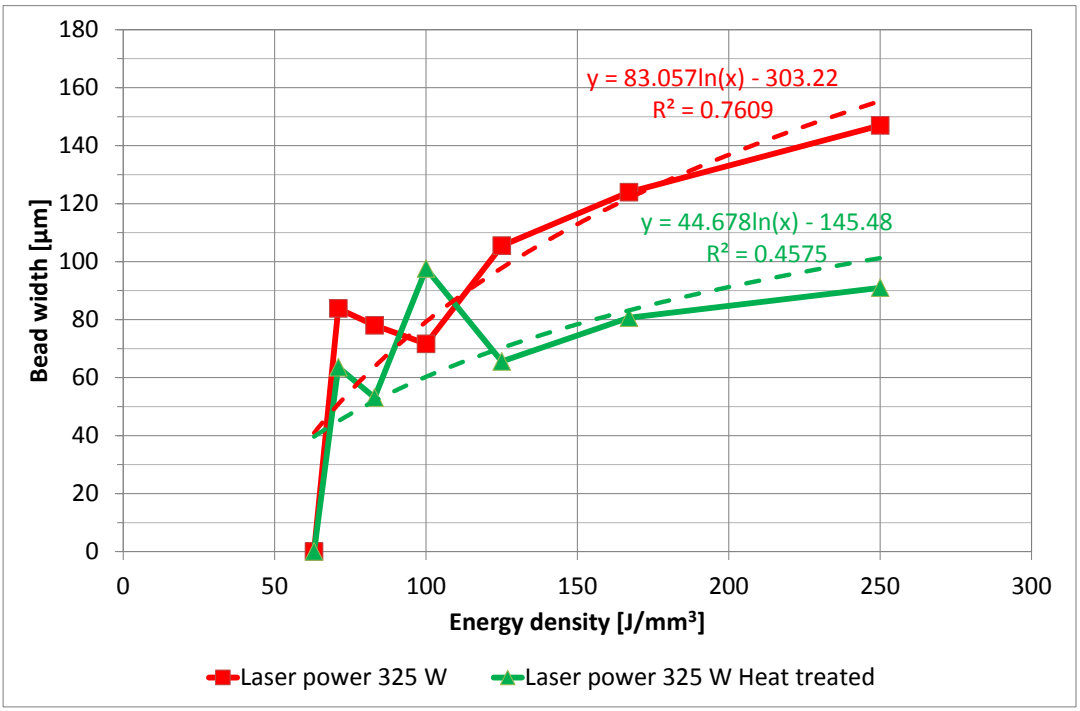

Figure 42. Effect of heat treatment to energy density vs. bead width.

As it can be seen from figure 42, the bead width in both test pieces varies with energy density input values less than the nominal 100 J/mm^3. It is also interesting to see, that the heat treated sample has the widest bead with energy density input of 100 J/mm^3, when non-heat treated specimen has narrowest bead width with the same energy density input. When energy density input is higher than 100 J/mm^3, the bead width is increasing linearly, when the energy density input is increasing. It can be also seen from the figure 42, that non-heat treated sample has overall wider bead width with almost all energy density inputs.

6.1.8 Effect of heat treatment on laser interaction time vs. bead width

Figure 43 shows the effect of heat treatment to laser interaction time vs. bead width.

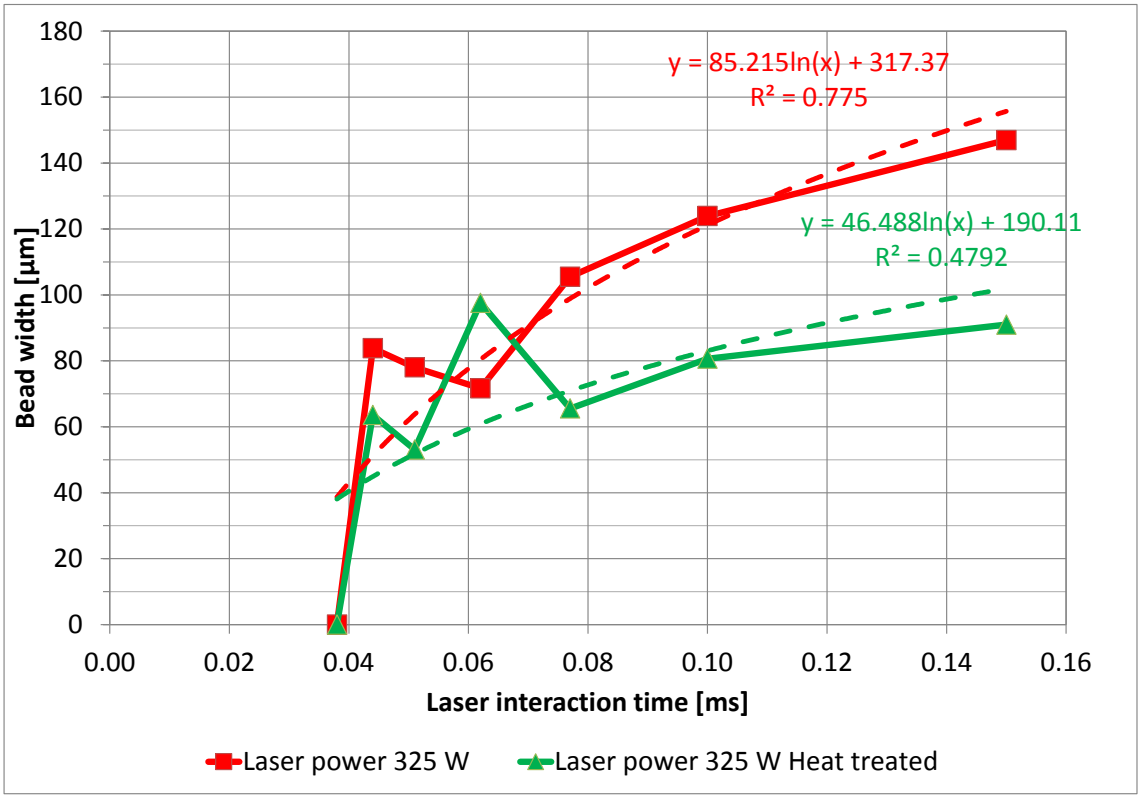

Figure 43. Effect of heat treatment to laser interaction time vs. bead width.

As it can be seen from figure 43, the bead widths are varying a lot, when laser interaction time is at the shortest. It can be also observed from the figure 43, that when interaction time is more than 0.08 ms, the bead width increases almost linearly. Since these two specimen single tracks have same laser interaction times it is noticeable that non-heat treated specimen has wider bead width than the heat treated one.

6.1.9 Energy density vs. *WDR*

Figure 44 presents energy density vs. *WDR*, when laser power of 200 W and 325 W were used.

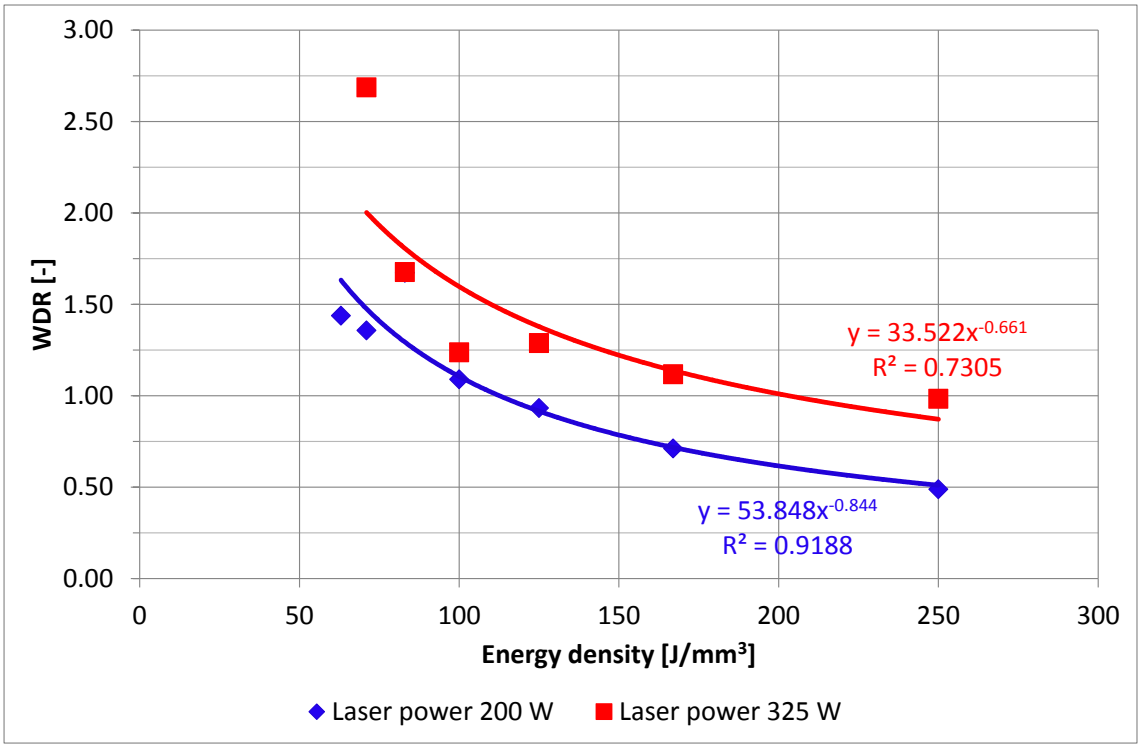

Figure 44. Energy density vs. *WDR*.

It can be observed from figure 44, that *WDR* decreases when energy density input increases. As mentioned before, the single track made with lowest energy density input in 325 W sample was not possible to detect, so that track was not plotted in figure 44. It can be seen, that *WDR* values, when laser power of 200 W was used, decreases as energy density input increases. It is also noticeable that *WDR* values, when laser power of 325 W was used, are larger than *WDR* values with laser power of 200 W. This can be because the 200 W single-tracks were made with slower scan speeds thus probably causing deeper penetration rather than wider bead width. However, this issue needs further study. Single tracks manufactured with 200 W had overall deeper penetration than single tracks fabricated with laser power of 325 W.

Figure 45 illustrates effect of heat treatment on energy density input vs. *WDR*.

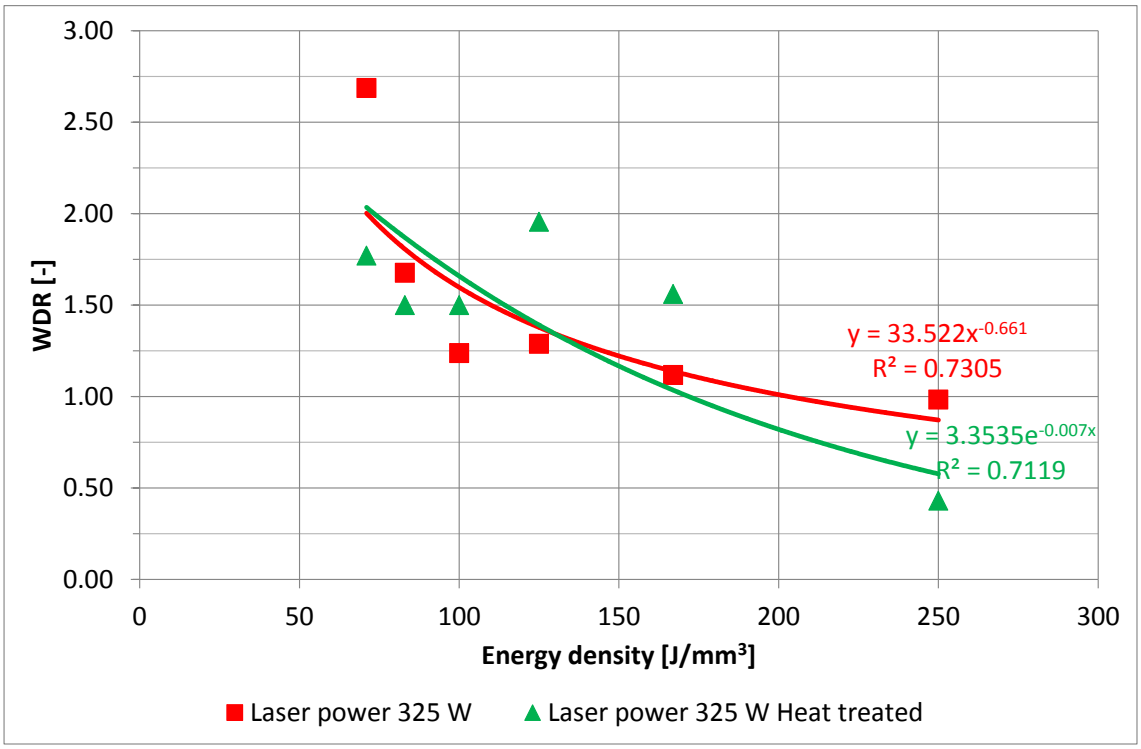

Figure 45. Effect of heat treatment on energy density vs. *WDR*.

As it can be concluded from figure 45, the *WDR* of heat treated sample vary when energy density input is between 63 J/mm^3 and 167 J/mm^3. The *WDR* values of non-heat treated sample decreases when energy density increases. It is also noticeable that almost all *WDR* values of heat treated sample are larger than those of the non-heat treated, when energy density is between 63 J/mm^3 and 167 J/mm^3. When energy density is larger than 167 J/mm^3, the *WDR* value of heat treated sample is smaller than in the non-heat treated.

Figure 46 presents energy density vs. *WDR* when laser power of 200 W and 325 W were used.

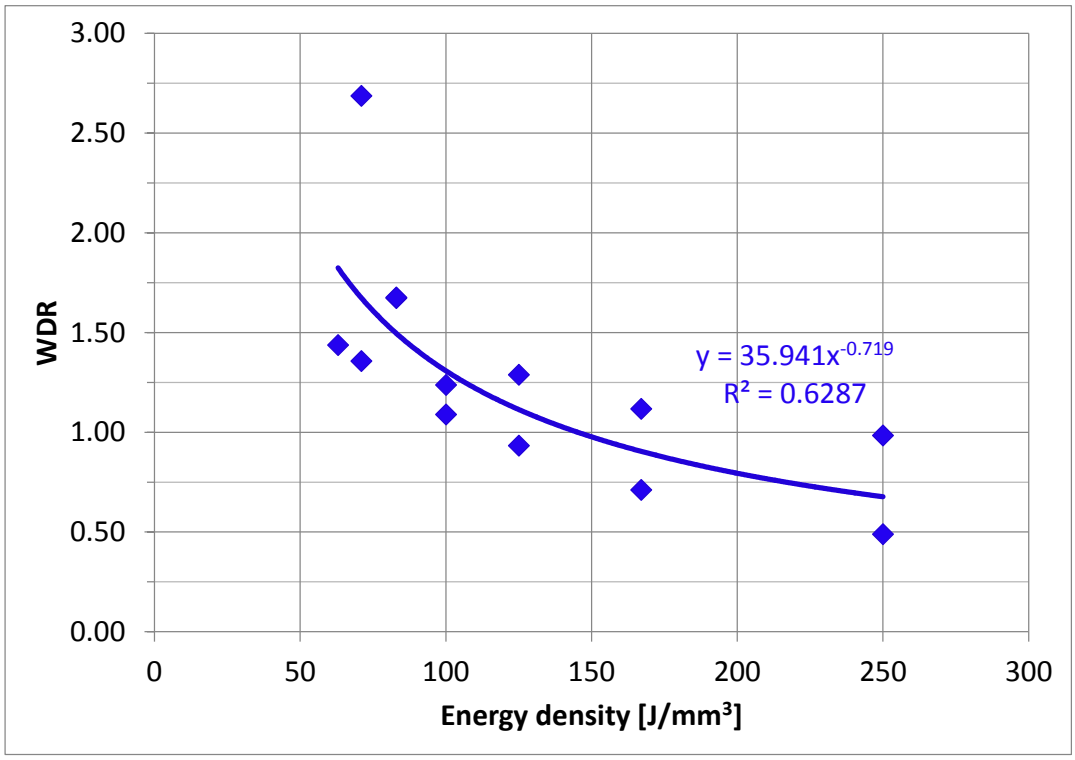

Figure 46. Energy density vs. *WDR*.

As it can be observed from the figure 46, there is variation in *WDR*. It can be seen from figure 46 that *WDR* acts such that when energy density increases, the *WDR* decreases. This means that the single tracks start to achieve deeper and narrower penetration when the energy density input increases.

6.1.10 Laser interaction time vs. *WDR*

Figure 47 illustrates laser interaction time vs. *WDR* when laser power of 200 W and 325 W were used.

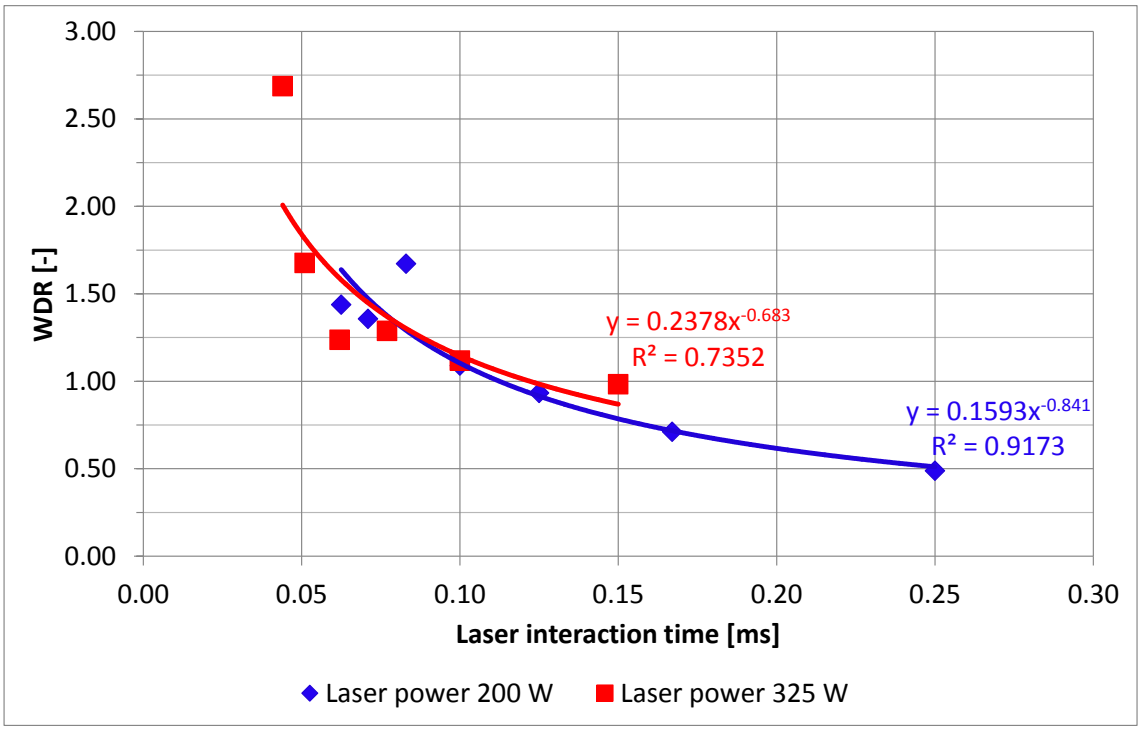

Figure 47. Laser interaction time vs. *WDR*.

Single track manufactured with laser power of 325 W and with shortest laser interaction time is not shown in figure 47, since it was impossible to see it with microscope. As it can be noticed from figure 47, the *WDR* with both samples are between 1.15 and 2, when the laser interaction time is between 0.05 ms to 0.1 ms. Also, the *WDR* decreases under value of one when interaction time is more than 0.1 ms. It can be observed from the figure 47, that if laser interaction time is increasing, the *WDR* decreases.

Figure 48 represents effect of heat treatment on laser interaction time vs. *WDR*.

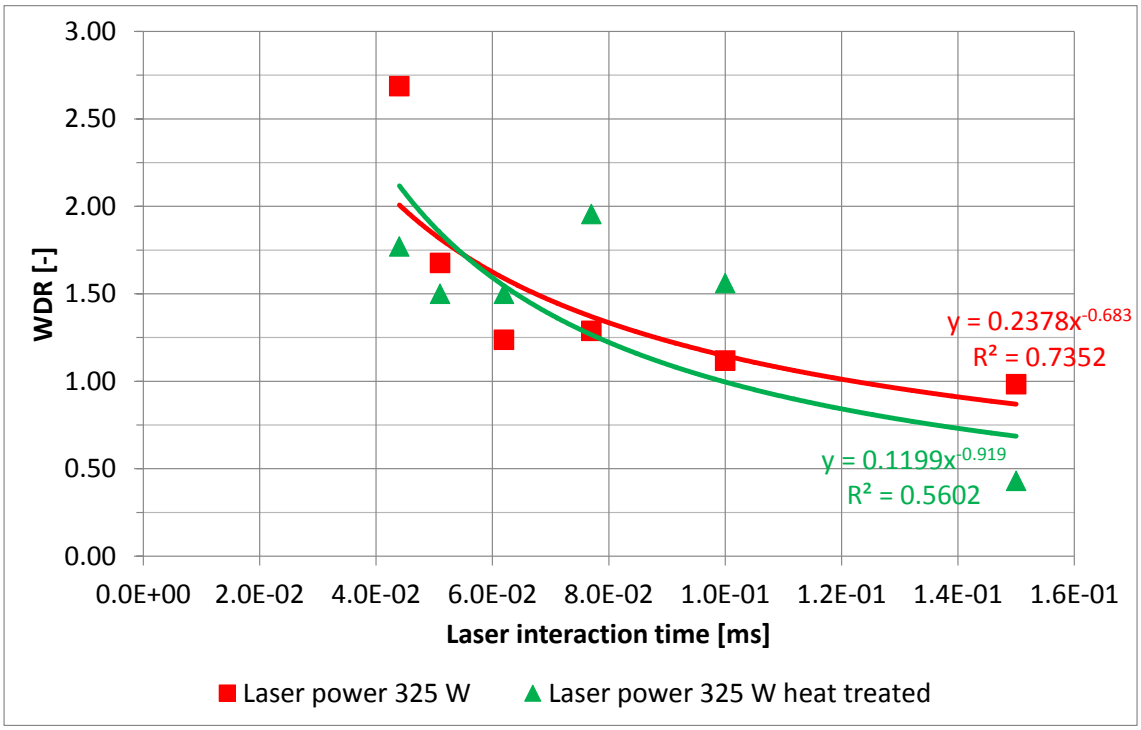

Figure 48. Effect of heat treatment on laser interaction time vs. *WDR*.

As it can be concluded from figure 48, the *WDR* value vary more in heat treated sample than in non-heat treated one. In case of non-heat treated sample, the *WDR* value first decreases quickly and when laser interaction time is increasing the *WDR* is balancing. *WDR* values in heat treated sample first decrease when interaction time increases, but while interaction time increases more the *WDR* also increases. This is because the bead width is increasing. As it can be seen from figure 48, once the laser interaction time is longer than 0.1 ms, the *WDR* value in heat treated sample is decreasing because of larger penetration depth.

Figure 49 presents laser interaction time vs. *WDR*.

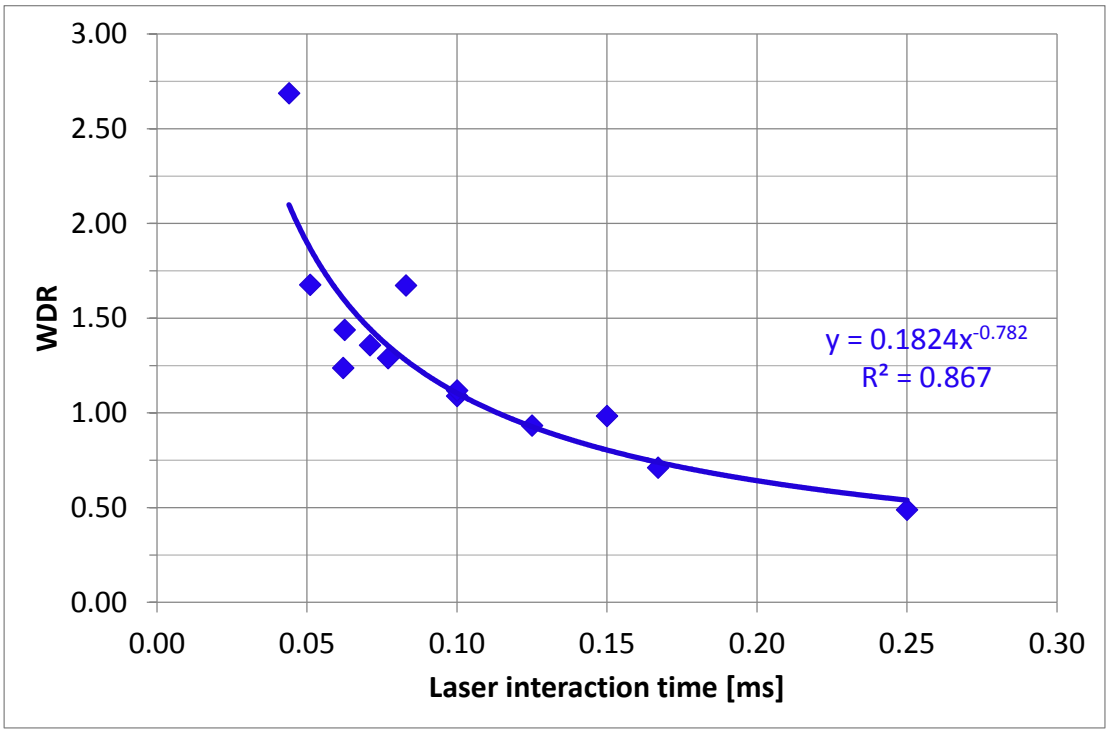

Figure 49. Laser interaction time vs. *WDR*.

Figure 49 shows that when *WDR* is presented as function of laser interaction time, the variation in *WDR* settles. It can be seen from the figure 49 that laser interaction time has effect on *WDR*. When the laser interaction time is increased, the *WDR* decreases dramatically. This is again because of the deep and narrow penetration of the single tracks. So it can be said that with higher energy density input and with longer laser interaction time, the single tracks tend to have narrow and deep penetration.

6.1.11 Energy density vs. *WDA*

The area of the penetrated tracks were also roughly calculated and compared between specimens made with laser power of 200 W, 325 W and the one which was heat treated. The energy density vs. *WDA*, when laser power of 200 W and 325 W were used, is presented in figure 50.

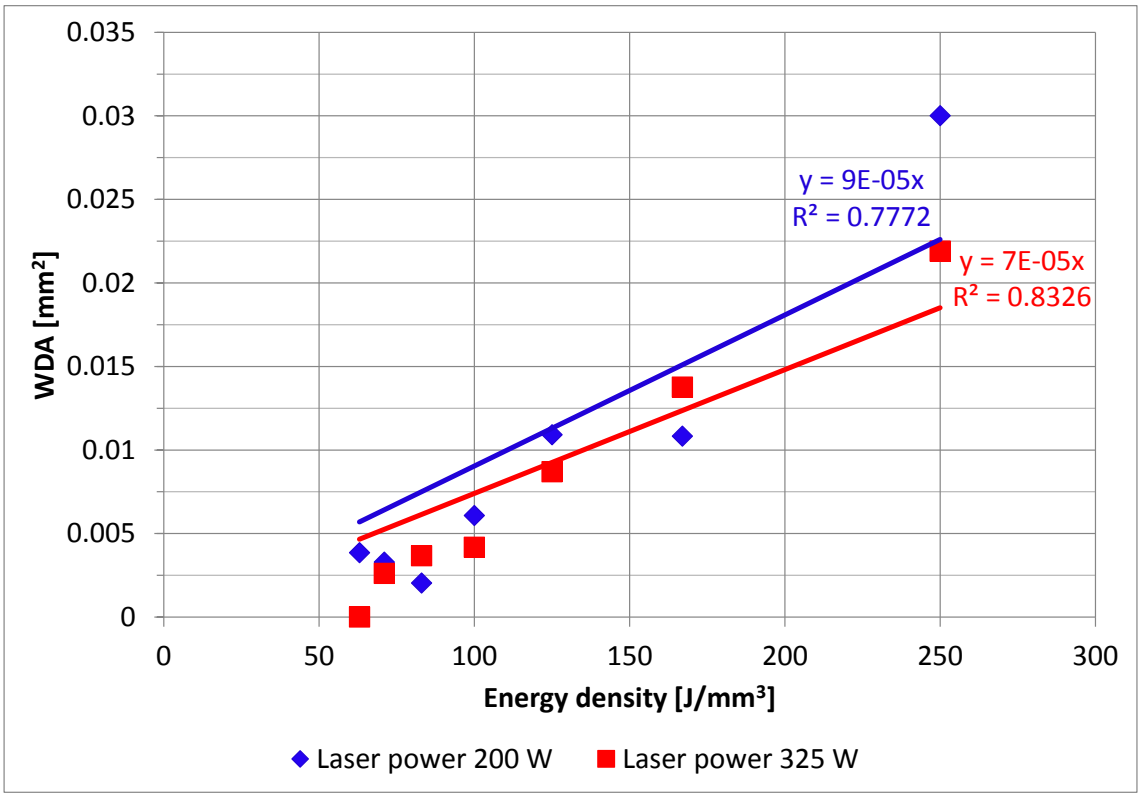

Figure 50. Energy density vs. *WDA*.

As it can be observed from the figure 50, *WDA* is very close to each other with both of the test pieces when energy density input is less than 100 J/mm^3. *WDA* of 200W increases when energy density input increases. This is because of the large penetration depth of the single-tracks in this test piece. Figure 50 shows also similar behavior when laser power of 325 W was used.

Figure 51 presents effect of heat treatment on energy density vs. *WDA*.

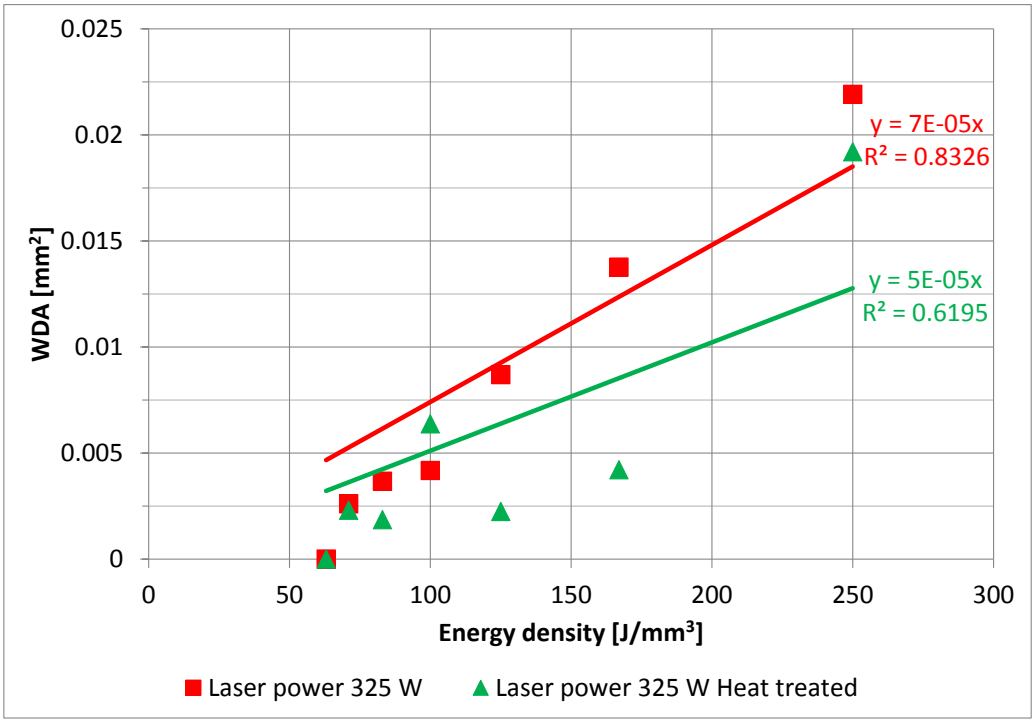

Figure 51. Effect of heat treatment on energy density vs. *WDA*.

As it can be observed from figure 51, the heat treated test piece *WDA* is not increasing as strongly as with non-heat treated sample with laser power of 325 W, when energy density input is increasing. As it can be seen from the figure 51, *WDA* values in heat treated sample are small until energy density input increases over 167 J/mm^3. After this point, *WDA* increases in heat treated sample. This is because of the deeper penetration. Overall the non-heat treated *WDA* values are larger than the heat treated ones.

Figure 52 presents the energy density vs. *WDA*.

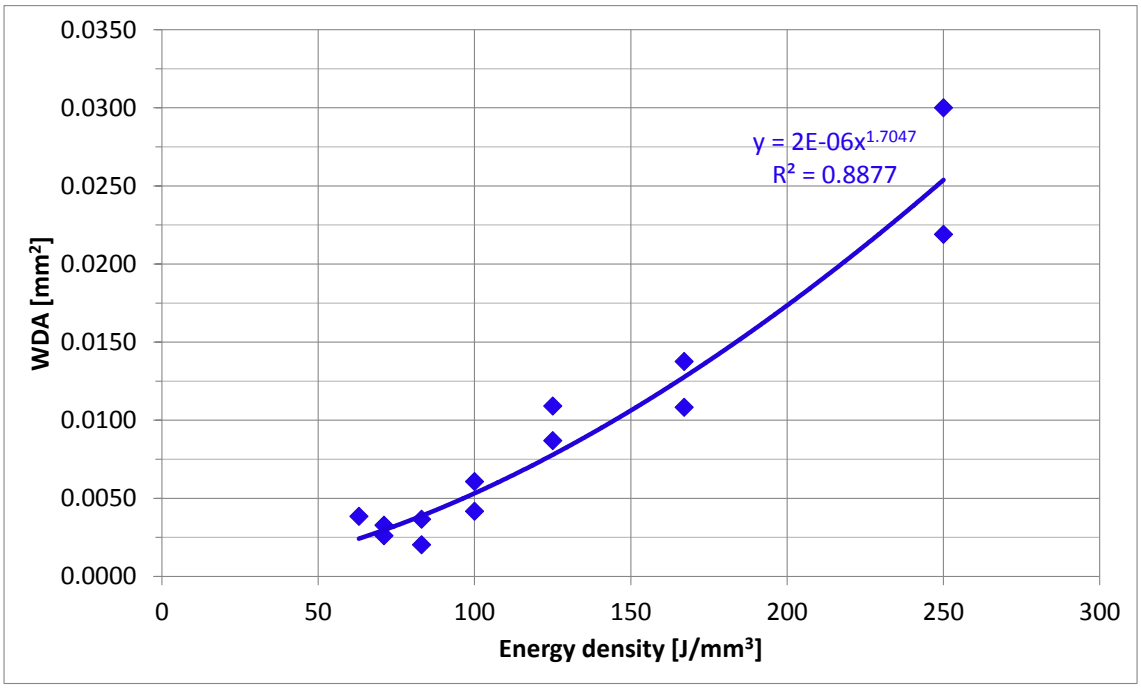

Figure 52. Energy density vs. *WDA*.

Figure 52 shows that when energy density is increased, the *WDA* is also increasing. It can be seen also from the figure 52, that the *WDA* remains quite stable until energy density input is higher than the nominal value of 100 J/mm^3. As mentioned before, the energy density input value of 100 J/mm^3 seems to be some kind of threshold value, since when energy density input rises above that, the penetration depth increases dramatically.

6.1.12 Laser interaction time vs. *WDA*

Figure 53 represents laser interaction time vs. *WDA* when laser power of 200 W and 325 W were used.

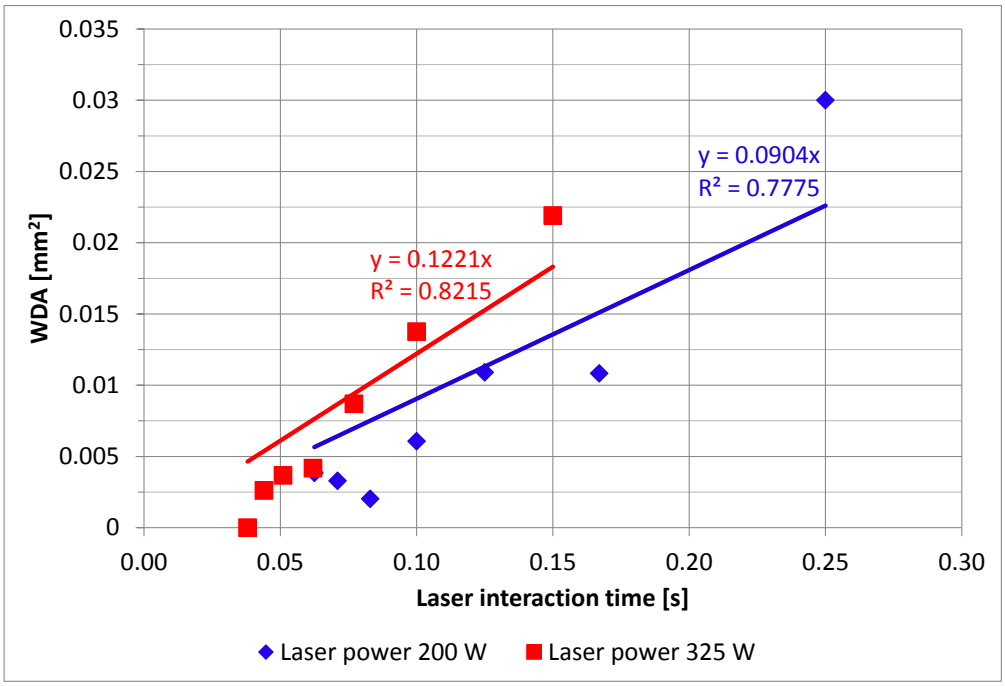

Figure 53. Laser interaction time vs. *WDA*.

As it can be observed from figure 53, *WDA* increases, when laser interaction time increases. It can be also seen, that when laser interaction time is between 0.05 to 0.1 ms, *WDA* is very close to each other between both test pieces. It is also interesting to see, that *WDA* values with laser power of 325 W increases more rapidly than with the 200 W specimen, even though the 200 W sample has longer interaction times. With laser power of 200W, the area of penetration does not increase rapidly until when the laser interaction time is more than 0.2 ms. This is again because the 200 W specimen has deeper and narrower penetrations in single-tracks, compared to the one made with 325 W.

Figure 54 shows effect of heat treatment on laser interaction time vs. *WDA*.

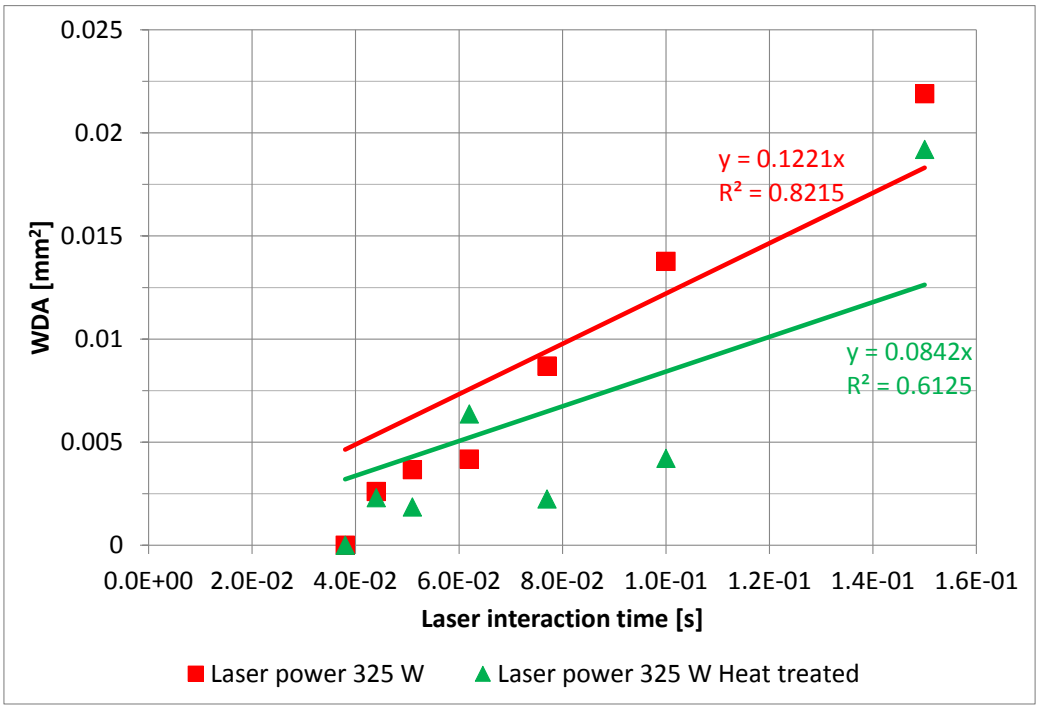

Figure 54. Effect of heat treatment on laser interaction time vs. *WDA*.

Figure 54 shows that *WDA* of heat treated sample are low compared to the non-heat treated one. This is because the heat treated beads are narrow and low penetrated compared to the non-heat treated ones. It can be also concluded that the non-heat treated *WDA* values are increasing linearly when the laser interaction time is increasing. This is because of the larger penetration depths when interaction time is increased. When laser interaction time is more than 0.1 ms, the *WDA* values of both pieces increases dramatically. This is because of large penetration depth and wider bead width.

Figure 55 illustrates laser interaction time vs. *WDA*.

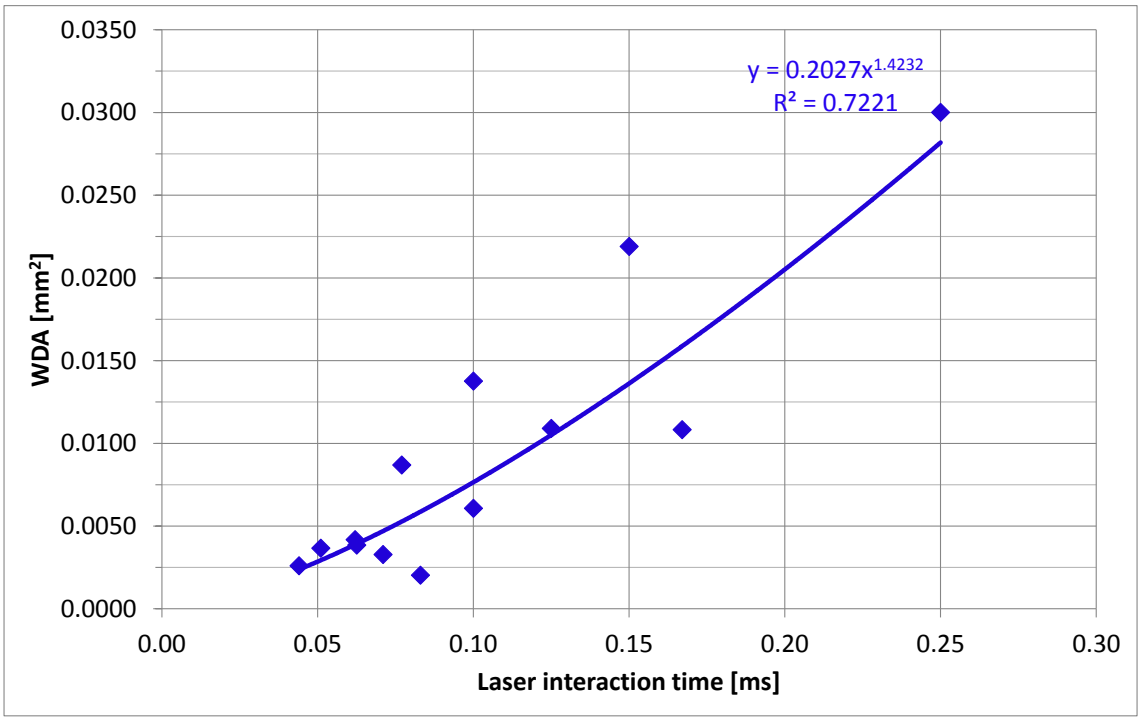

Figure 55. Laser interaction time vs. *WDA*.

It can be observed from the figure 55, that laser interaction time has effect on the single-track *WDA*. It can be seen that *WDA* increases when laser interaction time increases. As mentioned before, this is because the penetration is deeper with longer laser beam interaction time. It can be also seen from the figure 55, that with the laser interaction time between 0.05 to 0.1 ms, the single-track *WDA* are very close to each other. When the interaction time is longer than 0.1 ms, the *WDA* start to increase.

6.2 Penetration depth in beginning of single track and in middle of single track

There were two polished sections made from the specimen made with laser power of 200 W, one which was made from the edge of the specimen and one, which was made from the lengthwise cut from the middle of the specimen. Figure 56 shows the comparison of penetration depth between the beginning of the single track and middle of single track.

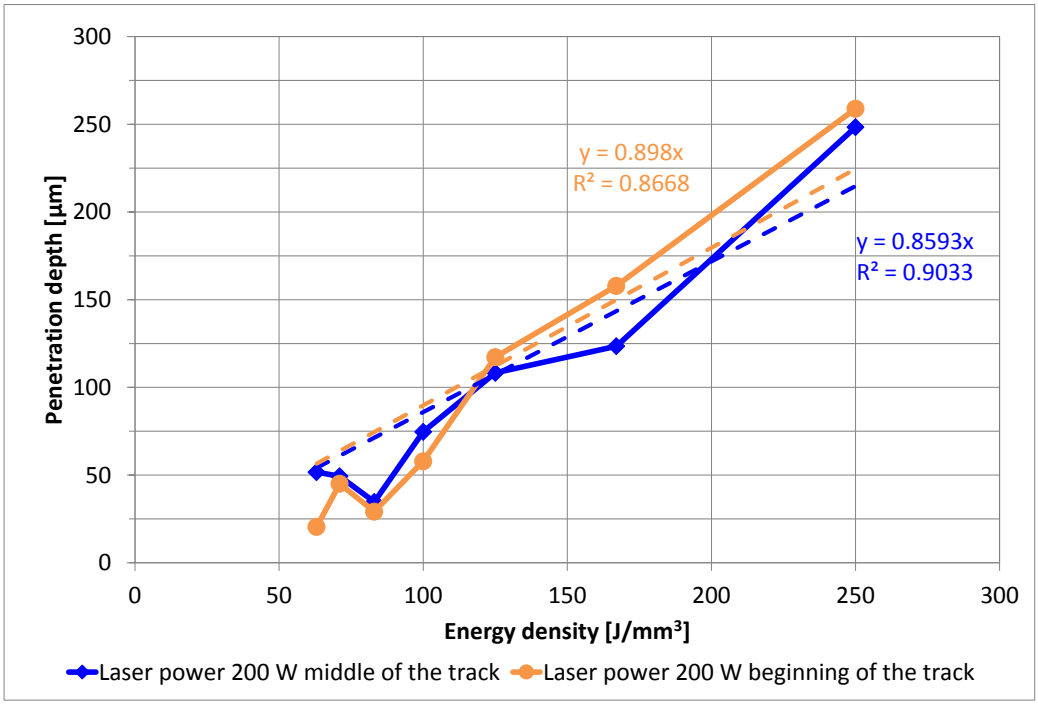

Figure 56. Energy density vs. penetration depth when measurement is done in beginning of single track and in middle of the single track.

As it can be observed from the figure 56, the penetration depth has only minor variations between the beginning of the track and middle of the track. The penetration depth from the beginning of the single track, is lower than in the middle of the track, when energy density input is lower than the nominal value of 100 J/mm^3. But once the energy density input is higher than 125 J/mm^3, the penetration depth increases in the beginning of the tracks. As mentioned before, the penetration depths seem to maintain the same depth along the exposed single track and the variation is very small between the penetration in the beginning of the track and in the middle of the track.

6.3 Bead height

Bead height was also measured from all of the test pieces. In bead height measurements the height variation was so large that no conclusion could be drawn. All the measurement data can be found from appendix III.

6.4 Single tracks with keyhole

It was noticed in single track tests that some of the tracks have very deep and narrow penetrations into the bulk material. It was decided to analyze these deep penetrated tracks

and figure out whether there have been keyhole or not, when single track have been exposed. Figure 57 illustrates fusion zone profiles of different welding processes (Steen, Mazumder, 2010, p.199).

Process	Heat source intensity ($W\,m^{-2}$)	Fusion zone profile
Flux-shielded arc welding	5×10^6–10^8	
Gas-shielded arc welding	5×10^6–10^8	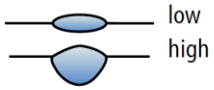
Plasma	5×10^6–10^{10}	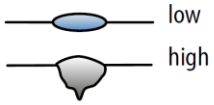
Laser or electron beam	10^{10}–10^{12}	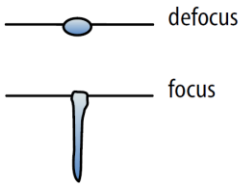

Figure 57. Fusion zone profile with different welding processes. (Steen and Mazumder, 2010, p.199).

Steen and Mazumder, (Steen and Mazumder, 2010) describe keyhole weld in laser welding, as weld that have parallel sided fusion zone, narrow width and deep penetration. Also the intensity of the laser beam should be 10^6 W/cm^2 or more in order to achieve formation of keyhole. The intensity calculations (see Appendix II) show that the threshold value 10^6 W/cm^2 for keyhole formation is exceeded in all of the single tracks. However, it was decided to investigate single tracks with deep and narrow penetration and *WDR* less than one.

Figure 58 presents micrographs of single tracks St_1, St_2 and St_3 made with laser power of 200 W.

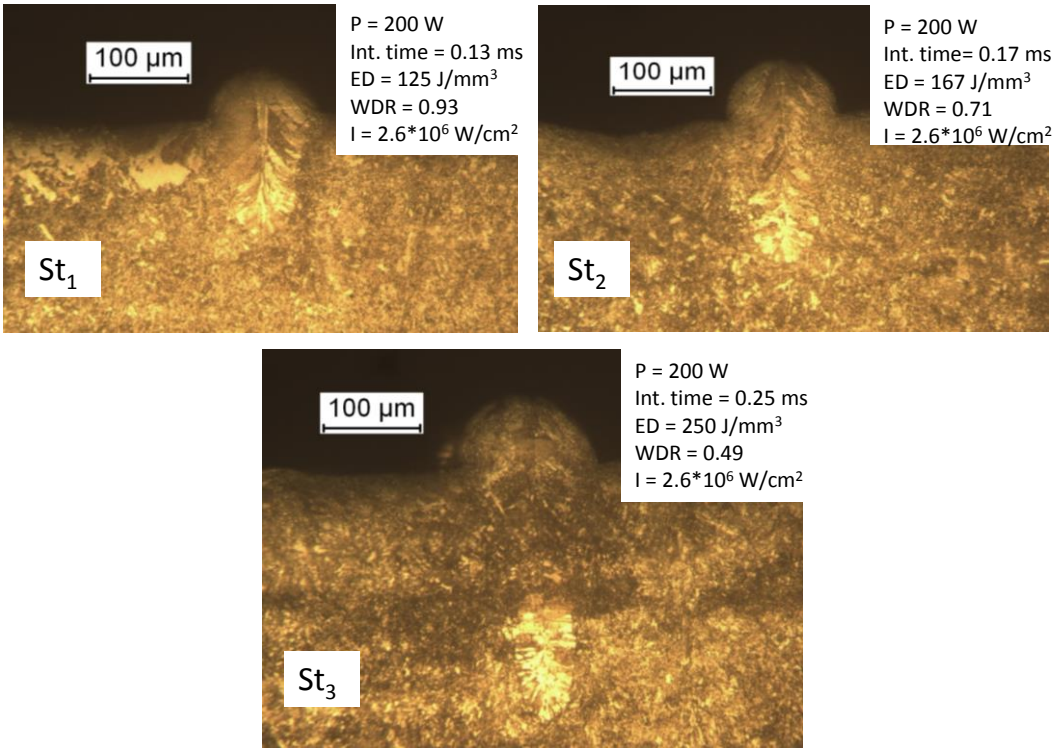

Figure 58. Single tracks *St₁*, *St₂* and *St₃* made with laser power of 200 W.

The figure 58 shows that, the limit intensity value for keyhole formation is exceeded in all of the single tracks, and it can be seen from figure 58 that the solidification of the penetrated tracks are similar than in laser welds including keyhole. As it can be observed from the figure 58, the penetration of the single track *St₁* is rather deep and as the *WDR* presents, the penetration of this track is deeper than the width of the track. It can be concluded from the figure 58, that when this single track was exposed it might have formed with keyhole. This issue needs further study.

As it can be seen from the figure 58, the penetration depth increases when scanning speed is decreasing and energy density is increasing. The single track *St₂* have narrow and deep penetration, as the *WDR* value shows. While the interaction time increases, also the penetration depth increases. It seems, that laser interaction time has effect of whether keyhole is formed or not, but it needs further studies.

As it can be analyzed from figure 58, the penetration depth of the single track *St₃* is large, and the bead is narrow as *WDR* value shows. The energy density input in this track is large which seems to lead deep and narrow penetration. It can be seen that the interaction time in *St₃* is longer than in tracks *St₁*, *St₂* and the penetration is larger because of that.

Figure 59 represents non-heat treated single track St_3 and heat treated single track St_3 made with laser power of 325 W.

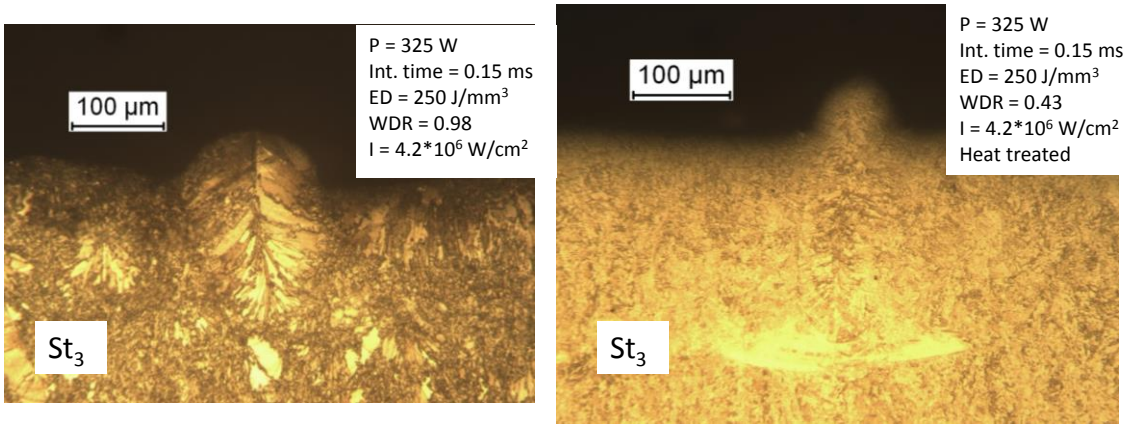

Figure 59. Non-heat treated single track St_3 and heat treated single track St_3 made with laser power of 325 W.

As it can be seen from figure 59, non-heat treated single track St_3 has not as deep or narrow penetration as single track St_3 made on heat treated bulk material. It can be observed from figure 59, that *WDR* value of non-heat treated St_3 is close to one which means that the width is close to the depth of penetration. Interesting is also to see, that when the energy density input is same as in heat treated St_3 and in figure 58 St_3, the penetration depth of non-heat treated St_3 is much lower. From the comparison of figure 58 and 59, it can be concluded that interaction time defines if keyhole is formed or not, since the intensity value is larger in all tracks than the threshold value for keyhole formation. Form of the non-heat treated St_3 in figure 59 is close to St_1 in figure 58, even though the energy density input is higher in non-heat treated St_3 in figure 59. The similarity is because the interaction times are very close to each other, and it seems that when interaction time exceeds 0.15 ms, the penetration becomes deeper and narrower. However this needs further studies.

As it can be seen from figure 59, the penetration is very deep in heat treated single track St_3. Also the *WDR* is small, which indicates narrow width and deep penetration. Compared to the St_3 in figure 58, these two single tracks share the similarity in the penetration form. Both are deep and narrow with same energy density input. When comparing heat treated St_3 to the non-heat treated St_3, it can be seen that heat treated St_3 has deeper and narrower penetration, even though these two are made with same energy

density input and they also share same interaction time. It seems that the heat treatment has also some effect on the penetration depth when interaction time is 0.15 ms or more.

6.5 Input-output parameter relations

When understanding the relations of input and output parameters (see figure 20) such as energy density input, laser interaction time, penetration depth and *WDA*, it is possible to evaluate and analyze the process efficiency. As literature review presented, process build rate can be evaluated as equation 1 shows. However, in order to adjust the process to be more efficient, the effect of input parameters into output parameters should be understood. It was decided in this thesis, that these input-output relations could be roughly estimated from the basis of the experimental results.

This thesis concludes that there is a significant correlation between:

- Energy density vs. penetration depth (see figure 60),
- Laser interaction time vs. penetration depth (see figure 61),
- Energy density vs. WDA (see figure 62) and
- Laser interaction time vs. WDA (see figure 63).

Energy density input was decided to be included in these equations since it includes important process input parameters, such as laser power, scan speed, layer thickness and hatch distance. The *WDA* value was decided to be included because of the similar reasons. It includes important output parameters, the penetration depth and bead width.

Figure 60 presents energy density vs. penetration depth.

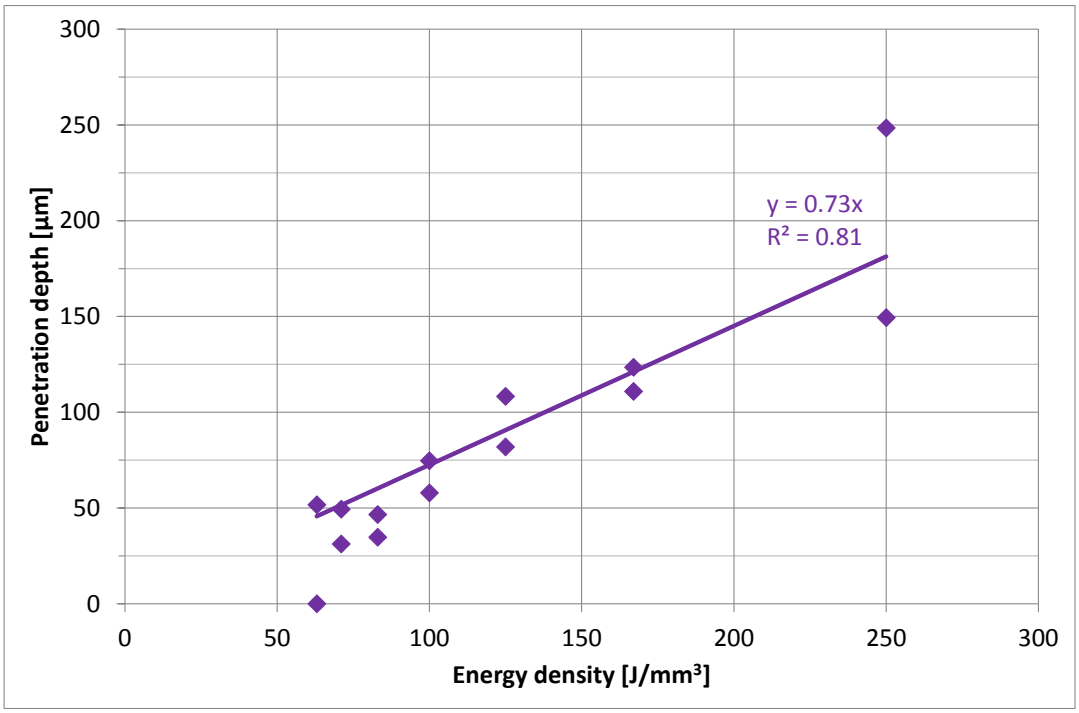

Figure 60. Energy density vs. penetration depth.

As the figure 60 shows, the dependency between energy density input and penetration depth is linear, and R^2 is 0.81. Figure 60 shows that that the penetration depth as function of energy density input can be described with equation 8.

$$PD = 0.73 \cdot ED \tag{8}$$

where, *PD* penetration depth,

ED energy density.

Figure 61 illustrates laser interaction time vs. penetration depth.

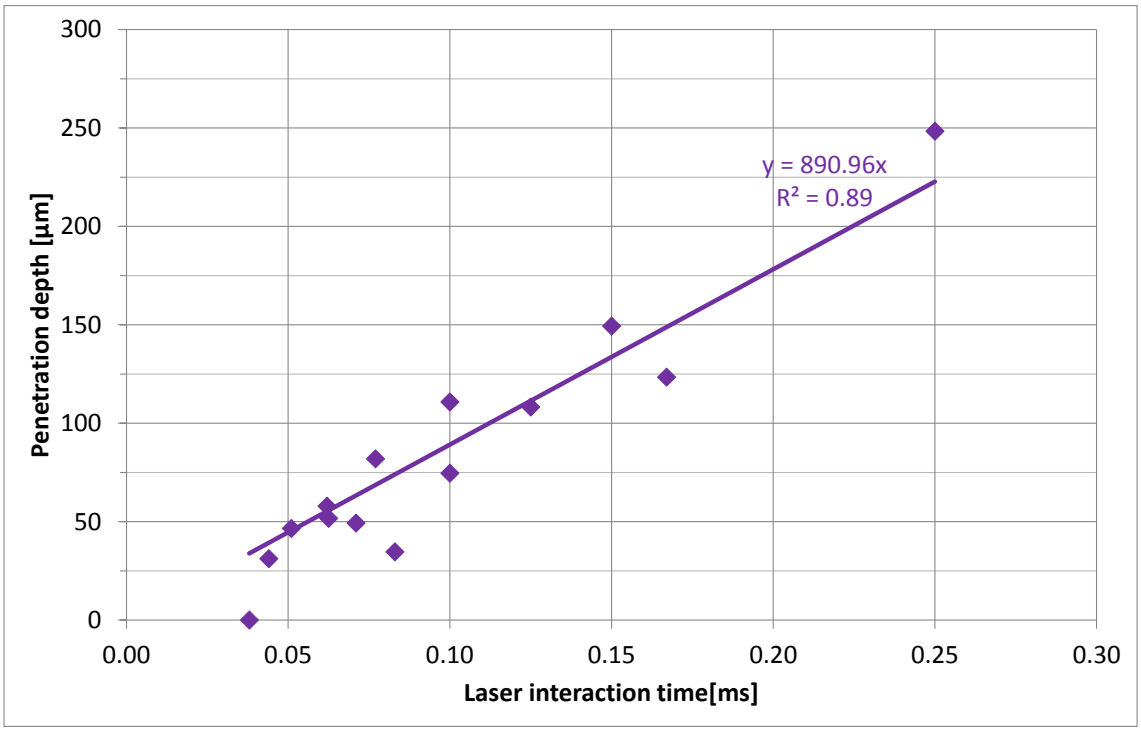

Figure 61. Laser interaction time vs. penetration depth.

As it can be observed from the figure 61, dependency between laser interaction time and penetration depth is linear. R^2 value is 0.89. According to figure 61, equation 9 describes the penetration depth as function of laser interaction time.

$$PD = 890.96 \cdot t \tag{9}$$

where, *PD* penetration depth

t laser interaction time.

Figure 62 represents energy density input vs. *WDA*.

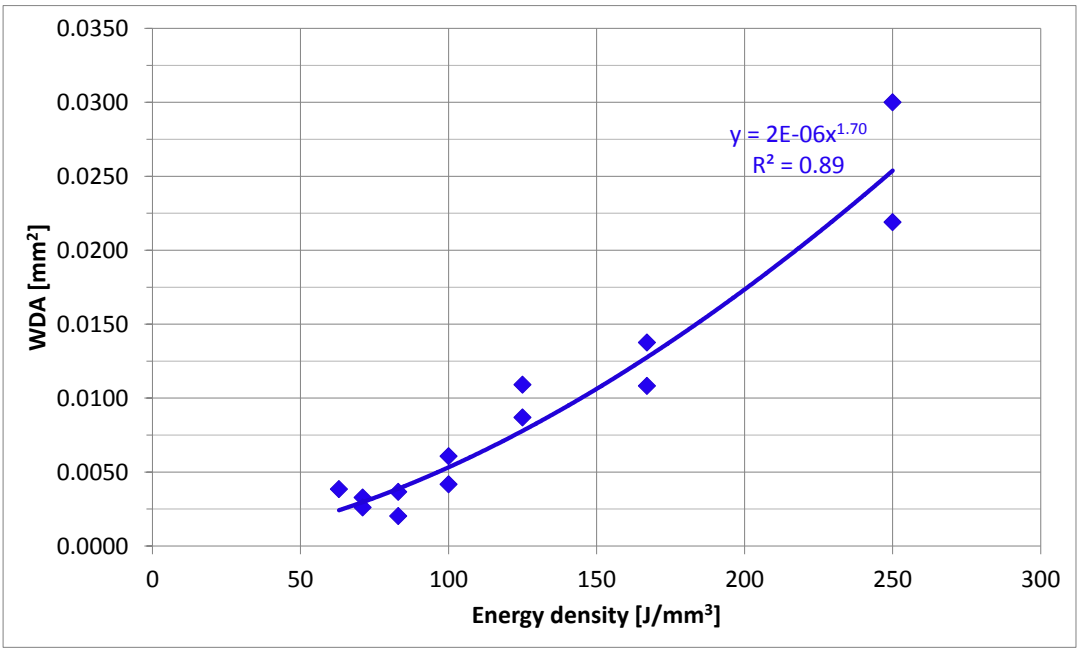

Figure 62. Energy density vs. *WDA*.

As the figure 62 presents, the *WDA* increases while energy density increases. Dependency between energy density and WDA is exponential. It can be also observed that R^2 is 0.89. According to figure 62, *WDA* can be calculated as function of energy density as function 10 represents.

$$WDA = 2 \cdot 10^{-6} \cdot ED^{1.70} \quad (10)$$

where, *WDA* area of penetrated bead,
ED energy density.

Figure 63 presents laser interaction time vs. *WDA*.

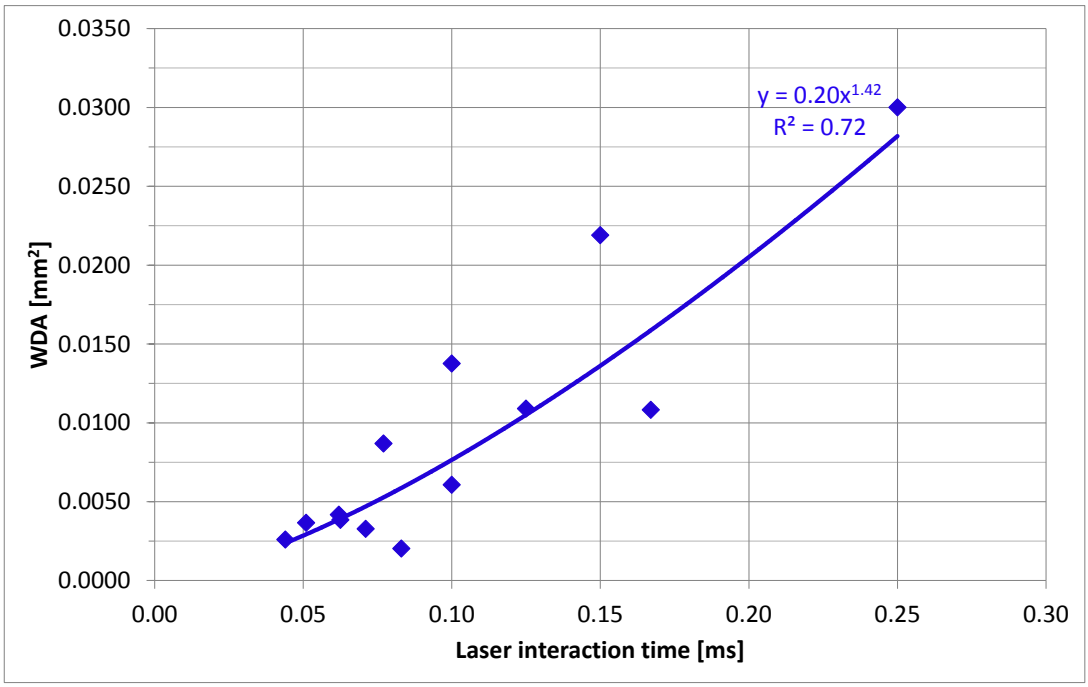

Figure 63. Laser interaction time vs. *WDA*.

It can be seen from figure 63, that increase of laser interaction time increases the *WDA*. It can be also observed that the correlation between laser interaction time and *WDA* is not as good as with energy density vs. *WDA*. It can be seen that there is some dispersion in *WDA* when interaction time is increased. Dependency between laser interaction time and WDA is exponential and R^2 is 0.72. According to figure 63, *WDA* as laser interaction time function can be calculated as equation 11 shows.

$$WDA = 0.20 \cdot t^{1.42} \tag{11}$$

where, *WDA* area of penetrated bead,

t laser interaction time.

As these equations presents, it is possible to estimate the input-output parameter relations from the experimental results. Equation 10 describes the input-output relation very well, since it includes the important input parameters and also the important output parameters. It is possible to evaluate the bead area of the single track with equation 10, and with help of that information, optimizing the process parameters could be one of the further studies. Equation 9 is also important and interesting as it enables to estimate the penetration depth of single track and also the threshold interaction time which leads to keyhole formation. However, the keyhole formation needs further studies.

6.6 Skin-core tests

Figure 64 shows skin-core 1 micrographs of the skin area, skin-core interface area and the core area.

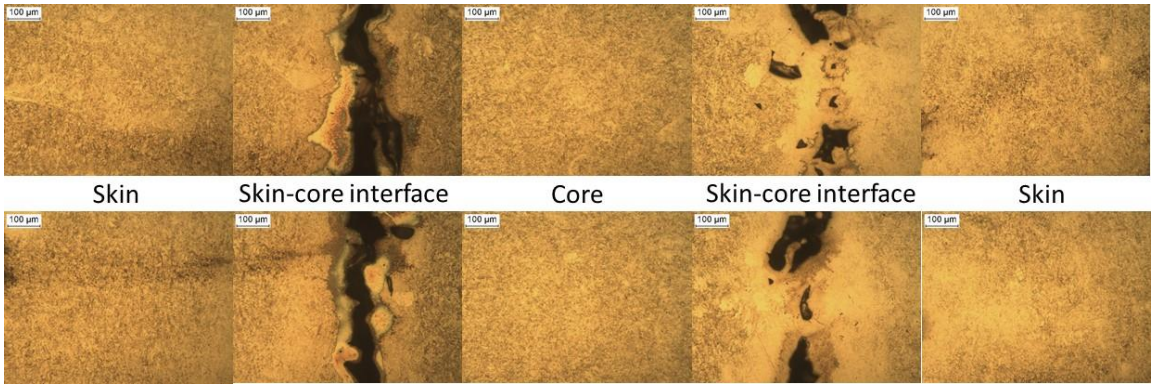

Figure 64. Skin-core 1 micrographs.

As it can be observed from the figure 64, in the skin and core areas do not include pores and the microstructure is solid. It can be noticed also that there is no cracks in skin or core areas. As mentioned before, the skin of the specimens were always made with same, nominal parameters, but the cores had variation in the parameters. Skin-core 1 has nominal parameters in the core are also. The interface area of skin-core 1 was not built solid. It has major pores, and as it can be seen from figure 64, the skin and core were not melted together. This is because of the offset parameter was set too big and there was not enough overlapping between the skin and core. The build of the core with doubled layer thickness was otherwise a success, since the micrographs show that there are no major defects in the microstructure of the skin-core 1.

Figure 65 illustrates the skin-core 2 micrographs.

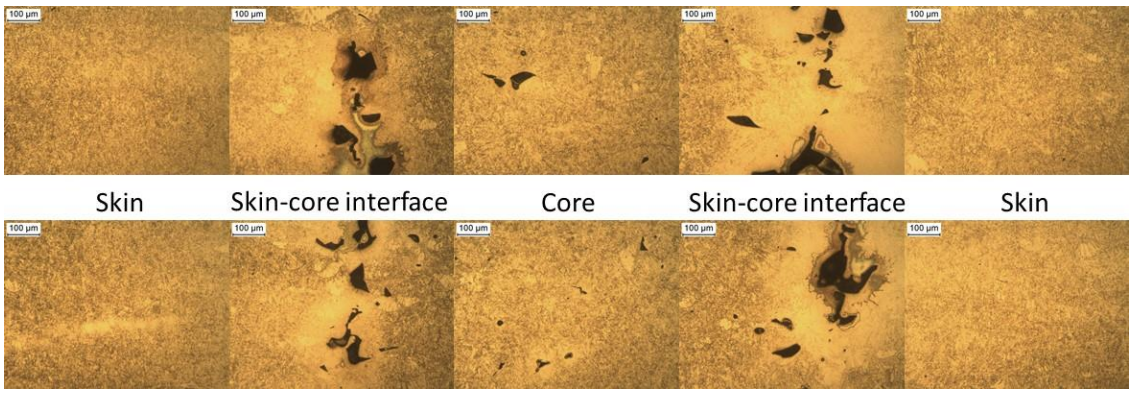

Figure 65. Skin-core 2 micrographs.

Figure 65 shows that the skin area was built without pores or defects. In skin-core 2 the core was made with lower heat input than the skin-core 1. As it can be seen from the figure 65, the core of this piece includes pores, but the porosity of the core area was varying in the piece. Also in skin-core 2, the skin-core interface area was not built as desired. As it can be observed from the figure 65, the interface area includes big pores and gaps between the skin and core area. The porosity in the interface area is because the offset parameter was same than in skin-core 1, and as mentioned before, the overlapping of skin and core areas was too small. Also in skin-core 2, the core building with doubled layer thickness was in good level, since the porosity of the core was small.
Figure 66 shows the skin-core 3 micrographs.

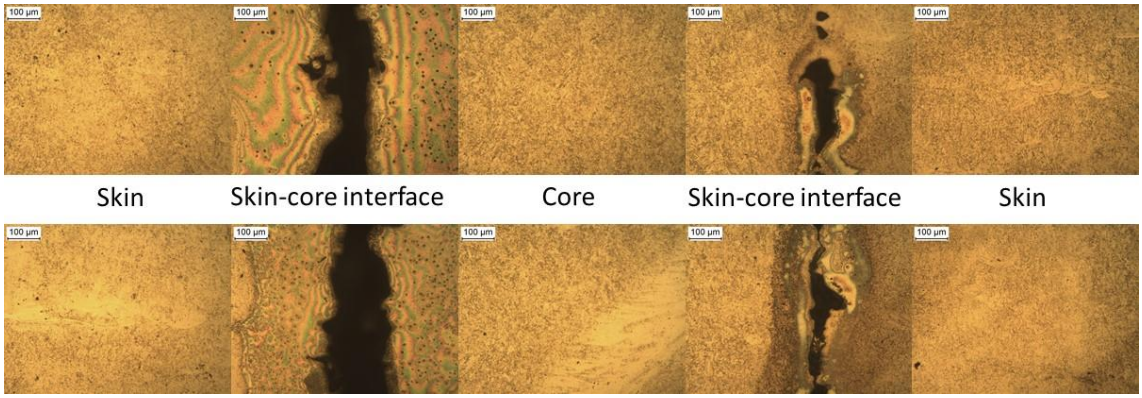

Figure 66. Skin-core 3 micrographs

The skin-core 3, core was made with higher energy density input than the skin-core 1 and skin-core 2. As it can be seen from the figure 66, the skin and core areas of this piece include only very small pores. The core area includes much smaller pores than the skin-core 2. Interesting is that in skin-core 3, also the skin area has some small pores. Similarly as before, the interface area is filled with pores and large gaps between skin and core area. Reason for this is the same as with the skin-core 1 and skin-core 2, the overlapping of the skin and core was too small and therefore joining of these two areas was poor. But also in this piece, the building of the core with doubled layer thickness was success, since the core area is almost pore free.

7 ERROR ESTIMATION

Error estimation in this thesis concentrates on the measurement results of the single track tests. Etching of the single track test samples was challenging, since the etching was uneven. Due to this the visibility of the outlines of the single tracks was rather

unsatisfactory. This might have caused some errors in the measurements. The polished sections of the single track test pieces were slightly convex since the single tracks situated very close to the edge of the bulk material. This convexity caused problems in microscope taken photographs. The micrographs were combined from 3 to 4 different pictures in order to generate sharp images to analyze. The combining of the micrographs could have result in errors in penetration depth and bead width measurements because of the measurements were made by measuring the amount of pixels in certain length. This amount of pixels were then scaled into the scale in the pictures.

8 CONCLUSIONS

Aim of this thesis was to study the aspects for increasing the process efficiency of LAM process. The process efficiency in LAM process usually means the build rate of the parts. The unit of the build rate is mm^3/s. It was decided to study the input-output parameter relations more closely, since the process efficiency adjustment requires basic understanding and knowledge of these parameters. Figure 67 presents the laser beam-material-interaction model which was used as base when studying effect of different parameters in LAM process.

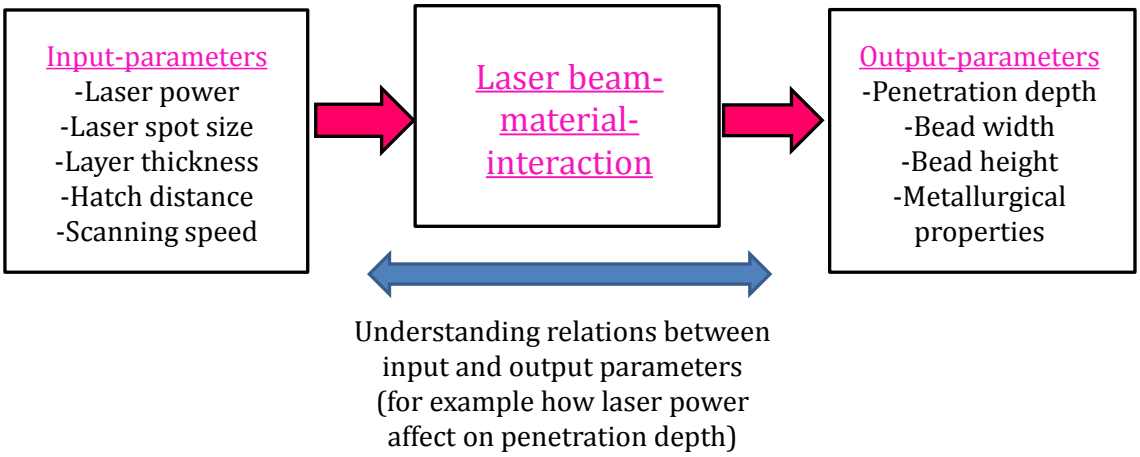

Figure 67. Laser beam-material-interaction parameters.

Literature review of this thesis includes basic principles of LAM process and introduction for the important process parameter effects in the building process. It was concluded in literature review that the most important process input parameters are:

- laser power,
- layer thickness,
- laser scan speed,

- hatch distance and
- laser beam spot size.

It was also concluded in literature review that the understanding the building process requires understanding of the formation of single exposed track. Laser power and scanning speed has effect on track formation and consistency. Also the layer thickness effects on single track formation. It was also concluded that it is possible to increase the build rate of the LAM process by using the skin-core building strategy. Skin-core building strategy enables usage of higher power lasers and thicker powder layers in building of core area and with this increase the build speed. The quality and resolution of the part is not decreasing in skin-core building strategy, since the skin is manufactured with thinner layers and lasers which have smaller beam spot size.

The experimental part focuses on studying and understanding of the LAM process input-output parameter effects and relations. The tests were made with two different LAM systems and the results were compared to each other. Single track tests were made with 200 W laser equipped prototype system representing the EOS M-series in LUT Laser and with 400 W system EOS EOSINT M280 in EOS Finland, Turku.

One of the built bulk pieces was heat treated before the single track exposing. It was concluded in single track tests that the energy density input has effect on penetration depth and bead width of the single tracks. When energy density input is increased, the penetration depth also increases. It was also concluded that when laser interaction time increases, the penetration depth increases. Width-depth ratio, *WDR*, was calculated and it showed that the *WDR* is decreasing when energy density input and laser interaction time is increasing. The area of penetration, *WDA*, was also calculated. It was concluded that the *WDA* is increasing when energy density input and laser interaction time is increasing.

It was concluded that the penetration depth does not have variation when comparing single tracks from the beginning and from the middle of the tracks. It was noticed that there is possibility to form keyhole in each exposed track with the tested parameters. It was concluded that laser interaction time has effect on the keyhole formation, since the penetration depth is increasing while the laser interaction time increases. The differences between penetration depths of tests made with 200 W and 325 W laser powers may also

occur because the laser beam profile can be different. In order to make more specific conclusions the laser beams should be analyzed in order to see if the differences in penetration depths are caused by different beam profiles.

One of the important conclusions was that the form of some of the single tracks indicates that there has been a keyhole during the single track exposure. During the literature review it was noticed that the keyhole formation in LAM process have not been studied extensively. It was shown in study by M.E. Islam et al. (M.E. Islam et al. 2012) that temperatures rose as high as 1750 °C which is much higher than the melting point of stainless steel material. These temperature peaks can indicate the metal vapor that is formed when keyhole is formed. It can be concluded that in LAM process a keyhole can be formed.

The test results showed that there is correlation between input and output parameters. Equations were created from the measurement data and it showed that it is possible to have rough estimations on the single track formation with these equations. It was concluded that the penetration depth and *WDA* can be estimated with the created equations.

One of the main conclusions in this thesis was that the process efficiency can be described with energy density vs. *WDA* equation. *WDA* can be calculated as equation 12 presents.

$$WDA = 2 \cdot 10^{-6} \cdot ED^{1.70} \quad (12)$$

where, *WDA* area of penetrated bead,
ED energy density.

The *WDA* describes the cross-section area of exposed single track and it includes important output parameters such as penetration depth and bead width. The energy density input describes the most important input parameters such as laser power, scan speed, layer thickness and hatch distance. The experiments showed that these input and output parameters correlate, and with these parameters the area of the penetration can be roughly estimated. However, it must be remembered that this equation, as well as the equations presented in results and discussion, gives rough estimation only with the SS 17-4 PH stainless steel material used in this thesis.

The skin-core tests showed that it is possible to manufacture objects with this kind of building strategy. It was concluded that the building speed can be increased with skin-core strategy. However, defining the optimal building parameters can be challenging since there is the interface area between skin and core, which must be fully joined together.

9 FURTHER STUDIES

The experimental part of this thesis showed that it is possible to evaluate the formation of the single scanned tracks in LAM of stainless steel. However, further studies should be done in order to get more accurate methods to estimate what happens in the building process:

- The single track tests showed that parameter testing should be done in order to understand the effects of the input process parameters into the output ones. The formation of the keyhole effect should be studied more closely.
- The test results showed that there is theoretical possibility to achieve keyhole with the tested parameters. The track scanning should be monitored closely in order to receive more information about the keyhole formation.
- The formed single tracks should be studied more with non-destructive methods such as x-ray imaging and laser spectrometer microscope.
- Also further studies should be made with various laser powers in order to see if there is correlation between the same energy density inputs with different laser powers.
- The formation of multiple tracks should be studied in order to achieve more accurate knowledge of the manufacturing process.

LIST OF REFERENCES

ASTM Standard F2792-12a, Standard Terminology for Additive Manufacturing Technologies, 2012

Buchbinder, D., Schleifenbaum, H., Heidrich, S., Bültmann, J. High Power Selective Laser Melting (HP SLM) of Aluminum Parts, 2011, Physics Procedia Volume 12, Part A, 2011, Proceedings of the 6th International WLT Conference on Lasers In Manufacturing, p.271-278, Elsevier Ltd. [Web document] From: http://www.sciencedirect.com/science/article/pii/S1875389211001143 [referred: 4.11.2013]

Ciurana, J., Hernandez, L., Delgado, J. Energy density analysis on single tracks formed by selective laser melting with CoCrMo powder material, 2013, The International Journal of Advanced Manufacturing Technology, Volume 68, Issue 5-8, p. 1103-1110, Springer-Verlag London, Online ISSN: 1433-3015

EOS GmbH – EOS StainlessSteel 17-4 PH Material data sheet, [Web document] From: http://www.3axis.us/matetials/dmls/stainless-steel-17-4-mds.pdf [referred: 31.10.2013]

EOS GmbH – EOSINT M270/PSW 3.2 Operation manual, 2006

Gibson, I., Rosen, D.W., Stucker, B. Additive manufacturing technologies – Rapid prototyping to direct digital manufacturing, 2010, Springer New York. ISBN: 978-1-4419-1119-3

Ilyas, I., Taylor, C., Dalgarno, K., Gosden, J. Design and manufacture of injection mold tool inserts produced using indirect SLS and machining processes, 2010, Rapid Prototyping Journal Volume 16, Number 6. p. 429-440, Emerald Group Publishing Limited. ISSN: 1355-2546

Islam, M.E., Taimisto, L., Piili, H., Nyrhilä, O., Salminen, A., Comparison of theoretical and practical studies of heat input in laser assisted additive manufacturing of stainless

steel. Proc. 37th International Conference Matador. 25th – 27th July, 2012. Manchester, U.K.,The University of Manchester, pp. 365-368.

Kelbassa, I., Gasser, A., Meiners, W., Backes, G., Müller, B., High speed LAM, 2012 Conference proceedings of the 37th International MATADOR Conference, University of Manchester, July 2012, Edited by Srichand Hinduja, Lin Li

Kruth, J- P., Vandenbroucke, B., Van Vaerenbergh, J., Mercelis, P. Benchmarking of different SLS/SLM processes as rapid manufacturing techniques, 2005. [Web document] From: http://www.lasercusing.nl/files/bestanden/Benchmarking_of_different_SLS-SLM_processes.pdf [referred: 31.10.2013]

Kruth, J- P., Badrossamay, M., Yasa, E., Deckers, J., Thijs, L., Van Humbeeck, J., Part and material properties in selective laser melting of metals, 2010, ISEM XVI Keynote paper, [Web document] From: https://lirias.kuleuven.be/bitstream/123456789/265815/1/Kruth_ISEM-XVI_keynote_paper.pdf [referred: 30.10.2013]

Li, R., Liu, J., Shi, Y., Wang, L., Jiang, W., Balling behavior of stainless steel and nickel powder during selective laser melting process, 2012, The International Journal of Advanced Manufacturing Technology, Volume 59, Issue 9-12, p. 1025-1035, Springer-Verlag, Online ISSN: 1433-3015

Löber, L., Flache, C., Petters, R., Kühn, U., Eckert, J., Comparison of different post processing technologies for SLM generated 316L steel parts, 2013, Rapid Prototyping Journal, Volume 19, Number 3. p. 173-179, Emerald Group Publishing Limited, ISSN: 1355-2546

Piili, H. Characterization of Laser Beam and Material Interaction, 2013 Doctoral Thesis, Acta Universiatis Lappeenranta 512, ISBN: 978-952-265-381-9

Schleifenbaum, H., Meiners, W., Wissenbach, K., Hinke, C. High Power Selective Laser Melting: A New Approach for Individualized Series Production, 2009, Conference

Proceedings of the 28th International Congress on Applications of Lasers & Electro-Optics (ICALEO), LIA Publication # 612, Volume 102, ISBN: 978-0-912035-59-8

Schleifenbaum, H., Meiners, W., Wissenbach, K., Hinke, C. Individualized production by means of high power Selective Laser Melting, 2010, CIRP Journal of Manufacturing Science and Technology, Volume 2, Issue 3, Elsevier Ltd. ISSN: 1755-5817

Schleifenbaum, H., Diatlov, A., Hinke, C., Bültmann, J., Voswinckel, H. Direct photonic production: towards high speed additive manufacturing of individualized goods, 2011, Production Engineering, Volume 5, Issue 4, p. 359-371, Springer-Verlag, Online ISSN: 1863-7353

Steen, W.M., Mazumder, J., Laser Material Processing, 2010, 4th Edition, Spinger-Verlag London Limited, ISBN: 978-1-84996-061-8

Wohlers, T., Caffrey, T., Wohlers Report 2012 – Additive Manufacturing and 3D Printing State of the Industry Annual Worldwide Progress Report, 2012, Wohlers Associates, Inc. ISBN 0-9754429-8-8

Yadroitsev, I., Smurov, I., Selective laser melting technology: from the single laser melted track stability to 3D parts of complex shape, 2010a, Physics Procedia 5, p. 551-560, Conference proceedings of 6th International Conference of Laser Assisted Net Shape Engineering, Elsevier, ISSN: 1875-3892

Yadroitsev, I., Gusarov, A., Yadroitsava, I., Smurov, I., Single track formation in selective laser melting of metal powders, 2010b, Journal of Materials Processing Technology, Volume 210, Issue 12, p. 1624-1631, Elsevier, ISSN: 0924-0136

Yadroitsev, I., Krakhmalev, P., Yadroitsava, I., Johansson, S., Smurov, I., Energy input effect on morphology and microstructure of selective laser melting single track from metallic powder, 2013, Journal of Materials Processing Technology, Volume 213, Issue 4, p. 606-613, Elsevier, ISSN: 0924-0136

APPENDICES

APPENDIX I MICROGRAPHS OF THE SINGLE TRACKS

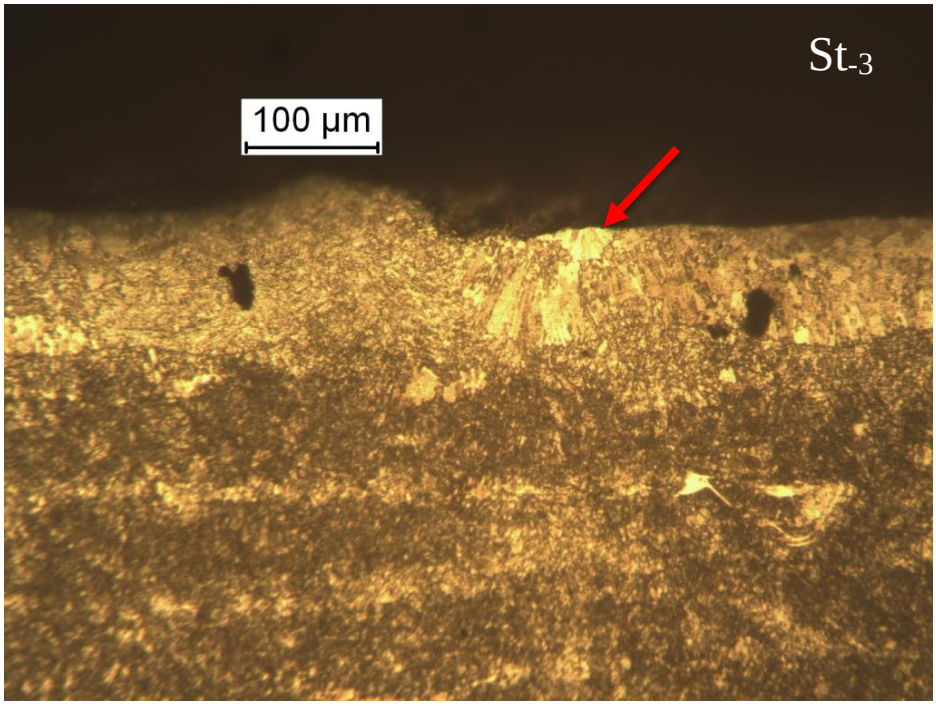

Figure 1. Micrograph of *St-3* when laser power of 200 W was used. Arrow indicates the *St-3*.

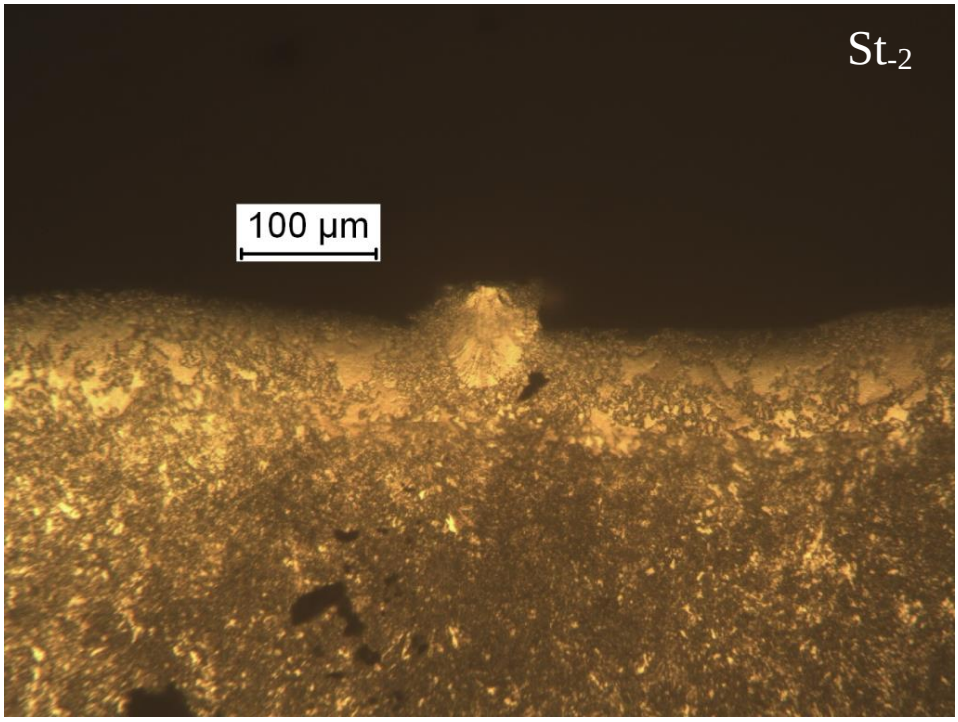

Figure 2. Micrograph of *St-2* when laser power of 200 W was used.

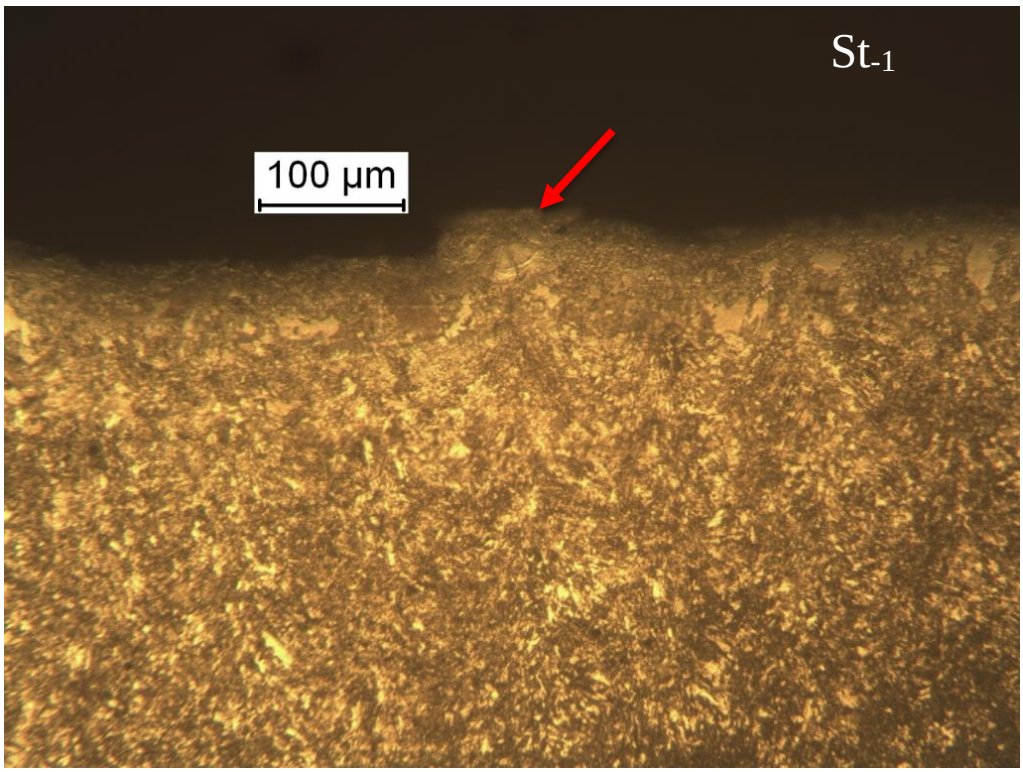

Figure 3. Micrograph of *St-1* when laser power of 200 W was used. Arrow indicates the *St-1*

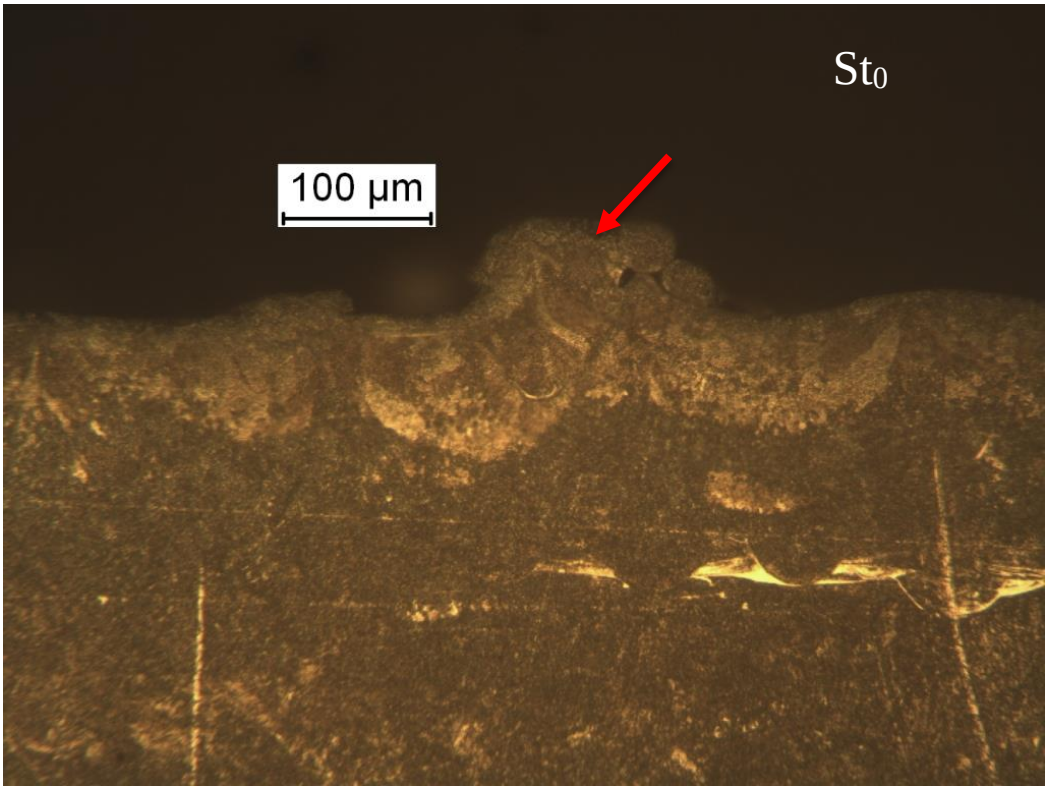

Figure 4. Micrograph of *St0* when laser power of 200 W was used. Arrow indicates the *St0*.

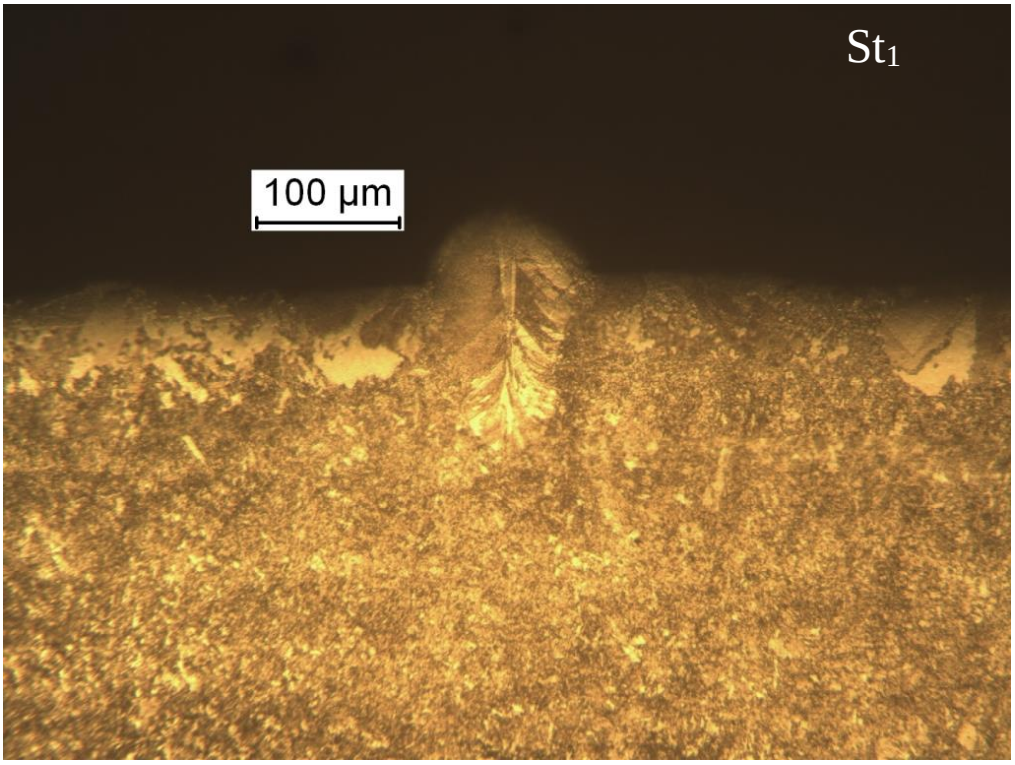

Figure 5. Micrograph of *St1* when laser power of 200 W was used.

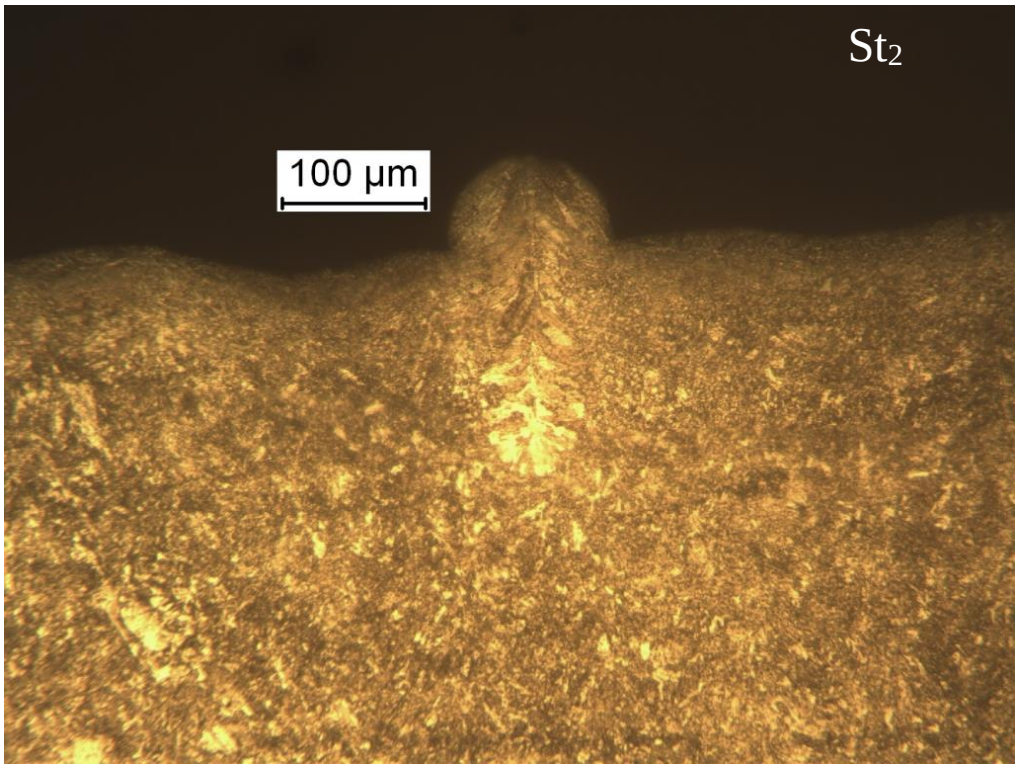

Figure 6. Micrograph of *St2* when laser power of 200 W was used.

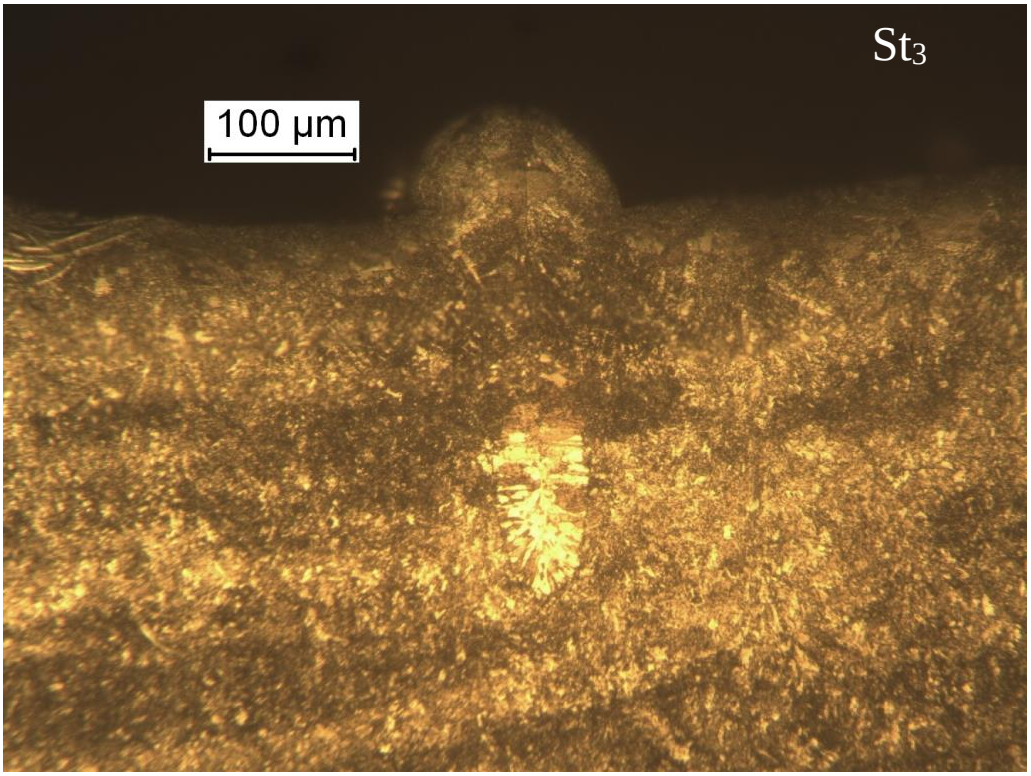

Figure 7. Micrograph of *St3* when laser power of 200 W was used.

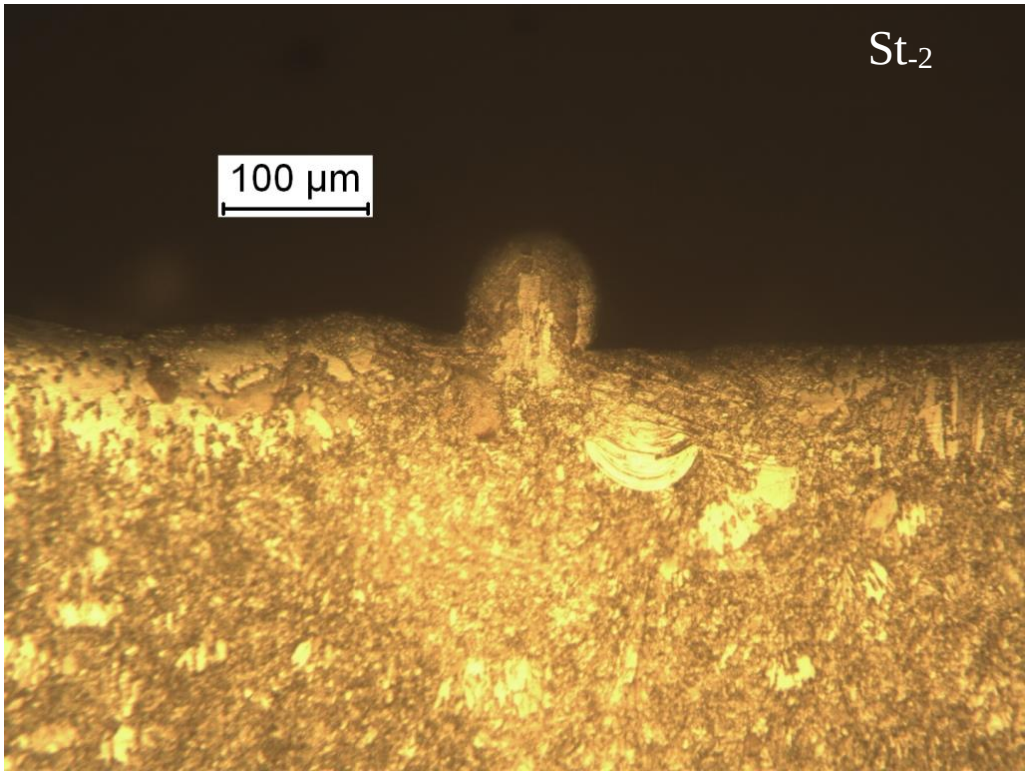

Figure 8. Micrograph of *St-2* when laser power of 325 W was used.

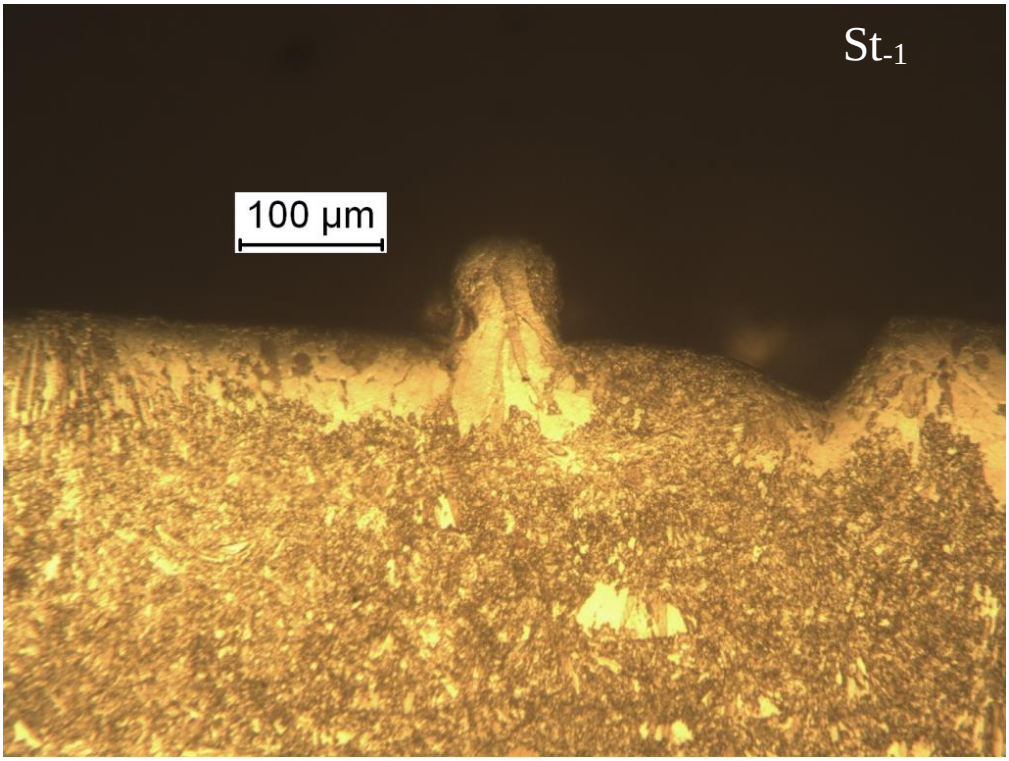

Figure 9. Micrograph of *St-1* when laser power of 325 W was used.

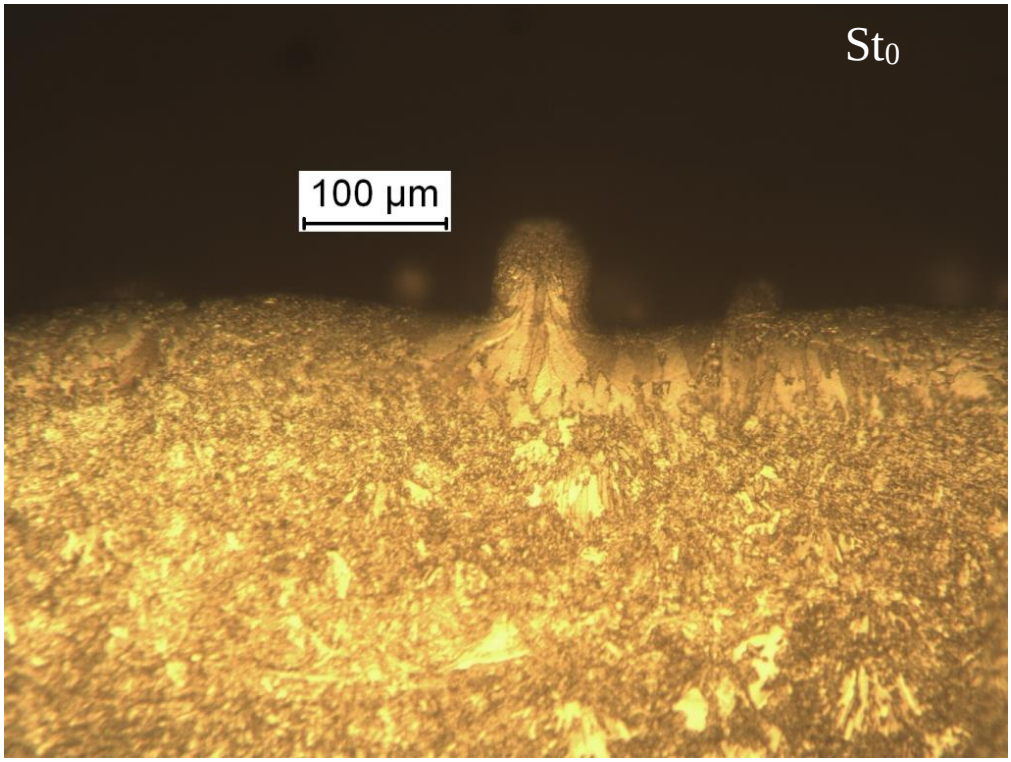

Figure 10. Micrograph of *St0* when laser power of 325 W was used.

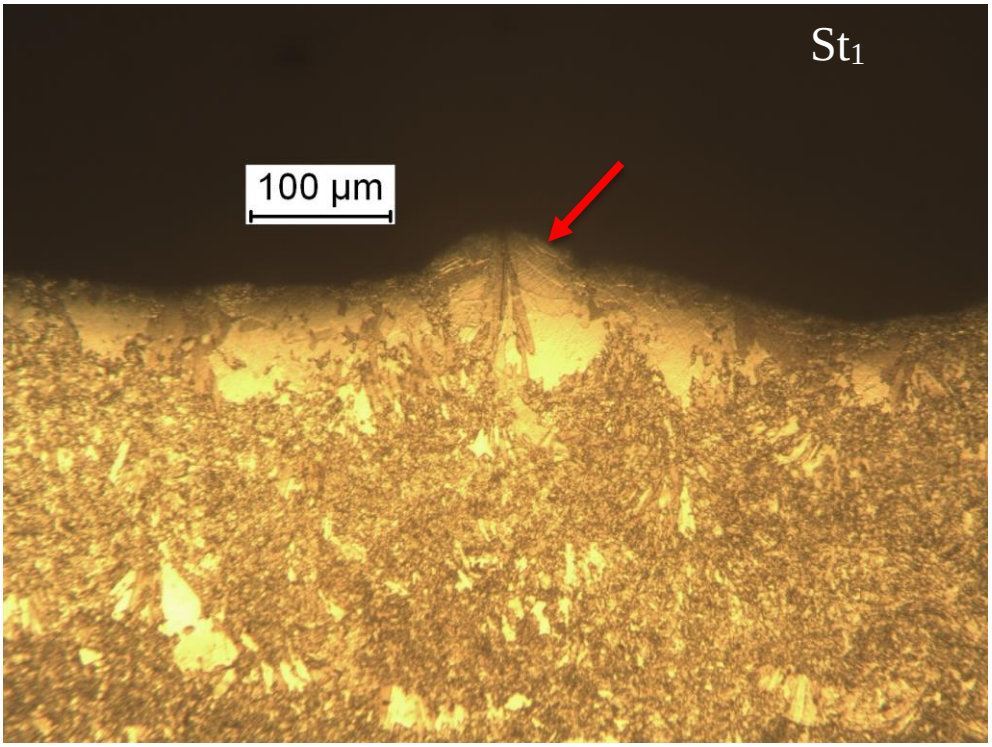

Figure 11. Micrograph of *St₁* when laser power of 325 W was used. Arrow indicates the *St₁*.

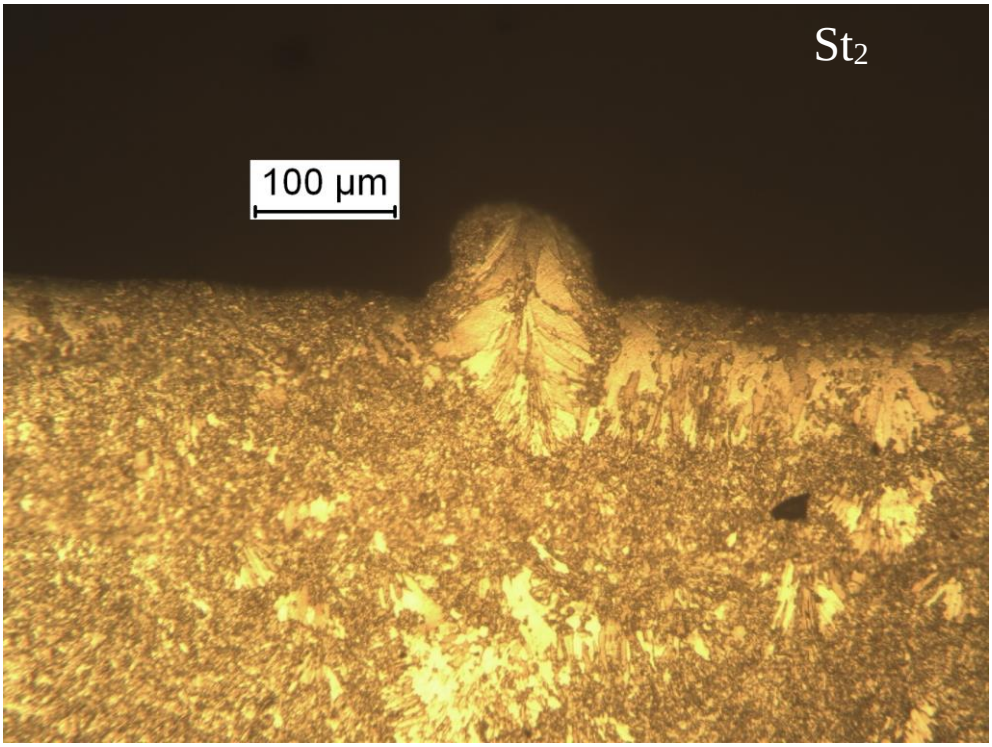

Figure 12. Micrograph of *St₂* when laser power of 325 W was used.

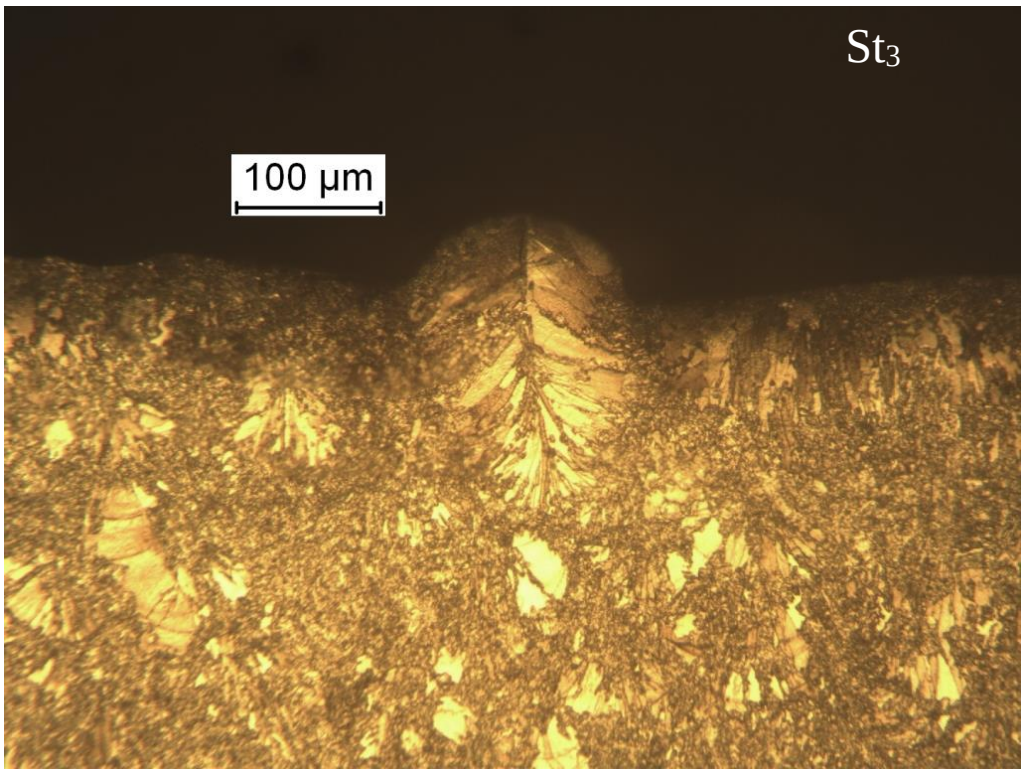

Figure 13. Micrograph of *St3* when laser power of 325 W was used.

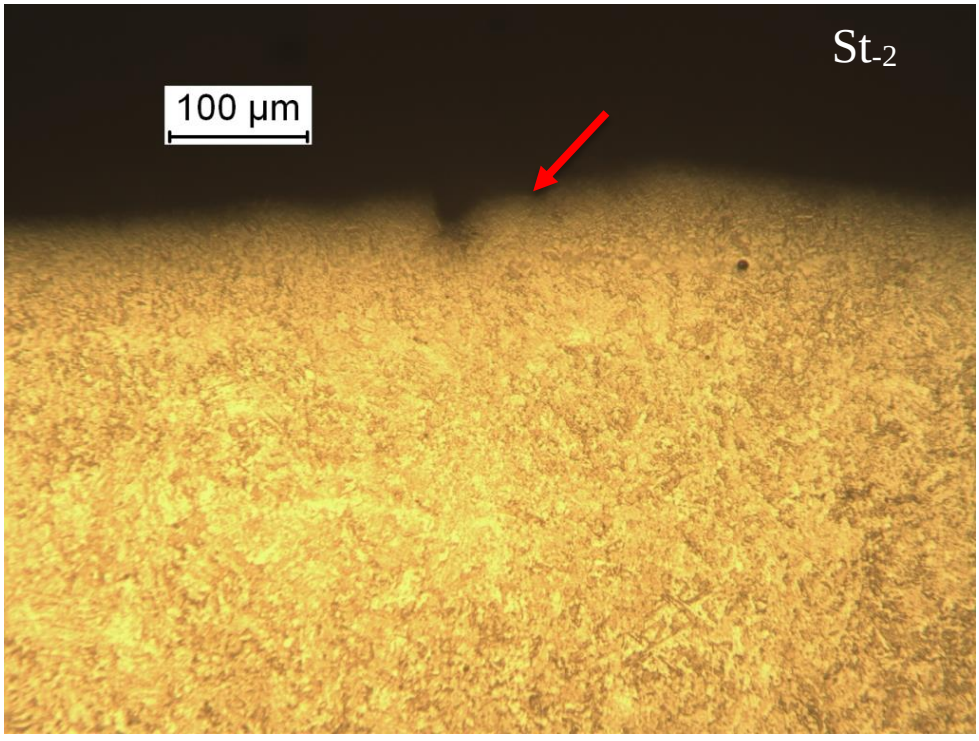

Figure 14. Micrograph of *St-2* when laser power of 325 W and heat treatment was used. Arrow indicates the *St-2*.

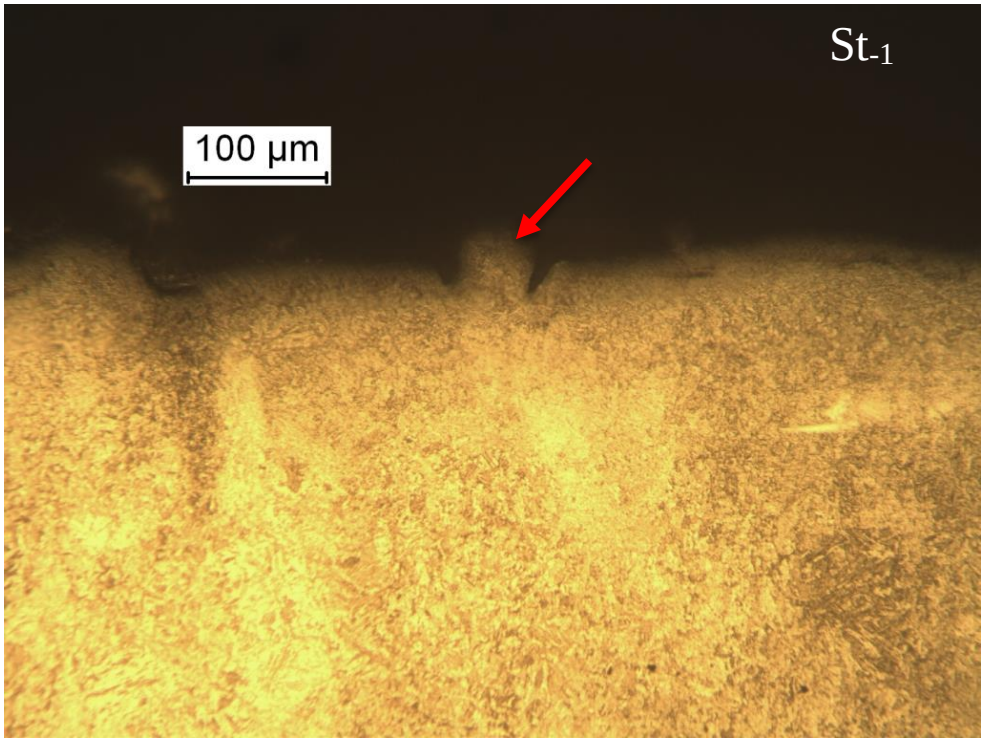

Figure 15. Micrograph of *St-1* when laser power of 325 W and heat treatment was used. Arrow indicates the *St-1*.

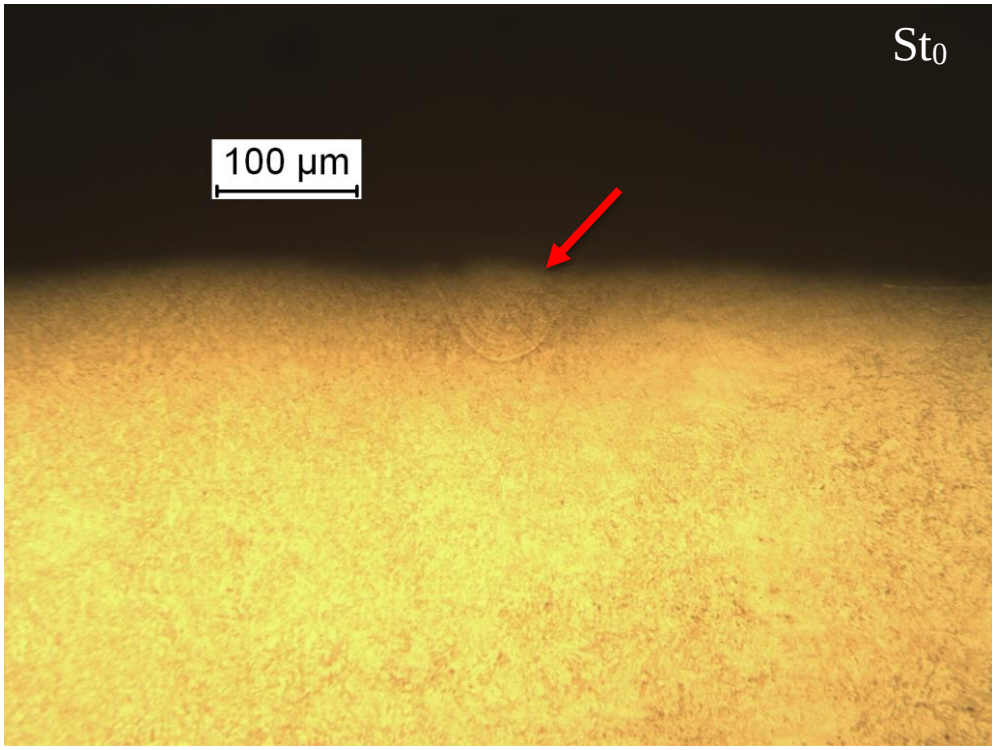

Figure 16. Micrograph of *St0* when laser power of 325 W and heat treatment was used. Arrow indicates the *St0*.

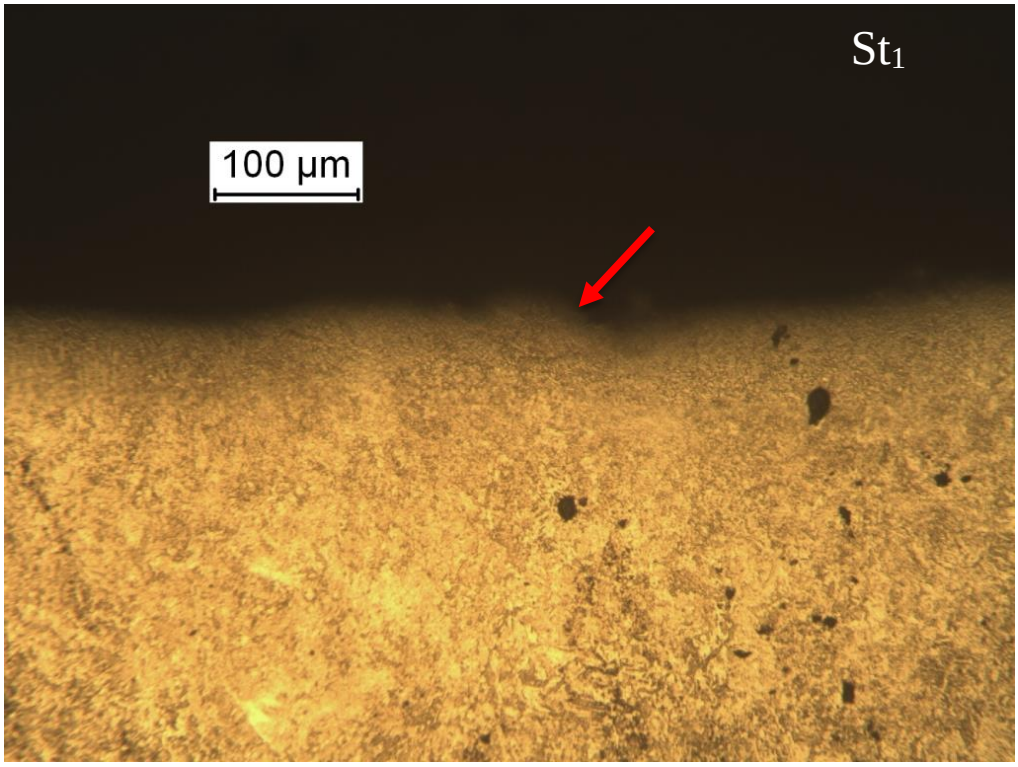

Figure 17. Micrograph of *St₁* when laser power of 325 W and heat treatment was used. Arrow indicates the *St₁*.

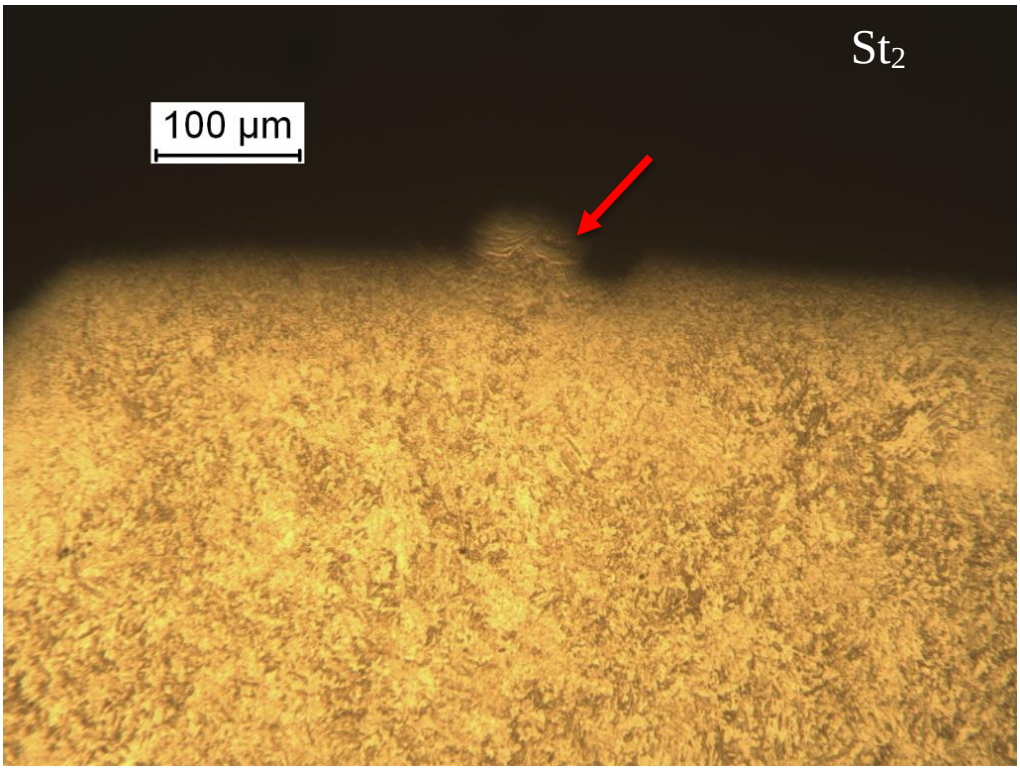

Figure 18. Micrograph of *St₂* when laser power of 325 W and heat treatment was used. Arrow indicates the *St₂*.

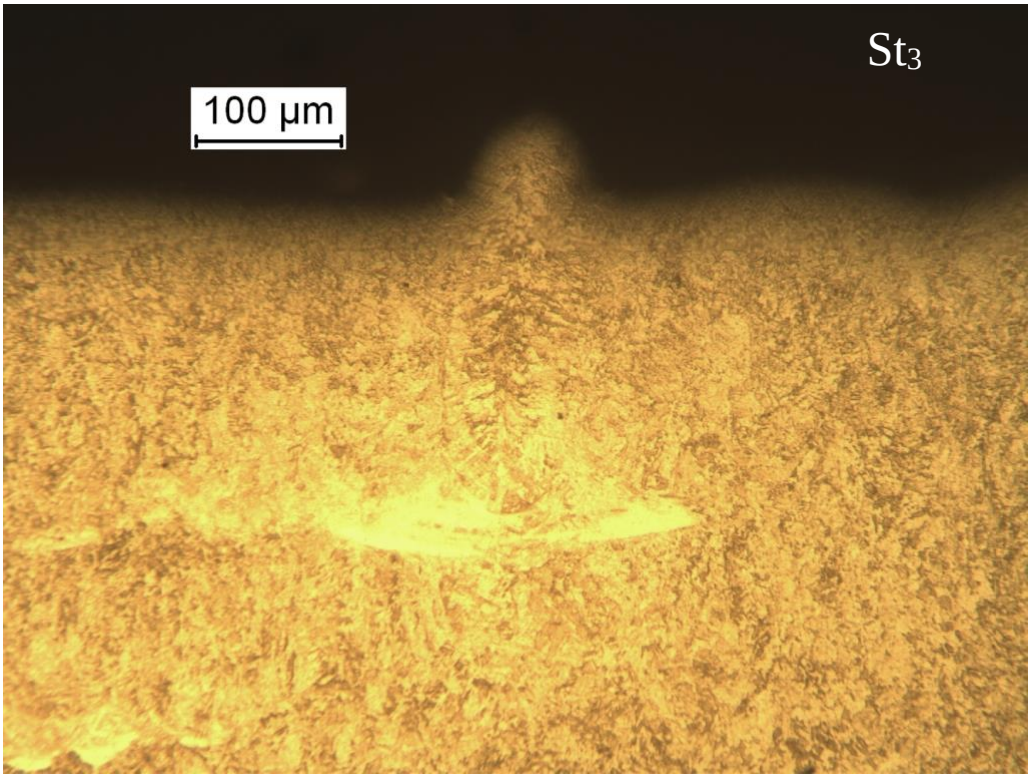

Figure 19. Micrograph of *St3* when laser power of 325 W and heat treatment was used.

APPENDIX II SINGLE TRACK MEASUREMENT RESULTS

Table 1. Measurement results of single tracks when laser power of 200 W was used.

Laser power 200 W	**St_{-3}**	**St_{-2}**	**St_{-1}**	**St_0**	**St_1**	**St_2**	**St_3**
Penetration [µm]	52	49	35	75	108	123	248
Width [µm]	74	67	58	81	101	88	121
Height of the bead [µm]	29	42	25	79	63	75	94
Energy density [J/mm^3]	63	71	83	100	125	167	250
Intensity [W/cm^2]	$2.6*10^6$	$2.6*10^6$	$2.6*10^6$	$2.6*10^6$	$2.6*10^6$	$2.6*10^6$	$2.6*10^6$
Laser interaction time [ms]	0.06	0.07	0.08	0.10	0.13	0.17	0.25
***WDR* [-]**	1.44	1.36	1.67	1.09	0.93	0.71	0.49
***WDA* [mm^2]**	0.004	0.003	0.002	0.006	0.011	0.011	0.030

Table 2. Measurement results of single tracks when laser power of 325 W was used.

Laser power 325 W	**St_{-3}**	**St_{-2}**	**St_{-1}**	**St_0**	**St_1**	**St_2**	**St_3**
Penetration [µm]	N/A	31	47	58	82	111	149
Width [µm]	N/A	84	78	72	106	124	147
Height of the bead [µm]	N/A	73	70	70	26	66	54
Energy density [J/mm^3]	63	71	83	100	125	167	250
Intensity [W/cm^2]	$4.2*10^6$	$4.2*10^6$	$4.2*10^6$	$4.2*10^6$	$4.2*10^6$	$4.2*10^6$	$4.2*10^6$
Laser interaction time [ms]	0.04	0.04	0.05	0.06	0.08	0.10	0.15
***WDR* [-]**	0.00	2.69	1.68	1.24	1.29	1.12	0.98
***WDA* [mm^2]**	0.000	0.003	0.004	0.004	0.009	0.014	0.022

Table 3. Measurement results of single tracks when laser power of 325 W and heat treatment was used.

Laser power 325 W Heat treated	**St_{-3}**	**St_{-2}**	**St_{-1}**	**St_0**	**St_1**	**St_2**	**St_3**
Penetration [µm]	N/A	36	35	65	34	52	211
Width [µm]	N/A	64	53	98	66	81	91
Height of the bead [µm]	N/A	0	23	0	10	30	57
Energy density [J/mm^3]	63	71	83	100	125	167	250
Intensity [W/cm^2]	$4.2*10^6$	$4.2*10^6$	$4.2*10^6$	$4.2*10^6$	$4.2*10^6$	$4.2*10^6$	$4.2*10^6$
Laser interaction time [ms]	0.04	0.04	0.05	0.06	0.08	0.10	0.15
***WDR* [-]**	0.00	1.77	1.50	1.50	1.96	1.56	0.43
***WDA* [mm^2]**	0.000	0.002	0.002	0.006	0.002	0.004	0.019

APPENDIX III BEAD HEIGHT MEASUREMENTS

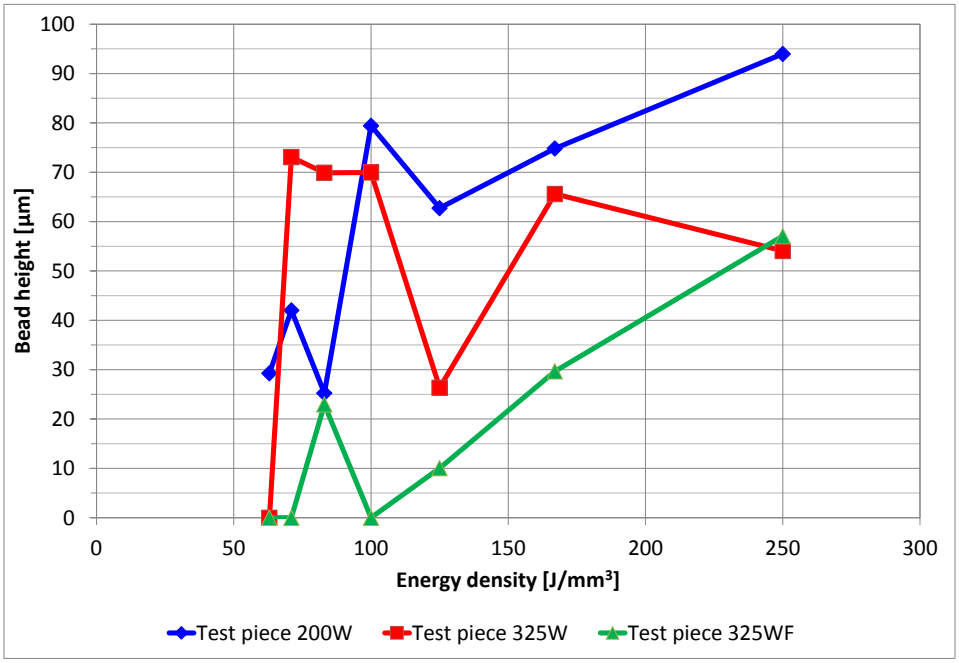

Figure 1. Energy density vs. bead height when laser power of 200 W, 325 W and heat treatment was used.

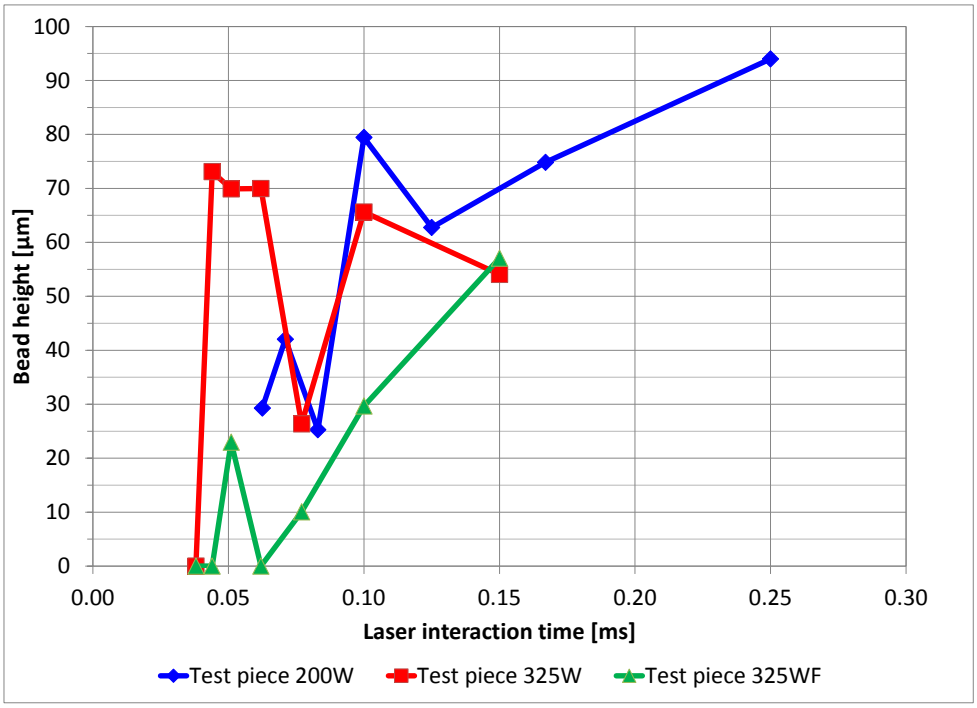

Figure 2. Laser interaction time vs. bead height when laser power of 200 W, 325W and heat treatment was used.

APPENDIX IV HEAT TREATMENT TEMPERATURE GRAPH

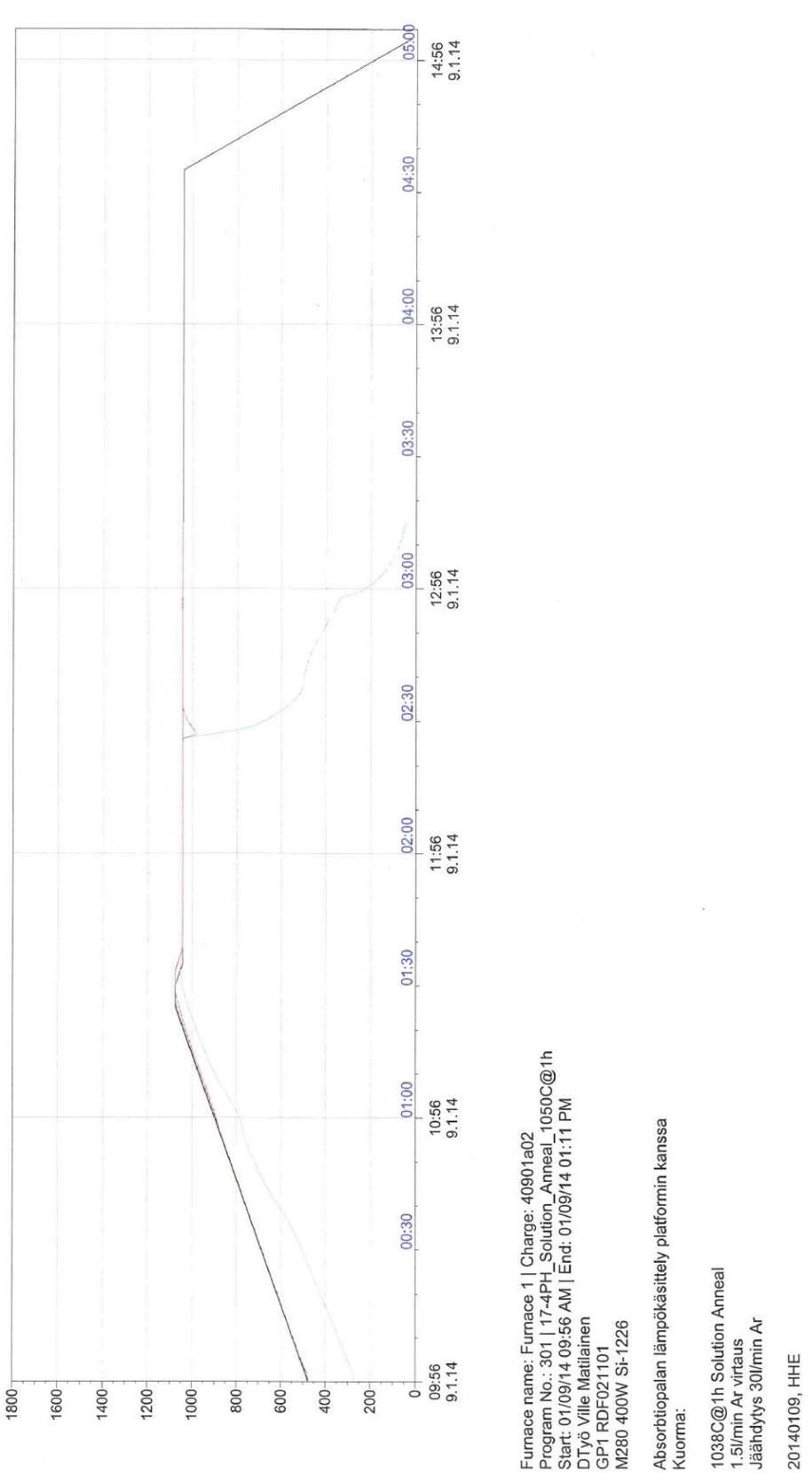

Figure 1. Heat treatment temperature graph.